

The Pennsylvania State University
Department of Engineering Science and Mechanics
College of Engineering

**FINITE-ELEMENT IMPLEMENTATION AND VERIFICATION OF
COMPLEX FLUID MODELS BASED ON EVOLVING NATURAL
CONFIGURATIONS, MOTIVATED BY STUDIES OF BLOOD**

A Thesis in
Engineering Science and Mechanics
by
Amel O. Awadelkarim

© 2017 Amel O. Awadelkarim

Submitted in Partial Fulfillment
of the Requirements
for the Degree of

Master of Science

December 2017

The thesis of Amel O. Awadelkarim was reviewed and approved* by the following:

Francesco Costanzo
Professor of Engineering Science and Mechanics
Thesis Advisor

Keefe Manning
Professor of Biomedical Engineering

Judith A. Todd
P. B. Breneman Department Head Chair,
Department of Engineering Science and Mechanics

*Signatures are on file in the Graduate School.

Abstract

The ability to model the flow of blood along with its concurrent capacity for clotting and lysis can greatly accelerate the development and deployment of many clinical applications. Examples of these range from novel surgical therapies for acute ischemic stroke to intra-operative pharmacological interventions for the prevention of massive coagulation or hemorrhage in liver transplantation. In this study, a specific fully-coupled model is selected from the literature for the flow, clotting, and lysis of blood. A new approach is then proposed for the finite element method (FEM) implementation of this model. Specifically, a reduced model is first considered, limited to the mere mechanical response of an incompressible (viscoelastic) Oldroyd-B fluid. For this model, Eulerian, Lagrangian, and arbitrary Lagrangian-Eulerian (ALE) finite element (FE) implementations are considered. Subsequently, the model is expanded to include reaction and diffusion concurrent with advection, which is necessary to model the chemistry of blood clotting and lysis that can take place during blood flow. The proposed FEM scheme is then extended to be applicable to the fully-coupled model. COMSOL Multiphysics[®] has been used as the programming environment for the FEM implementation. The accuracy of the proposed implementations has been assessed using the method of manufactured solutions (MMS). A convergence analysis is performed to observe the dependence of the error in the numerical solutions upon refinement of the mesh. Finally, we propose sources of error in the solver and discuss future work for the use of the proposed formulation in physiologically relevant applications.

Table of Contents

List of Figures	vii
List of Tables	x
List of Symbols	xi
Chapter 1	
Motivation for Blood Chemo-Mechanics	1
1.1 Premise	1
1.2 Strokes	1
1.3 Current Therapies	2
1.3.1 Non-Invasive Methods	2
1.3.2 Invasive Methods	3
1.3.3 Efficiency	4
1.4 A New Concept in Clot-Removal Devices	4
1.5 Mathematical and Numerical Modeling	5
1.6 Literature Review	7
1.7 Notation	13
Chapter 2	
Fluid Models & Oldroyd-B Example	15
2.1 Existing Fluid Models for Blood	15
2.1.1 Power Law Model	15
2.1.2 Maxwell-Type Model	17
2.1.3 Oldroyd-B Model	20
2.2 Oldroyd-B Problem Setup	21
2.3 Motion Representation Frameworks	25
2.3.1 Lagrangian Formulation	27
2.3.2 ALE Formulation	29

Chapter 3	
COMSOL Multiphysics® Inputs	32
3.1 Introduction to the Finite Element Method	32
3.2 Method of Manufactured Solutions	34
3.2.1 Manufactured Solutions	36
3.2.1.1 Pressure	37
3.2.1.2 Velocities and Displacements	38
3.2.1.3 Tensor G	39
3.2.2 COMSOL Multiphysics® Inputs	40
3.2.2.1 Manufactured Source Terms	41
3.2.2.2 Initial and Boundary Conditions	42
3.2.3 Solver Setup	42
3.2.3.1 Domain	42
3.2.3.2 Time-Stepping	43
Chapter 4	
Oldroyd-B Results & Analysis	45
4.1 Eulerian Results	45
4.2 Lagrangian Results	47
4.3 ALE Results	50
4.4 Analysis	53
Chapter 5	
Blood Model & Study	55
5.1 Rheological Clot Model	55
5.2 Study Components	60
Chapter 6	
Blood Model Results & Analysis	63
6.1 Eulerian Results	63
6.2 Lagrangian Results	66
6.3 ALE Results	68
6.4 Analysis	71
Chapter 7	
Conclusion	73
7.1 Future Plans	73
7.1.1 3D Verification Analysis	73
7.1.2 Chemical Contributions to Fluid Model	74
7.1.3 Surrounding Artery	75

7.1.4	Clinical Application	76
7.2	Conclusion	77
Appendix		
	Proof of Equivalence Between Two Models	78
1	Rajagopal et al.	78
2	Hron et al.	79
	Bibliography	81

List of Figures

1.1	(A) Catheter pierces through the thrombus. (B) The Merci [®] Retriever spirals through. (C) Both the retriever and clot are removed from the body. Image from the American Journal of Neuroradiology [1].	4
1.2	Schematic of catheter delivering alternating suction pressure to the face of a blood clot lodged in cerebral artery.	5
1.3	Illustration of the various components of blood. From Saint Luke's Health System webpage.	8
1.4	Common pictorial representations of viscous, elastic, and viscoelastic fluid/solid rheological models. Viscosity and spring constant given by c and k , respectively.	9
2.1	Schematic of the evolving natural configuration. The tensor \mathbf{F}_{κ_R} is the deformation gradient of the line elements surrounding a material point \mathbf{X} in the reference to those in the current configuration. Similarly, $\mathbf{F}_{\kappa_p(t)}$ is the deformation of the line elements in the natural configuration to the current one. The solid line from κ_R to κ_t , $S_{\kappa_R}(\mathbf{X}, t)$ is merely the motion of a material point, \mathbf{X} , through time.	18
3.1	Plot of \mathbf{MSp} at time $t = 0.7$ s.	37
3.2	Plot of the \hat{i} -component of \mathbf{MSv} , \mathbf{MSu} and $\mathbf{MS}\hat{u}$ at time $t = 0.7$ s.	38
3.3	Plot of the \hat{i} -component of the \mathbf{MSv}_A at time $t = 0.7$ s.	39
3.4	$\hat{i} \otimes \hat{i}$ component of \mathbf{MSG} at time $t = 0.7$ s.	40
4.1	Numerical solution of p in Eulerian framework. Left to right: $h = 0.25$ m, $h = 0.0625$ m, and $h = 1.563 \times 10^{-2}$ m.	45
4.2	Numerical solution of \mathbf{v}_1 in Eulerian framework. Left to right: $h = 0.25$ m, $h = 0.0625$ m, and $h = 1.563 \times 10^{-2}$ m.	46
4.3	Numerical solution of \mathbf{G}_{11} in Eulerian framework. Left to right: $h = 0.25$ m, $h = 0.0625$ m, and $h = 1.563 \times 10^{-2}$ m.	46
4.4	Plot of the L^2 and H^1 norms of error for p , \mathbf{v} , and \mathbf{G} — Eulerian.	47

4.5	Numerical solution of p in the Lagrangian framework. Left to right: $h = 0.25$ m, $h = 0.0625$ m, and $h = 1.563 \times 10^{-2}$ m.	48
4.6	Numerical solution of \mathbf{u}_1 in the Lagrangian framework. Left to right: $h = 0.25$ m, $h = 0.0625$ m, and $h = 1.563 \times 10^{-2}$ m.	48
4.7	Numerical solution of \mathbf{G}_{11} in Lagrangian framework. Left to right: $h = 0.25$ m, $h = 0.0625$ m, and $h = 1.563 \times 10^{-2}$ m.	48
4.8	Plot of the L^2 and H^1 norms of error for p , \mathbf{u} , and \mathbf{G} — Lagrangian.	49
4.9	Numerical solution of p in ALE framework. Left to right: $h = 0.25$ m, $h = 0.0625$ m, and $h = 1.563 \times 10^{-2}$ m.	50
4.10	Numerical solution of \mathbf{v} in ALE framework. Left to right: $h = 0.25$ m, $h = 0.0625$ m, and $h = 1.563 \times 10^{-2}$ m.	50
4.11	Numerical solution of \mathbf{G} in ALE framework. Left to right: $h =$ 0.25 m, $h = 0.0625$ m, and $h = 1.563 \times 10^{-2}$ m.	51
4.12	Numerical solution of $\hat{\mathbf{u}}$ in ALE framework. Left to right: $h = 0.25$ m, $h = 0.0625$ m, and $h = 1.563 \times 10^{-2}$ m.	51
4.13	Plot of the L^2 and H^1 norms of error for p , \mathbf{v} , $\hat{\mathbf{u}}$, and \mathbf{G} — ALE. . .	52
5.1	Plot of \mathbf{MSp} at time $t = 0.7$ s.	61
5.2	Plot of the \hat{i} -component of \mathbf{MSv} , \mathbf{MSu} , and $\mathbf{MS}\hat{\mathbf{u}}$ at time $t = 0.7$ s.	61
5.3	Plot of the \hat{i} -component of the \mathbf{MSv}_A at time $t = 0.7$ s.	61
5.4	$\hat{i} \otimes \hat{i}$ component of \mathbf{MSG} at time $t = 0.7$ s.	62
6.1	Numerical solution of p in Eulerian framework. Left to right: $h =$ 0.125 m, $h = 0.0313$ m, and $h = 7.813 \times 10^{-3}$ m.	64
6.2	Numerical solution of \mathbf{v}_1 in Eulerian framework. Left to right: $h = 0.125$ m, $h = 0.0313$ m, and $h = 7.813 \times 10^{-3}$ m.	64
6.3	Numerical solution of \mathbf{G}_{11} in Eulerian framework. Left to right: $h = 0.125$ m, $h = 0.0313$ m, and $h = 7.813 \times 10^{-3}$ m.	64
6.4	Plot of the L^2 and H^1 norms of error for p , \mathbf{v} , and \mathbf{G} — Eulerian. .	65
6.5	Numerical solution of p in Lagrangian framework. Left to right: $h = 0.125$ m, $h = 0.0313$ m, and $h = 7.813 \times 10^{-3}$ m.	66
6.6	Numerical solution of \mathbf{u}_1 in Lagrangian framework. Left to right: $h = 0.125$ m, $h = 0.0313$ m, and $h = 7.813 \times 10^{-3}$ m.	66
6.7	Numerical solution of \mathbf{G}_{11} in Lagrangian framework. Left to right: $h = 0.125$ m, $h = 0.0313$ m, and $h = 7.813 \times 10^{-3}$ m.	67
6.8	Plot of the L^2 and H^1 norms of error for p , \mathbf{u} , and \mathbf{G} — Lagrangian.	68
6.9	Numerical solution of p in ALE framework. Left to right: $h =$ 0.125 m, $h = 0.0313$ m, and $h = 7.813 \times 10^{-3}$ m.	69
6.10	Numerical solution of \mathbf{v}_1 in ALE framework. Left to right: $h =$ 0.125 m, $h = 0.0313$ m, and $h = 7.813 \times 10^{-3}$ m.	69

6.11	Numerical solution of \mathbf{G}_{11} in ALE framework. Left to right: $h =$ 0.125 m, $h = 0.0313$ m, and $h = 7.813 \times 10^{-3}$ m.	69
6.12	Numerical solution of $\hat{\mathbf{u}}_1$ in ALE framework. Left to right: $h =$ 0.125 m, $h = 0.0313$ m, and $h = 7.813 \times 10^{-3}$ m.	70
6.13	Plot of the L^2 and H^1 norms of error for p , \mathbf{v} , $\hat{\mathbf{u}}$, and \mathbf{G} — ALE. . .	71

List of Tables

4.1	Error in numerical solution of p , \mathbf{v} , and \mathbf{G} in Eulerian framework. . .	46
4.2	Error in numerical solution of p , \mathbf{u} , and \mathbf{G} in Lagrangian framework.	49
4.3	Error in numerical solution of p , \mathbf{v} , and \mathbf{G} in ALE framework. . . .	51
4.4	Error in numerical solution of $\hat{\mathbf{u}}$ in ALE framework.	52
5.1	Parameter values for use in clot formulation.	58
6.1	Error in numerical solution of p , \mathbf{v} , and \mathbf{G} in Eulerian framework. .	65
6.2	Error in numerical solution of p , \mathbf{u} , and \mathbf{G} in Lagrangian framework.	67
6.3	Error in numerical solution of p , \mathbf{v} , and \mathbf{G} in ALE framework. . . .	70
6.4	Error in numerical solution of $\hat{\mathbf{u}}$ in ALE framework.	70

List of Symbols

Formulation Variables

- p Scalar multiplier, “pressure”
- \mathbf{v} Velocity field in Eulerian and ALE formulations
- \mathbf{u} Displacement field in Lagrangian formulation
- $\hat{\mathbf{u}}$ ALE map, “mesh-motion”
- \mathbf{B} Left Cauchy-Green stress tensor of the deformation from the natural configuration to the current configuration of the body
- \mathbf{G} Tensor variable, used in redefinition of \mathbf{B}
- J_G Determinant of \mathbf{G}
- \mathbf{T} Cauchy (true) stress of the body
- \mathbf{D} Symmetric part of the velocity gradient
- \mathbf{I} Identity tensor
- \mathbf{F} Deformation gradient from the reference to the current configuration
- J Determinant of \mathbf{F}
- $\hat{\mathbf{F}}$ Deformation gradient from the computational (ALE) domain to the current one
- \hat{J} Determinant of $\hat{\mathbf{F}}$
- \tilde{p} Test function for p

- $\tilde{\mathbf{v}}$ Test function for \mathbf{v} in Eulerian and ALE formulations
- $\tilde{\mathbf{u}}$ Test function for \mathbf{u} in Lagrangian formulation, and for $\hat{\mathbf{u}}$ in ALE formulation
- $\tilde{\mathbf{G}}$ Test function for \mathbf{G}

Verification Variables

- MS p** Manufactured solution for the scalar multiplier, p
- MS \mathbf{v}** Manufactured solution for velocity
- MS \mathbf{v}_A** Manufactured solution for velocity in ALE formulation
- MS \mathbf{u}** Manufactured solution for the displacement
- MS $\hat{\mathbf{u}}$** Manufactured solution for the mesh-motion
- MSG** Manufactured solution for \mathbf{G}
 - c Source term for incompressibility equation in each formulation
 - \mathbf{f} Source term for balance of linear momentum in each formulation
 - \mathbf{A} Source term for evolution equation of the natural configuration in each formulation
- w_A Source term for ALE map equation

Formulation Parameters

- ρ Mass density of the material
- μ Elastic shear modulus of the material
- η Dynamic viscosity of the material
- τ Relaxation time of the material
- n Shear-thinning index in the blood model
- α Constant parameter describing the evolution of \mathbf{B}
- γ Small parameter used in enforcing boundary data in ALE formulation
- h Characteristic mesh length

Chapter 1 | Motivation for Blood Chemo- Mechanics

1.1 Premise

A myriad of clinical applications justify the development of mathematical models to predict the flow and chemistry of blood. Reviewing of all of these would be a daunting task outside the scope of this thesis. Instead, to motivate this study, a specific clinical problem is selected, one with challenges that might be best tackled via a systematic computational approach, as opposed to, say, “trial and error,” or small incremental and empirical improvement of current techniques. The example selected concerns the development of a novel surgical therapy for a class of acute ischemic strokes.

1.2 Strokes

An individual experiences a stroke when there is a disruption to blood flow in the brain so that oxygen can no longer be transported to brain cells. This event occurs when a blood clot fully or partially obstructs an artery carrying oxygenated-blood, or after the rupture of a blood vessel. Ischemic strokes, or strokes caused by a blockage of an artery, are the primary focus of this study, as they make up about 87% of all cases [2].

The embolic and thrombotic strokes are the two most common types of ischemic stroke. When a clot or plaque formed in one place in the body travels to the brain

and gets lodged in a constricting vessel, this is known as an embolic stroke. A thrombotic stroke is instead caused by the build up of a plaque directly on the wall of an artery leading to the brain, say as a result of atherosclerosis. This protrusion from the vessel wall often acts as a site for clotting, which further contributes to the blood flow reduction [3].

Following a stroke, the brain cells deprived of oxygen begin to die and a patient has a small window of time in which permanent damage may be avoided. The effects of a stroke are highly dependent upon the area in which the blood clot is lodged and the amount of time the vessel has been blocked. The neural activity of these deprived cells can be severely compromised, jeopardizing the motor functions and/or the cognitive abilities of the patient. More than two-thirds of stroke survivors have some type of permanent disability [4].

1.3 Current Therapies

The fundamental objective of any therapy for stroke is the restoration of oxygenated blood flow downstream of the occlusion. Depending on the severity of the situation, the doctor may choose one of two kinds of treatment: non-invasive or invasive.

1.3.1 Non-Invasive Methods

Drugs are a simple way to quickly benefit a stroke patient and prevent potential strokes if the blood clot is detected early enough. This strategy is usually only effective within the first three hours of recognizing the symptoms, after which, hardening and adhesion become major challenges [5]. These treatments typically try to dissolve the clot with the use of anti-inflammatories or blood-thinners such as Aspirin [6].

Tissue plasminogen activator (TPA) is another non-surgical treatment that can produce benefits if administered early [6]. It is an enzyme that catalyzes the production of plasmin from plasminogen, another enzyme responsible for the breakdown of fibrin clots. This method is intravenous (administered in the venous system). In cases where the threat of permanent damage is less imminent, TPA can be administered through the arm. The aforementioned treatments are quick and simple if the conditions allow for them.

1.3.2 Invasive Methods

Unfortunately, not all strokes are caught soon enough to utilize a non-invasive method. For such cases, there are more urgent methods of remedy whose objective is to remove the clot. This is done by approaching the clot endovascularly (from within the blood vessel). As evident from the literature, endovascular stroke therapies constitute a rapidly changing field of research [7]. One of such therapies is called intra-arterial thrombolysis, which consists in removing a clot from an obstructed artery by dissolving it. A widely accepted procedure utilizes TPA, as discussed above, but rather than injecting the enzyme into the patients arm, the doctor applies the enzyme directly to the clotting site. This is typically done by threading a catheter from the groin through the vasculature of the patient up towards the brain, and then releasing the enzyme directly at the thrombus to expedite its effects. Even at its expedited rate, though, methods reliant on dissolving the thrombus may take up to two hours to be effective depending on the clot's calcification level [8].

Mechanical thrombectomy can be used in cases where the blood clot has grown too stiff or has adhered to arterial walls. These are cases in which tissue plasminogen activator (TPA) is largely ineffective. The doctor threads a catheter through the groin up to the clotting site. However, instead of carrying TPA to be ejected onto the clot, the catheter holds a metal stent or some other clot retrieval device. One such device, called the Merci[®] Retriever System [9], consists of a helical wire on the order of a few millimeters in diameter. Once the catheter reaches its destination at the clot interface, the wire is then effectively screwed into the clot and both the catheter and stent carrying the occlusion are removed from the body. An example of such a removal is depicted in Fig. 1.1.

The Merci[®] Retriever is not the only device of its type. Another popular, and more recent, retrieval device is the Solitaire[™] FR Revascularization Device manufactured by Covidien[™] [10]. The device is a tube-like mesh of free wires attached to one core wire, which is ejected from a microcatheter through the thrombus. Once it has pierced through, the removal procedure resembles that for the Merci[®] Retriever.

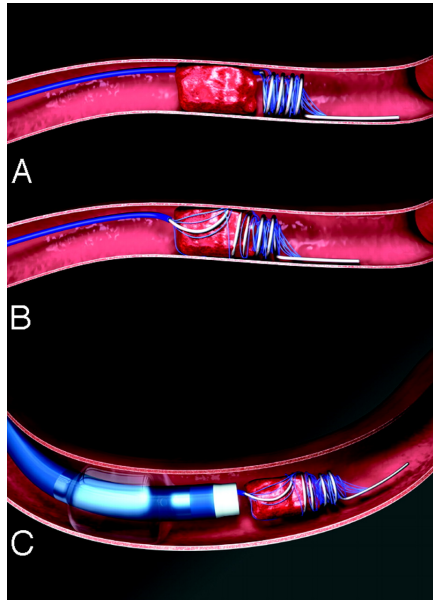


Figure 1.1: (A) Catheter pierces through the thrombus. (B) The Merci[®] Retriever spirals through. (C) Both the retriever and clot are removed from the body. Image from the American Journal of Neuroradiology [1].

1.3.3 Efficiency

The success rate of such mechanical methods is highly dependent upon the following three conditions: the stiffness of the clot, the location of the blockage, and the level of adhesion of the clot to arterial walls. If the blood clot has reached a hardness such that the guide wire of the catheter is unable to penetrate it, then the method fails. A clot situated between two branches of a cerebral artery causes complications for two reasons: the clot may block two passageways instead of just one, and the wire itself may pose the threat of damaging the arterial wall. Lastly, there is little that can be done to pull out a clot that is strongly attached to a vessel's endothelium. It is because of these conditions that clot retrieval systems like the Merci[®] Retriever or the Solitaire[™] FR Device are successful in only 60% of cases [8].

1.4 A New Concept in Clot-Removal Devices

Dr. Scott Simon, Professor of Neurosurgery at the Penn State Milton S. Hershey Medical Center in Hershey (PA), and his research group have proposed a new strategy to remove hard and strongly adhering blood clots using cyclic aspiration [11].

In a laboratory experiment, Dr. Simon manually applied alternating suction pressure, mediated through saline or blood, to the wall of clot-like substance in a silicone cerebral artery model and successfully removed the clot. This is done by threading a catheter up through the body, much like the procedure used in the aforementioned invasive methods, but instead of deploying a metal stent, the catheter carries an apparatus to deliver the suction pressure. This is depicted in Fig. 1.2. Dr. Simon

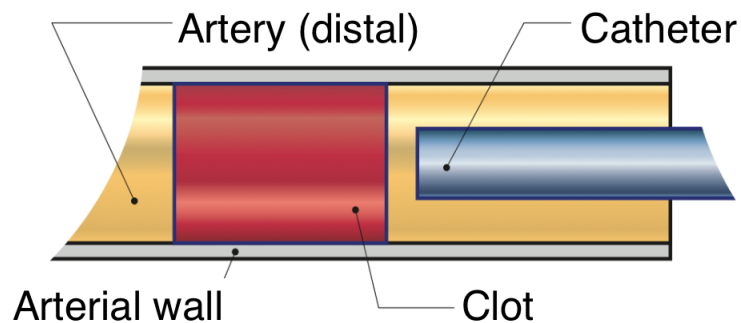


Figure 1.2: Schematic of catheter delivering alternating suction pressure to the face of a blood clot lodged in cerebral artery.

speculated two things: (i) that continuous aspiration does not yield the same efficacy of removal as does cyclic aspiration, and (ii) that *the driving force of dislodging the clot is the fatigue fracture of the clot at the inner radius of the arterial wall*. Overall, Dr. Simon proposes that applying an alternating pressure field on the proximal face of the clot would more successfully fatigue, fracture, and detach thrombi from an arterial wall than current mechanical thrombectomy procedures, no matter the level of adhesion or stiffness of the clot.

1.5 Mathematical and Numerical Modeling

The technique discussed in Section 1.4 offers a good example of a clinical application predicated on mechanical concepts such as deformation and fracture. The optimal conditions in terms of amplitude and frequency of the pressure wave imposed by the surgeon are likely to be patient-specific and not easily applied by a surgeon's hand. In this case, a mathematical model of the deformation and fracture behavior of a clot, in relation to local geometry and adhesion conditions, could be very useful in identifying operating conditions for the desired new clot removal device. This

is because a model would allow the examination of the role played by a variety of factors and parameters without the need to operate on a patient. First and foremost, the desired model would need to describe the mechanical response of a blood clot while surrounded on some surfaces by liquid blood. Furthermore, if the clot can be softened by some pharmacological intervention, the model in question would have to also describe the chemistry of blood whether in a clotted state or not. In the case of a stroke, one would also provide adequate models of the contact and adhesion of the clot with the arterial endothelium.

The example we have just described is one of very many examples in which the availability of a mathematical model of the mechanical and chemical response of blood would be decisive in the improvement or the development of therapeutic interventions involving the flow, clotting, and lysis of blood. In all of these cases, once a mathematical model of the blood behavior is formulated, further effort is needed to make the model usable in practice. This is usually achieved through the numerical implementation of the model and the development of software to carry out the task.

The current state of the art in blood modeling is often characterized by the use of a host of models tailored for specific events that may happen during the flow and chemical response of blood. That is, a model of blood flow is often distinct from that of clotting. The interplay of clotting on the flow conditions is typically managed with *ad hoc* schemes that must switch from one model to another at one spatial location at different times. From a numerical standpoint, this switching strategy, which is intrinsically discontinuous in nature, very likely results in the inability to provide reliable measures of approximation error if not in the serious deterioration of the overall predictive capability.

The objective of the current work is to consider a model for blood chemo-mechanics that can be applied to a range of blood states, and then explore a numerical implementation of the model with a single monolithic approach so as to offer a transparent analysis of the method's accuracy.

In the next section, we will review the existing literature and present the work that has motivated and helped formulate this study. Then, in the following chapters, we will discuss some existing fluid models and solve a two-dimensional example problem on one such model, specifically that of an Oldroyd-B fluid. We will reformulate this example problem using three descriptions: Eulerian, Lagrangian,

and arbitrary Lagrangian-Eulerian (ALE). For each formulation, we will propose a finite element method (FEM) implementation, starting with the statement of a convenient weak form, along with its computer implementation in COMSOL Multiphysics®. The latter is a commercially available piece of software for the solution of boundary value problems (BVPs) via the FEM. COMSOL Multiphysics® provides a variety of modules for the solution of specific physically-based problems. COMSOL Multiphysics® can also be used as a programming environment in which a user can develop a custom module whenever a commercial one is not available. As no ready-made module is available for the behavior of blood, the work presented herein required the development of a corresponding custom module.

The results of each module developed are verified via the Method of Manufactured Solutions [12]. We then take one step towards modeling the full biological response of blood by utilizing a continuum model for blood and solving the same system with this constitutive relation. Again, we formulate the problem using Eulerian, Lagrangian, and ALE frameworks, solve the system using COMSOL Multiphysics®, and present the results. Lastly, we will analyze the error in the outputs and discuss the next steps required to reach our goals of exploring the full system of flow, coagulation, and thrombolysis.

1.6 Literature Review

Blood, though foundational to the existence of advanced life forms, is an incredibly complex and confounding fluid from the perspective of scientists and engineers. To begin, blood is a heterogeneous mixture, composed of erythrocytes (red-blood cells), leukocytes (white-blood cells), and thrombocytes (platelets) suspended in an aqueous polymer solution, called plasma (see Fig. 1.3) [13]. In healthy human blood, plasma makes up about 55% of blood by volume and red-blood cells (RBCs) approximately make up the remaining 45%; white-blood cells (WBCs) and platelets combined make up only 1-2% of blood by volume [13]. These cells function to maintain *homeostasis* in the body, or the regulation of the extracellular fluid environment despite external environmental fluctuation: RBCs transport oxygen to and carbon-dioxide from cells, WBCs fight infection in the body, and platelets assist in clotting [14], a natural physiological response to blood loss due to vascular injury.

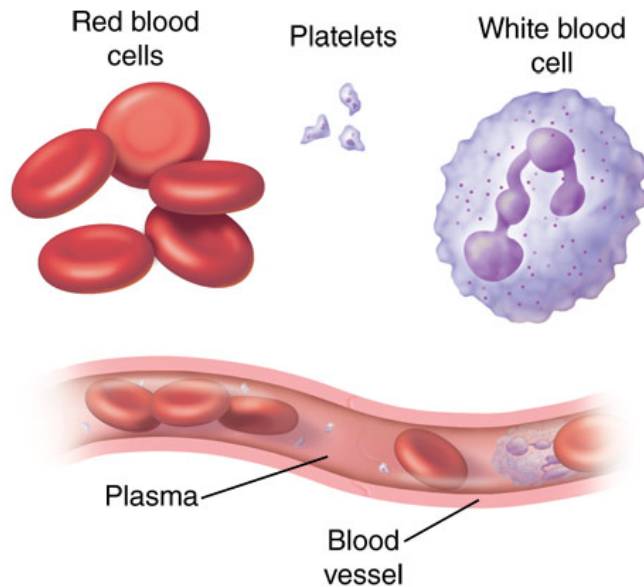


Figure 1.3: Illustration of the various components of blood. From Saint Luke’s Health System webpage.

In studies of biofluid mechanics, the most crucial piece of information to describing the flow of blood is its *constitutive equation* — a statement describing some physical property of a material [13]. In this case, the equation in question defines the relationship between the true stress and strain/strain rate of the material. The simplest of these constitutive relations for fluids include a non-viscous idealized fluid, a Newtonian viscous fluid, and a Hookean elastic solid [13]. Many rheological fluid models, including the Newtonian and Hookean materials, can be illustrated using mechanical analogues, representing the viscous and elastic components of stress by a dashpot and a spring, respectively, connected in either series or parallel. Some of these analogues are shown in Fig. 1.4.

The Newtonian fluid model, depicted by a single viscous dashpot, is often referenced in studies of fluid mechanics. Plasma, for example, is a well-known Newtonian fluid, meaning its shear stress is linearly proportional to the strain rate [13]. Yet, for whole blood, the constitutive relationship relating stress to strain and strain-rate is distinctly Non-Newtonian. Moreover, the relationship is heavily reliant upon the surrounding flow conditions. That is, variables such as vessel diameter and cell geometry have a massive effect on the mechanical response of blood. As plasma alone is linear viscous, the complex non-Newtonian nature of

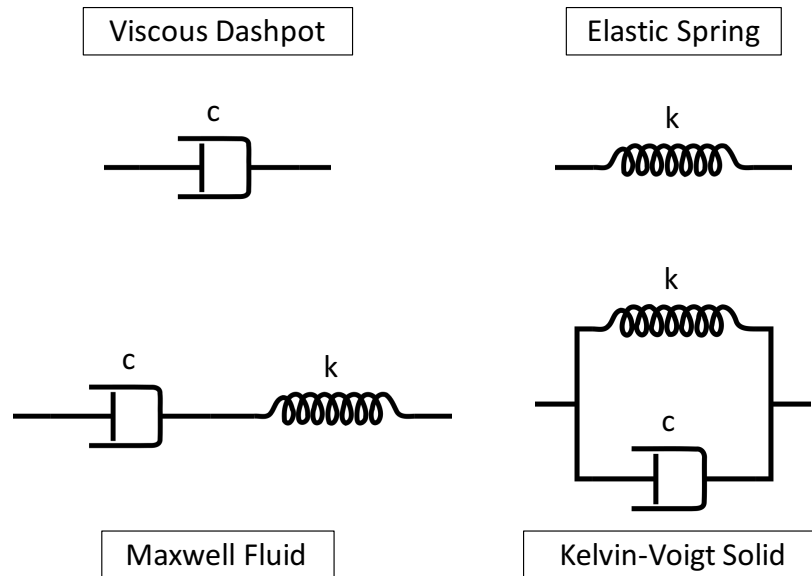


Figure 1.4: Common pictorial representations of viscous, elastic, and viscoelastic fluid/solid rheological models. Viscosity and spring constant given by c and k , respectively.

whole blood results from its cellular components.

In fact, some diseases and infections inhibit the functionality of blood *simply by altering the physical properties of these cellular components*. For example, the most severe form of malaria, caused by a parasite called plasmodium falciparum, makes RBCs “stiff and sticky”; the cells become more rigid and are found to adhere to vessel walls [15]. In healthy blood, these cells are highly deformable, as they must be able to traverse narrow capillaries to exchange carbon-dioxide for oxygen between cells in the body. Therefore, this parasite impairs blood circulation all by the structural mutation of RBCs. Clearly, as slight alterations to the physical properties of RBCs can compromise the function of the entire circulatory system, the daily performance of blood is nothing short of miraculous.

Furthermore, blood is unique to other fluids in that it has “living” components which can be stimulated to react to external factors. For example, clotting occurs to prevent blood loss and is triggered by platelet exposure to tissue factor (TF) from the damaged vessel wall. Clot formation involves platelet adhesion, chemical reactions, and species transport mechanisms, processes which are heavily influenced by hydrodynamic forces and the principles of mechanics [16]. For the above reasons, blood presents more challenges when it comes to mathematical modeling and

numerical implementation than commonly studied fluids, such as water or air.

RBCs are primarily responsible for the extreme variability of blood’s constitutive relationship. These cells are a thin, elastic membrane filled with fluid in the shape of a biconcave disc. They have a tendency to aggregate at low shear rates [17, 18], resulting in two side effects. First, these aggregates are “solid-like” objects with the ability to store elastic energy in their cell membranes, making blood a *viscoelastic* fluid. Viscoelastic materials are ones in which the features of stress relaxation, creep, and hysteresis under cyclic loading are present [13]. The fundamental viscoelastic models are the Maxwell and Kelvin-Voigt models, and their mechanical analogues can be seen in Fig. 1.4. Second, as the rate of shear increases, these clusters break up and the individual cells align with the flow, decreasing the apparent viscosity of blood [18], giving blood a shear-thinning nature.

In larger vessels where shear rates are high and individual particles are relatively small in relation to the vessel lumen, it may be appropriate to assume the viscosity of blood as a constant and the fluid as simply Newtonian, or linear viscous. However, in small vessels, such as capillaries, where the shear rate decreases, the constituents in blood are far more relevant to the flow characteristics as the size of the lumen approaches the size of the cells themselves. At these levels, blood exhibits strong non-Newtonian characteristics, influenced by the rate of shear, hematocrit (volume percentage of RBCs in blood), level of RBC aggregation and deformability, and temperature, among other factors [17, 18]. Due to the flow characteristics strong dependence on shear rate, many conflicting fluid models may satisfy the needs of a specific clinical application depending on the location of interest and pathology. For example, some published works, such as [19] and [20], serve the purpose of simply modeling the flow of blood through the body. Since these authors are focused on modeling the unrestricted flow of blood through relatively large arteries, they choose to model blood as a Newtonian fluid. Hence, the resulting governing equations are those of the traditional Navier-Stokes problem. While this assumption may be appropriate for the author’s applications, they are too simplistic for an all-purpose model, and we look to more appropriate continuum models.

In the mid-twentieth century, J. G. Oldroyd developed the first set of constitutive equations to describe the rheological behavior of viscoelastic fluids applicable to general three-dimensional problems [21]. His relationships, though novel at the time,

incorporate phenomena regarding fluid flow that had been previously neglected, e.g. that some fluid responses depend on their rheological history. These findings have radically influenced researchers in the field today. One such researcher, K. R. Rajagopal, expanded upon this endeavor to model complex fluids following a thermodynamic approach [22]. Rajagopal and his co-workers suggested that various materials are characterized by their energy storage and rate of dissipation functions, each governed by the evolution of the natural configuration of the body. These concepts are fully developed in [23] and [24] and are explained in greater detail in the next Chapter. Rajagopal has set the groundwork for a plethora of fluid models in [22], including a simple Maxwell model (see Fig. 1.4), and the classical Oldroyd-B fluid model, using his approach.

The Oldroyd-B model, discussed in the following Chapter, is prevalent in studies of blood [25–27] as it captures fluid’s Non-Newtonian behavior quite well over a wide range of shear rates [28]. One paper, by J. Hron, K. R. Rajagopal, and K. Tůma [29], studies the classical Oldroyd-B fluid under the balance of mass, and balance of linear momentum using the model derived in [22]. This holds particular significance for our purposes because not only does it propose a weak form of this problem for the Oldroyd-B fluid model using the Eulerian and Lagrangian frameworks (explanation of the Weak Formulation will come in the following Chapter), but it also provides a guideline for solving the governing equations of motion over an evolving domain using an ALE formulation. As we would ultimately like to describe the interaction between blood flow and the arterial wall motion, this feature is of specific importance to this group.

Anand and Rajagopal propose a generalization of the classical Oldroyd-B model in [30] that has gone on to serve as the basis for many projects applied to blood, including [17, 28, 31–37]. This model more accurately captures the deformation-dependence of the relaxation time of blood and its shear-thinning nature. However, one common theme links all of these projects. Each author assumes blood to be an incompressible fluid, and as such, a constraint must be enforced that ensures that the determinant of the deformation gradient from the material’s natural to its current configuration be equal to 1 (an explanation of these concepts can be found in Chapter 2). While these authors acknowledge the required constraint, not one publication enforces it rigorously in the formulation. One major contribution of this thesis is the explicit enforcement of this constraint without the addition of a

Lagrange multiplier to the system.

Rajagopal and Anand published a paper in *Pathophysiology of Haemostasis and Thrombosis* [32] in which they model the formation and lysis of blood clots taking the extrinsic pathway of coagulation into account. The paper incorporates both the mechanical and biochemical processes that contribute to the generation of blood clots by employing the generalized Oldroyd-B model and the advection-diffusion equation to link constituent concentrations to the flow. Blood clots, compared to whole blood, exhibit distinct responses to stress due to the presence of the constituents involved in the coagulation process. Hence, depending on the particular state of a blood sample, the viscous and elastic responses need to correspond to that state. That is, the dynamic viscosity of a clot will be substantially higher than that of liquid blood. According to the paper by Anand and Rajagopal [32], the models for blood and clots are similar in structure with the viscosity of the clot being even an order of magnitude greater than that of blood. As a first approximation, we will be ignoring the chemistry of blood (i.e., the reaction-convection-diffusion equations of this model) and focus only on the mechanical response of blood. We will also disregard the dependence on shear rate and deformation of the viscosity and take its value to be constant. The values we will use for the material parameters of blood clots are obtained from this paper, and these authors share much of the same content in [31].

In [28], Anand and his co-workers propose an enhanced version of generalized Oldroyd-B model documented in [30], the latter suffering from non-convergence of the residual error in solutions over complex geometries due to the discontinuous relaxation time and shear-thinning index. The enhancement is a power-law dependence in the rate of dissipation *coefficient* rather than on the entire term, resulting in a system that better aligns with experimental data, particularly for very low Reynolds number, and “start-up” flows. In future iterations of this project, we may find the employment of the proposed model in [28] more suitable to the situation at hand.

In summary, these published works play some role in the decisions made in this study. We gathered the necessary constitutive equations for modeling the behavior of a blood clot from [22] and [30]. We propose weak formulations of our own, while carefully considering the weak forms of the governing equations proposed by Hron *et al.* [29]. The parameter values for clotted blood were obtained from [35]. After

an introduction to the notation used throughout this document, we can begin our study with a brief background on common fluid models and by setting up our case-study problem on an Oldroyd-B fluid.

1.7 Notation

The three-dimensional Euclidean point space within which the motion of a physical body takes place is denoted by \mathcal{E}^3 . The associated translation (vector) space is denoted by \mathcal{V} . Scalar quantities, such as pressure or elastic modulus, will be denoted using italicized Latin and Greek letters, and are viewed as elements of \mathbb{R} , the set of real numbers. Vector quantities such as velocity or displacement will be denoted using boldface italicized symbols such as \mathbf{v} or $\boldsymbol{\xi}$, and they are viewed as elements of \mathcal{V} . Second order tensors will be denoted by boldface sans-serif symbols \mathbf{A} or $\boldsymbol{\tau}$ and they are understood to be elements of $\mathcal{L}(\mathcal{V}, \mathcal{V})$, by which we denote the space of linear operators from \mathcal{V} into \mathcal{V} . The set $\mathcal{L}^+(\mathcal{V}, \mathcal{V})$ is defined as follows:

$$\mathcal{L}^+(\mathcal{V}, \mathcal{V}) = \{\mathbf{A} | \mathbf{A} \in \mathcal{L}(\mathcal{V}, \mathcal{V}), \det \mathbf{A} > 0\}. \quad (1.1)$$

$\mathcal{L}^+(\mathcal{V}, \mathcal{V})$ therefore denotes the subset of second order tensors with positive determinant. Clearly, under the standard multiplication of tensors that makes $\mathcal{L}(\mathcal{V}, \mathcal{V})$ into an algebra, any element of $\mathcal{L}^+(\mathcal{V}, \mathcal{V})$ is invertible. Furthermore, while $\mathcal{L}^+(\mathcal{V}, \mathcal{V})$ is not a vector space, it does form a group.

The set $\mathcal{U}(\mathcal{V}, \mathcal{V})$ is defined as follows:

$$\mathcal{U}(\mathcal{V}, \mathcal{V}) = \{\mathbf{A} | \mathbf{A} \in \mathcal{L}(\mathcal{V}, \mathcal{V}), \det \mathbf{A} = 1\}. \quad (1.2)$$

The set $\mathcal{U}(\mathcal{V}, \mathcal{V})$ therefore denotes the subset of tensors with determinant equal to 1. This subset is referred to as the unimodular group and it is a subgroup of $\mathcal{L}^+(\mathcal{V}, \mathcal{V})$.

The set $\text{Sym}(\mathcal{V}, \mathcal{V})$ is defined as follows:

$$\text{Sym}(\mathcal{V}, \mathcal{V}) = \{\mathbf{A} | \mathbf{A} \in \mathcal{L}(\mathcal{V}, \mathcal{V}), \mathbf{A} = \mathbf{A}^T\}. \quad (1.3)$$

$\text{Sym}(\mathcal{V}, \mathcal{V})$ therefore denotes the subset of symmetric tensors.

The set $\text{Skw}(\mathcal{V}, \mathcal{V})$ is defined as follows:

$$\text{Skw}(\mathcal{V}, \mathcal{V}) = \{\mathbf{A} | \mathbf{A} \in \mathcal{L}(\mathcal{V}, \mathcal{V}), \mathbf{A} = -\mathbf{A}^T\}. \quad (1.4)$$

$\text{Skw}(\mathcal{V}, \mathcal{V})$ therefore denotes the subset of skewsymmetric tensors. We note that both $\text{Sym}(\mathcal{V}, \mathcal{V})$ and $\text{Skw}(\mathcal{V}, \mathcal{V})$ are proper subspaces of $\mathcal{L}(\mathcal{V}, \mathcal{V})$.

The inner product of two vectors \mathbf{a} and \mathbf{b} will be denoted by $\mathbf{a} \cdot \mathbf{b}$. The tensor product of two vectors \mathbf{a} and \mathbf{b} will be denoted by $\mathbf{a} \otimes \mathbf{b}$. Following standard definitions (cf. [38]), $\mathbf{a} \otimes \mathbf{b} \in \mathcal{L}(\mathcal{V}, \mathcal{V})$ such that

$$(\mathbf{a} \otimes \mathbf{b})\mathbf{c} = (\mathbf{b} \cdot \mathbf{c})\mathbf{a}, \quad \forall \mathbf{c} \in \mathcal{V}. \quad (1.5)$$

Similarly, given $\mathbf{A} \in \mathcal{L}(\mathcal{V}, \mathcal{V})$ and $\mathbf{b} \in \mathcal{V}$, the notation $\mathbf{A} \otimes \mathbf{b}$ will denote a third order tensor such that

$$(\mathbf{A} \otimes \mathbf{b})\mathbf{c} = (\mathbf{b} \cdot \mathbf{c})\mathbf{A}, \quad \forall \mathbf{c} \in \mathcal{V}. \quad (1.6)$$

The inner product of two second order tensors \mathbf{A} and \mathbf{B} will be denoted by $\mathbf{A} : \mathbf{B}$.

Time will be denoted by t , and the first and second order derivatives with respect to time will often be denoted by ∂_t and ∂_{tt} , respectively. The symbol ∇ will denote the gradient operator. Also, given a generic field (i.e., function of position) ϕ , $\nabla \cdot \phi$ will denote the divergence of ϕ . For convenience, letting $\phi(\mathbf{x})$ be some generic field ϕ function of position \mathbf{x} , the notations $\partial\phi/\partial\mathbf{x}$ and $\nabla\phi$ will be used interchangeably. That is

$$\frac{\partial\phi}{\partial\mathbf{x}} = \nabla\phi. \quad (1.7)$$

In some cases, it will be important to clearly identify the spatial variable with respect to which the gradient and divergence operators are computed. In these cases, the spatial variable in question will be placed as a subscript of the symbol ∇ , like in $\nabla_{\mathbf{x}}$ or $\nabla_{\mathbf{X}}$.

Given $\mathbf{A}(t) \in \mathcal{L}^+(\mathcal{V}, \mathcal{V})$ for all t in a convenient open interval of the real line, the time derivative of the determinant of $\mathbf{A}(t)$ has the following form (cf. [38]):

$$\partial_t \det[\mathbf{A}(t)] = \det[\mathbf{A}(t)] \text{tr}[\mathbf{A}^{-1} \partial_t \mathbf{A}(t)], \quad (1.8)$$

where $\text{tr} \mathbf{A}$ is the trace of \mathbf{A} .

Chapter 2 | Fluid Models & Oldroyd-B Example

This Chapter presents some existing fluid models, introducing the concept of evolving natural configuration of a body, as presented in [22]. Then, an initial/boundary value problem (IBVP) is formulated for one such fluid, namely the Oldroyd-B model. The same example problem is presented in three forms: Eulerian, Lagrangian, and arbitrary Lagrangian-Eulerian (ALE) to illustrate their differences. This chapter will serve as the framework for modeling clot behavior using the rheological clot model found in [30].

2.1 Existing Fluid Models for Blood

Blood's rheological characteristics are amazingly complex and highly variable due to the effects of its environment, flow velocity, and any pathological abnormalities. Depending on the application, a wide variety of fluid models may satisfy the criteria of the situation, some even contradictory.

2.1.1 Power Law Model

There are four common categories of fluid models (cf. [39, 40]): Newtonian, dilatant, pseudoplastic, and Bingham plastic. A Newtonian fluid is defined as a material whose stress is linearly proportional to its strain rate. For a one-dimensional

theological model, this can be expressed mathematically using the following relation:

$$\tau = \eta \nabla v, \quad (2.1)$$

where τ is fluid shear stress, η , referred to as the dynamic viscosity of the fluid, is the model's constant of proportionality, v is the fluid velocity, and ∇v is the strain rate, i.e., the gradient of the velocity.

Many common fluids, like, say, water, exhibit this simplistic relationship under ordinary conditions and are classified as Newtonian fluids. The three other categories of fluids, however, showcase more interesting attributes. Dilatant, also known as shear-thickening, fluids become more viscous when they are abruptly strained, while pseudoplastic, or shear-thinning, fluids become less viscous with higher strain rates. An example of each would be quicksand and toothpaste respectively. To conceptually describe the differences between the first three models discussed thus far, we can use the following one-dimensional power law representation:

$$\tau = \eta \text{sign}(\nabla v) |\nabla v|^\alpha, \quad \alpha > 0, \quad (2.2)$$

where, with $\xi \in \mathbb{R}$,

$$\text{sign}(\xi) = \begin{cases} 1, & \text{for } \xi \geq 0, \\ -1, & \text{for } \xi < 0. \end{cases} \quad (2.3)$$

When $\alpha = 1$, Eq. (2.2) describes a Newtonian fluid. For $\alpha > 1$, Eq. (2.2) describes a dilatant fluid, whereas for $0 < \alpha < 1$, it describes a pseudoplastic fluid.

Bingham plastic fluids demonstrate distinct behaviors compared to the last three — a certain yield stress must be first overcome before the fluid behaves like a Newtonian fluid. Denoting the threshold stress necessary for flow to occur by $\tau_y \in \mathbb{R}^+$, then, the shear stress of the material is modeled by a relation of the following type:

$$\begin{cases} \nabla v = 0, & \text{for } |\tau| \leq \tau_y, \\ \tau = \text{sign}(\nabla v) \eta (|\nabla v| + \tau_y), & \text{for } |\tau| > \tau_y. \end{cases} \quad (2.4)$$

As mentioned before, there is a vast literature on the modeling of blood. For example, blood is widely recognized to behave as a non-Newtonian fluid, in fact it exhibits clear shear-thinning behavior [41], but one can make the argument that it

can be modeled as a Newtonian fluid in some cases, e.g. if the blood constituents are sufficiently small compared to the diameter of the blood vessel.

2.1.2 Maxwell-Type Model

The four basic fluid models discussed above are one-dimensional rheological models convenient when trying to conceptually illustrate basic physical deformation mechanisms. In addition, said models do not contain all of the features needed to model blood behavior under a wide range of flow regimes or while undergoing clot formation or lysis. The three-dimensional generalization of these models is typically carried out with the use of continuum mechanics and thermodynamics.

Due to its rigor and applicability to the behavior of blood whether in the fluid or clotted states, here we present the model first proposed by K. R. Rajagopal and A. R. Srinivasa in [22]. In this model, blood is viewed as behaving as a viscoelastic fluid, i.e. a fluid with concurrent viscous and elastic responses to deformation. The abstract framework in which the model by Rajagopal and Srinivasa was developed is that of rational thermodynamics [42].

In [22], Rajagopal and Srinivasa derive several models for viscoelastic fluids with different energy storage functions, W , and rate-of-dissipation functions, ξ . The work in [22], based on the conceptual framework first proposed by J. G. Oldroyd in 1950 [21], served as the basis for over 200 studies since its publication, proving its vital contribution to the field.

The starting point for the construction of the model in [22] is that of *natural configuration* of a body. In Continuum Mechanics, a configuration is said to be *natural* when the free energy of the material achieves a minimum [43]. This definition is then shown to imply that the material in a natural configuration is stress free, or completely relaxed. When applied to a viscoelastic material, we then have that a natural configuration is one in which the fluid can be at rest, i.e., does not flow. With this premise, Rajagopal and co-workers have proposed that the rheological response of complex viscoelastic materials to applied loadings may include molecular rearrangements that cause the stress-free configuration of the material to *evolve* as function of the loading history.

Hence, along with a unique thermodynamic perspective, Rajagopal and co-workers posit that complex viscoelastic fluids should be modeled as materials

with *evolving natural configurations*. It is this concept that sets the work in [22] apart from those that had been previously derived. Borrowing the nomenclature used in [22], κ_R denotes the reference configuration of a body, and κ_t denotes its current configuration. The body's natural configuration is denoted by $\kappa_{p(t)}$. Following [22], a schematic illustrating these three configurations is given in Fig. 2.1. For a purely elastic body, there is only one natural configuration that the body

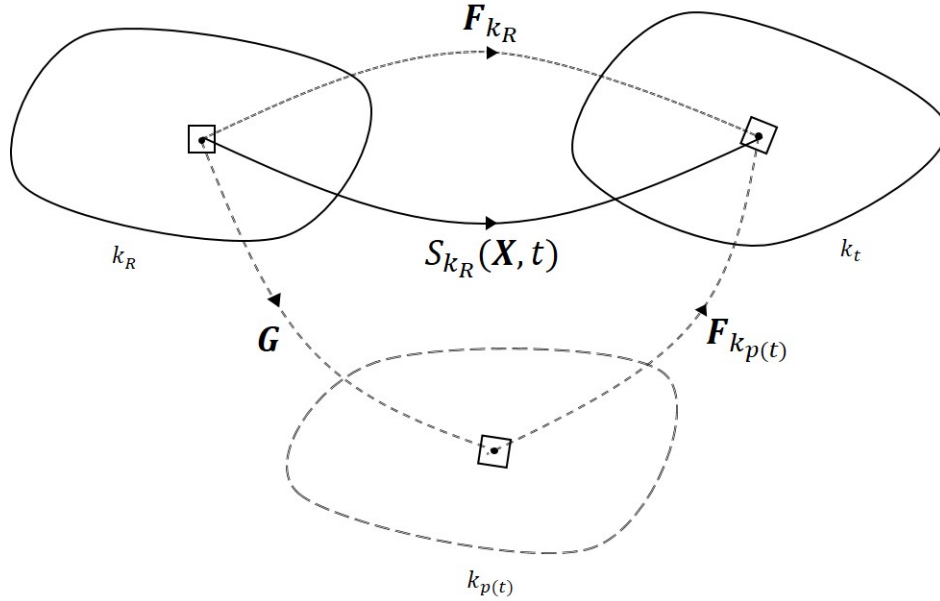


Figure 2.1: Schematic of the evolving natural configuration. The tensor \mathbf{F}_{κ_R} is the deformation gradient of the line elements surrounding a material point \mathbf{X} in the reference to those in the current configuration. Similarly, $\mathbf{F}_{\kappa_{p(t)}}$ is the deformation of the line elements in the natural configuration to the current one. The solid line from κ_R to κ_t , $S_{\kappa_R}(\mathbf{X}, t)$ is merely the motion of a material point, \mathbf{X} , through time.

recovers when the loads are removed, namely the reference configuration of the body, assuming that the latter is natural. On the other hand, for a purely plastic body which permanently deforms as stress is applied, there are infinitely many natural configurations, specifically being the evolving current configuration itself.

Many materials, including blood, do not simply fall into one of these two categories, but rather illustrate varying degrees of both. If the material response is not purely elastic or purely plastic, how can one identify the configuration to which the body relaxes from the current configuration? To answer this question, Rajagopal and Srinivasa postulated that the material conforms to the maximum

dissipation principle, that is, the body relaxes to a stress-free state through a deformation process for which *the pointwise rate of dissipation of the material is maximized* at each instant in time. The maximum dissipation principle has been used extensively in the study of plastic flow and an extended discussion can be found in [44].

Among those derived in [22], a Maxwell type fluid model is obtained through a distinct equation for the rate of dissipation for the fluid. In this case, the constitutive equation blends the rate of dissipation of a viscous Newtonian fluid with an assumption on the stored energy that resembles a neo-Hookean solid, the latter being a hyperelastic material [22].

The scalar dissipation rate and stored energy functions are given in the following form:

$$\hat{W} = \frac{\mu}{2}(I - 3), \quad (2.5)$$

$$\hat{\xi} = \eta \mathbf{D}_{\kappa_{p(t)}} : \mathbf{B}_{\kappa_{p(t)}} \mathbf{D}_{\kappa_{p(t)}}, \quad (2.6)$$

where μ is the elastic shear modulus, η is the dynamic viscosity, $\mathbf{D}_{\kappa_{p(t)}}$ represents the rate of change of the natural configuration of the body, $\mathbf{B}_{\kappa_{p(t)}}$ is the left Cauchy-Green stress tensor relative to the current natural configuration, and $I = \text{tr}(\mathbf{B}_{\kappa_{p(t)}})$, i.e., I is the first principal invariant of $\mathbf{B}_{\kappa_{p(t)}}$.

Applying these constitutive assumptions to the modeling of an incompressible Maxwell type fluid model, and following the procedure outlined in [22], one obtains

$$\mathbf{T} = -p\mathbf{I} + \mathbf{S}, \quad (2.7)$$

$$\mathbf{S} = \mu \mathbf{B}_{\kappa_{p(t)}}, \quad (2.8)$$

$$-\frac{1}{2} \overset{\nabla}{\mathbf{B}}_{\kappa_{p(t)}} = \frac{\mu}{\eta} (\mathbf{B}_{\kappa_{p(t)}} - \lambda \mathbf{I}), \quad (2.9)$$

where $\overset{\nabla}{\mathbf{B}}_{\kappa_{p(t)}}$, denotes the *upper convected time derivative* of $\mathbf{B}_{\kappa_{p(t)}}$. Denoting by \mathbf{L} the velocity gradient of the body, i.e., $\mathbf{L} = \nabla \mathbf{v}$, then the upper-convected time derivative of any tensor \mathbf{A} is defined as

$$\overset{\nabla}{\mathbf{A}} = \dot{\mathbf{A}} - \mathbf{L}\mathbf{A} - \mathbf{A}\mathbf{L}^T. \quad (2.10)$$

In Eqs. (2.7)–(2.9), \mathbf{T} is the Cauchy, or “true”, stress, p is a scalar multiplier responsible for the enforcement of the incompressibility condition, and λ is defined as:

$$\lambda = \frac{3}{\text{tr } \mathbf{B}_{\kappa_p(t)}^{-1}}. \quad (2.11)$$

The multiplier p is often erroneously referred to as the fluid pressure. In reality, p does not represent a measurable pressure experienced by the fluid, rather it takes on the units of a pressure and has an effect on the stress of the system. Only in the Navier-Stokes system for a linear-viscous and incompressible Newtonian fluid does the quantity p coincide with the empirically measurable pressure in the fluid.

2.1.3 Oldroyd-B Model

Starting again from [22], we explore another equation for the rate of dissipation, namely,

$$\hat{\xi} = \eta \mathbf{D}_{\kappa_p(t)} : \mathbf{B}_{\kappa_p(t)} \mathbf{D}_{\kappa_p(t)} + \eta_1 \mathbf{D} : \mathbf{D}, \quad (2.12)$$

where

$$\mathbf{D} = \text{Sym}(\mathbf{L}) = \frac{1}{2} [\nabla \mathbf{v} + (\nabla \mathbf{v})^T]. \quad (2.13)$$

The difference between this assumption and the one made for the Maxwell model is the extra dissipative term, specifically the quadratic relationship to the velocity gradient of the physical body, exhibiting further Newtonian dissipative behavior [22]. The term also introduces a second viscosity of the material, η_1 , which is the viscosity of the motion of the body and the viscosity that we are more familiar with. This variation on the dissipative equation, with the same stored energy function as with the Maxwell type model, results in the following set of constitutive equations:

$$\mathbf{T} = -p\mathbf{I} + \mathbf{S}, \quad (2.14)$$

$$\mathbf{S} = \mu \mathbf{B}_{\kappa_p(t)} + \eta_1 \mathbf{D}, \quad (2.15)$$

$$\mathbf{S} + \frac{\eta}{2\mu} \overset{\nabla}{\mathbf{S}} = \eta_1 \left(\mathbf{D} + \frac{\eta}{2\mu} \overset{\nabla}{\mathbf{D}} \right) + \mu \lambda \mathbf{I}. \quad (2.16)$$

This set of equations defines an Oldroyd-B fluid. All of the tensor and scalar quantities here match those discussed in the previous section.

One can express the above fluid model in the form used by Hron et al. in 2014 [29]. The full proof of equivalence can be found in Appendix A. The Oldroyd-B model used in [29] is

$$\mathbf{T} = -p\mathbf{I} + 2\eta\mathbf{D} + \mu(\mathbf{B} - \mathbf{I}), \quad (2.17)$$

$$\overset{\nabla}{\mathbf{B}} = \frac{1}{\tau}(\mathbf{I} - \mathbf{B}), \quad (2.18)$$

where τ is the relaxation time of the material, and the upper-convected derivative of \mathbf{B} can be simplified from Eq. (2.10) to

$$\overset{\nabla}{\mathbf{B}} = \partial_t \mathbf{B} + (\nabla \mathbf{B})\mathbf{v} - (\nabla \mathbf{v})\mathbf{B} - \mathbf{B}(\nabla \mathbf{v})^T \quad (2.19)$$

One should note that we have dropped the subscript on \mathbf{B} , but they are all understood to be $\mathbf{B}_{\kappa_p(t)}$, the left Cauchy-Green stress tensor of the deformation mapping the natural configuration to the current configuration. This notation will continue through the rest of this study.

2.2 Oldroyd-B Problem Setup

At this point, we will conduct a case study simulation using this classical Oldroyd-B fluid model with evolving natural configuration as declared in Eq. (2.18). This model is a simplification of the generalized model to be used for blood. Specifically, this model treats the relaxation time of the fluid as a constant, while the generalized model experiences deformation-dependent relaxation. The simplified model is applicable to blood in some situations, such as in high-shear flow regimes, and is an improvement to the simple Newtonian assumption. However, this model is only used for the purpose of study here; our desired blood model will be introduced in Chapter 5.

Any fluid motion must conform to the balance of mass and of momentum. As the material is assumed to be incompressible, the balance of mass reduces to a requirement that the material velocity field be divergence free (see, e.g., [43]). Hence, for the *strong form* of our problem, we have the following governing equations: incompressibility (Eq. (2.20)), the balance of linear momentum (Eq. (2.21)), and

the evolution of the natural configuration (Eq. (2.22)):

$$\nabla \cdot \mathbf{v} = 0, \quad (2.20)$$

$$\rho [\partial_t \mathbf{v} + (\nabla \mathbf{v}) \mathbf{v}] = \nabla \cdot \mathbf{T}, \quad (2.21)$$

$$\partial_t \mathbf{B} + (\nabla \mathbf{B}) \mathbf{v} - (\nabla \mathbf{v}) \mathbf{B} - \mathbf{B} (\nabla \mathbf{v})^T = \tau^{-1} (\mathbf{I} - \mathbf{B}), \quad (2.22)$$

with \mathbf{T} as defined in Eq. (2.17). The unknown quantities in the above model are the scalar multiplier p in Eq. (2.17), the vector velocity \mathbf{v} , and the strain tensor \mathbf{B} . These governing equations are provided in their Eulerian forms, the definition of which can be found in the following section.

For the purpose of solving the problem numerically via the finite element method (FEM), this problem now needs to be restated in its “weak form”. The idea here is to transform the differential equations of the strong form, denoted (S), into an equivalent set of integral equations with a reduction of the order of differentiation required to obtain the solution. This can be done by multiplying each equation by a set of “test” functions, integrating the new formula over the problem’s spatial domain, then using integration-by-parts to reduce the highest order of differentiation under the integral. The result is a set of integrals which are equivalent to the initial differential statement, and this is called the weak form of the problem, or (W).

Multiplying both sides of our equations in (S) by their corresponding test functions, then integrating over the current domain, Ω_x , we obtain the weak form as in [29]:

$$\int_{\Omega_x} (\nabla \cdot \mathbf{v}) \tilde{p} \, dv = 0, \quad (2.23)$$

$$\int_{\Omega_x} \rho [\partial_t \mathbf{v} + (\nabla \mathbf{v}) \mathbf{v}] \cdot \tilde{\mathbf{v}} \, dv - \int_{\Omega_x} (\nabla \cdot \mathbf{T}) \cdot \tilde{\mathbf{v}} \, dv = 0, \quad (2.24)$$

$$\int_{\Omega_x} [\partial_t \mathbf{B} + (\nabla \mathbf{B}) \mathbf{v} - (\nabla \mathbf{v}) \mathbf{B} - \mathbf{B} (\nabla \mathbf{v})^T + \tau^{-1} (\mathbf{B} - \mathbf{I})] : \tilde{\mathbf{B}} \, dv = 0, \quad (2.25)$$

with the Cauchy Stress, \mathbf{T} , written as

$$\mathbf{T} = -p \mathbf{I} + \eta (\nabla \mathbf{v} + (\nabla \mathbf{v})^T) + \mu (\mathbf{B} - \mathbf{I}). \quad (2.26)$$

\tilde{p} , $\tilde{\mathbf{v}}$, and $\tilde{\mathbf{B}}$ are the test functions for p , \mathbf{v} , and \mathbf{B} respectively, and they are taken

as elements of convenient functional spaces yet to be specified. Again, these weak contributions are Eulerian and come from the expressions for the incompressibility, balance of linear momentum, and evolution of the natural configuration, as defined in Eqs. (2.20)–(2.22).

As the body is assumed to be incompressible, its motion is *isochoric*, or volume-preserving. This assumption demands that the determinant of

$$\det \mathbf{B} = 1, \tag{2.27}$$

or $\mathbf{B} \in \mathcal{U}(\mathcal{V}, \mathcal{V})$. With this in mind, the only numerical implementations of this system discussed in the literature, namely those in [29] and [35], neglected to enforce this condition *explicitly*. That is, there is no statement in their systems ensuring that the determinant of \mathbf{B} stay equal to 1 for all possible physical scenarios. Recent personal communications with Prof. Srinivasa have confirmed that the constraint in question has turned out to be difficult to enforce and that no successful results are yet available in the literature.

In this thesis we propose to enforce Eq. (2.27) by adopting a well-known representation formula for elements of $\mathcal{U}(\mathcal{V}, \mathcal{V})$ in terms of elements of $\mathcal{L}^+(\mathcal{V}, \mathcal{V})$. In fact, recall that

$$\det(c\mathbf{A}) = c^3 \det(\mathbf{A}), \quad \forall \mathbf{A} \in \mathcal{L}(\mathcal{V}, \mathcal{V}) \text{ and } \forall c \in \mathbb{R}. \tag{2.28}$$

Then, rather than introducing another multiplier for the enforcement of Eq. (2.27), \mathbf{B} can be written using Eq. (2.28) as follows:

$$\mathbf{B} = J_G^{-1/3} \mathbf{G}, \quad \mathbf{G} \in \mathcal{L}^+(\mathcal{V}, \mathcal{V}), \tag{2.29}$$

where J_G is the determinant of \mathbf{G} . Equation (2.29) can be viewed as defining a map with domain $\mathcal{L}^+(\mathcal{V}, \mathcal{V})$ and co-domain $\mathcal{U}(\mathcal{V}, \mathcal{V})$. While only surjective, this map does guarantee that $\mathbf{B} \in \mathcal{U}(\mathcal{V}, \mathcal{V})$.

While seemingly simple, the proposed strategy for satisfying Eq. (2.27) represents a significant improvement relative to existing numerical implementations of the model chosen herein, as the behavior of $\det(\mathbf{B})$ is constrained to equal 1, no matter the flow regime.

The representation in (2.29) requires a corresponding representation for $\partial_t \mathbf{B}$,

appearing in Eq. (2.25):

$$\partial_t \mathbf{B} = \partial_t (J_G^{-1/3} \mathbf{G}) = J_G^{-1/3} \partial_t \mathbf{G} - \frac{1}{3} J_G^{-4/3} \partial_t J_G \mathbf{G}. \quad (2.30)$$

Using Jacobi's Formula and the definition of the adjugate matrix to express $\partial_t J_G$, we achieve the final form of $\partial_t \mathbf{B}$ with the representation of \mathbf{B} given in (2.29):

$$\partial_t \mathbf{B} = J_G^{-1/3} (\partial_t \mathbf{G} - \frac{1}{3} \text{tr}(\mathbf{G}^{-1} \partial_t \mathbf{G}) \mathbf{G}). \quad (2.31)$$

Given $\mathbf{G} \in \mathcal{L}^+(\mathcal{V}, \mathcal{V})$, for convenience, the notation $\mathbf{B}(\mathbf{G})$ will be used to denote the value of the right-hand side of Eq. (2.29). Then, we replace the problem defined by Eqs. (2.23)–(2.25) with the problem whose weak governing equations are

$$\int_{\Omega_x} (\nabla \cdot \mathbf{v}) \tilde{p} \, dv = 0, \quad (2.32)$$

$$\int_{\Omega_x} \rho [\partial_t \mathbf{v} + (\nabla \mathbf{v}) \mathbf{v}] \cdot \tilde{\mathbf{v}} \, dv - \int_{\Omega_x} (\nabla \cdot \mathbf{T}) \cdot \tilde{\mathbf{v}} \, dv = 0, \quad (2.33)$$

$$\begin{aligned} \int_{\Omega_x} [\partial_t \mathbf{B}(\mathbf{G}) + \nabla \mathbf{B}(\mathbf{G}) \mathbf{v} - \nabla \mathbf{v} \mathbf{B}(\mathbf{G}) - \mathbf{B}(\mathbf{G}) (\nabla \mathbf{v})^T \\ + \tau^{-1} (\mathbf{B}(\mathbf{G}) - \mathbf{I})] : \tilde{\mathbf{G}} \, dv = 0, \end{aligned} \quad (2.34)$$

with

$$\mathbf{T} = -p \mathbf{I} + \eta (\nabla \mathbf{v} + (\nabla \mathbf{v})^T) + \mu (\mathbf{B}(\mathbf{G}) - \mathbf{I}). \quad (2.35)$$

Using the product rule, $\nabla \cdot (\mathbf{A} \otimes \mathbf{b}) = (\nabla \cdot \mathbf{b}) \mathbf{A} + (\nabla \mathbf{A}) \mathbf{b}$, for all $\mathbf{A} \in \mathcal{L}(\mathcal{V}, \mathcal{V})$ and all $\mathbf{b} \in \mathcal{V}$. Therefore, under the stipulation that $\nabla \cdot \mathbf{v} = 0$,

$$(\nabla \mathbf{B}) \mathbf{v} = \nabla \cdot (\mathbf{B} \otimes \mathbf{v}). \quad (2.36)$$

Using Eq. (2.36) in conjunction with the divergence theorem (cf. [38]), the problem's finalized Eulerian weak form:

$$\int_{\Omega_x} (\nabla \cdot \mathbf{v}) \tilde{p} \, dv = 0, \quad (2.37)$$

$$\int_{\Omega_x} \rho [\partial_t \mathbf{v} + (\nabla \mathbf{v}) \mathbf{v}] \cdot \tilde{\mathbf{v}} \, dv + \int_{\Omega_x} \mathbf{T} : \nabla \tilde{\mathbf{v}} \, dv - \int_{\partial \Omega_x} \mathbf{T} \hat{\mathbf{n}} \cdot \tilde{\mathbf{v}} \, da = 0, \quad (2.38)$$

$$\int_{\Omega_x} [\partial_t \mathbf{B}(\mathbf{G}) - (\nabla \mathbf{v}) \mathbf{B}(\mathbf{G}) - \mathbf{B}(\mathbf{G})(\nabla \mathbf{v})^T + \tau^{-1}(\mathbf{B}(\mathbf{G}) - \mathbf{I})] : \tilde{\mathbf{G}} \, dv - \int_{\Omega_x} (\mathbf{B}(\mathbf{G}) \otimes \mathbf{v}) : \nabla \tilde{\mathbf{G}} \, dv + \int_{\partial\Omega_x} (\mathbf{B}(\mathbf{G}) \otimes \mathbf{v}) \hat{\mathbf{n}} : \tilde{\mathbf{G}} \, da = 0, \quad (2.39)$$

with

$$\mathbf{T} = -p\mathbf{I} + \eta(\nabla \mathbf{v} + (\nabla \mathbf{v})^T) + \mu(\mathbf{B}(\mathbf{G}) - \mathbf{I}), \quad (2.40)$$

$$\mathbf{B}(\mathbf{G}) = J_G^{-1/3} \mathbf{G}, \quad (2.41)$$

$$\partial_t \mathbf{B}(\mathbf{G}) = J_G^{-1/3} \left[\partial_t \mathbf{G} - \frac{1}{3} \text{tr}(\mathbf{G}^{-1} \partial_t \mathbf{G}) \mathbf{G} \right]. \quad (2.42)$$

In this formulation, $\partial\Omega_x$ denotes the boundary of our domain, and $\hat{\mathbf{n}}$ denotes the outward unit normal vector orienting $\partial\Omega_x$. One should note that the application of the divergence theorem on $\nabla \cdot (\mathbf{B} \otimes \mathbf{v})$ introduces a boundary contribution whose physical meaning is yet to be determined. This term needs to be further explored before solving this system under physiological boundary and initial conditions.

2.3 Motion Representation Frameworks

In mechanics, there are two main frameworks for the description of the motion of a physical system, Lagrangian and Eulerian. A third framework — the ALE description — is less common, but it gives a useful reformulation of a problem when neither the Lagrangian nor the Eulerian descriptions lead to robust numerical implementations, as it typically happens for fluid-structure-interaction or large deformation plastic flow problems.

An Eulerian framework is one in which the governing equations are defined over κ_t , the current configuration of the body. Recalling that $\kappa_t \subset \mathcal{E}^3$, the typical initial/boundary value problem (IBVP) in an Eulerian framework is posed over a *control volume*, the latter being defined as a time-independent subset of \mathcal{E}^3 , Ω , such that $\Omega \subset \kappa_t$ for all t is a given time interval of interest. Ω is sometimes referred to as a “window of observation.”

An Eulerian framework lends itself well to the formulation and solution of problems in fluid mechanics where we are typically interested in the fluid velocity at a point in space, for example, rather than the velocity of an individual fluid particle.

A Lagrangian framework, on the other hand, is one in which the governing equations are defined over $\kappa_R \subset \mathcal{E}^3$, the reference configuration of the body. In this framework, geometric points in κ_R can be uniquely identified with the material particles comprising the body. In solid mechanics, it is often required that the motion of individual particles from the reference configuration be computed. Therefore, the Lagrangian framework is the preferred one in the formulation of IBVP in solid mechanics.

There are many circumstances in which the numerical implementation of IBVP posed in an Eulerian or a Lagrangian framework suffer from severe pathologies [45]. For example in a regime of large deformations, the numerical approximation of the displacement field can easily end up predicting that the material is turned inside out. In the case of fluid structure interaction (FSI) problems, the boundary of the fluid domain is itself a time-dependent unknown of the problem. If such a problem is formulated within an Eulerian framework, the corresponding IBVP has a free boundary and, as such, presents significant challenges in its numerical formulation. On the other hand, a Lagrangian formulation of a fluid problem is characterized by deformation gradients that are almost singular, with a corresponding numerical representation that is essentially intractable.

When we must model both fluid and solid mechanics simultaneously, which framework do we choose? It turns out that the answer is neither an Eulerian nor a Lagrangian framework. Rather, the problem is reformulated so that the domain of the IBVP is the inverse image of a map whose range is κ_t and such that the map in question is computed to alleviate the numerical pathologies mentioned, and, as importantly, such that the inverse image of $\partial\kappa_t$ is known. This approach to the formulation of IBVP is referred to as an ALE formulation, and the map in question is referred to as the ALE map. It is important to keep in mind that this map is itself an unknown of the problem. That is, an ALE formulation has one more unknown field with respect to their Eulerian and Lagrangian counterparts. It therefore requires the statement of an additional governing equation that makes it possible to determine the ALE map. This additional equation is not dictated by physics, but by numerical convenience.

It is important to notice that both the Eulerian and Lagrangian formulations can be viewed as a special cases of an ALE formulation. Specifically, the Eulerian formulation can be viewed as an ALE formulation in which the ALE map is the

identity map. Similarly, a Lagrangian formulation can be viewed as an ALE formulation in which the ALE map is the (material) motion of the body. To demonstrate the consequences of each choice, we will reformulate and solve the above Eulerian Oldroyd-B problem using Lagrangian and ALE frameworks, comparing and contrasting all three solutions in the next chapter.

2.3.1 Lagrangian Formulation

To obtain the Lagrangian form of the Eulerian weak statement above, we perform a change of variables on Eqns. (2.37)–(2.39) from the current coordinates, \mathbf{x} , to the reference ones, \mathbf{X} . We begin by defining the transformation map from the reference to the current body, adopting the standard notation used in [29] and [46].

Let $\Omega_{\mathbf{x}}$ be the current domain, as in (W), and $\Omega_{\mathbf{X}}$ be the reference domain. We introduce a transformation map, $\varphi: \Omega_{\mathbf{X}} \rightarrow \Omega_{\mathbf{x}}$:

$$\varphi(\mathbf{X}, t) = \mathbf{x} = \mathbf{X} + \mathbf{u}, \quad (2.43)$$

where \mathbf{u} is the displacement of point \mathbf{X} . Here \mathbf{u} is defined as a function with κ_R as its domain. The (material) velocity, \mathbf{v} , is then

$$\mathbf{v} = \left. \frac{\partial \varphi(\mathbf{X}, t)}{\partial t} \right|_{\mathbf{X}} = \frac{\partial \mathbf{u}}{\partial t}. \quad (2.44)$$

Note that in this formulation, *the displacement \mathbf{u} replaces the velocity as our primary unknown*. This field, while explicitly present in our equations, will also be implicitly present in the variables \mathbf{F} , and J defined as follows:

$$\mathbf{F} = \frac{\partial \varphi(\mathbf{X}, t)}{\partial \mathbf{X}} = \mathbf{I} + \frac{\partial \mathbf{u}}{\partial \mathbf{X}} = \mathbf{I} + \nabla_{\mathbf{X}} \mathbf{u} \quad \text{and} \quad J = \det[\mathbf{F}]. \quad (2.45)$$

For an incompressible material, the Lagrangian form of the balance of mass simplifies to a condition that the determinant of the deformation gradient be equal to 1:

$$\frac{\partial \rho}{\partial t} + \nabla \cdot (\rho \mathbf{v}) = 0 \iff J = 1. \quad (2.46)$$

Next, we transform the spatial and total time derivatives in Eqns. (2.37)–(2.39). We begin by performing a change of variables on the gradients:

$$\nabla_{\mathbf{x}} \mathbf{v} = \frac{\partial \mathbf{v}}{\partial \mathbf{x}} = \frac{\partial \mathbf{v}}{\partial \mathbf{X}} \frac{\partial \mathbf{X}}{\partial \mathbf{x}} = \nabla_{\mathbf{X}} \mathbf{v} \mathbf{F}^{-1}. \quad (2.47)$$

Next, we express the total time derivative of quantity A , like \mathbf{v} in Eq. (2.38) or of \mathbf{B} in Eq. (2.39).

$$\dot{A} = \frac{\partial A}{\partial t} \Big|_{\mathbf{X}} = \frac{\partial A}{\partial t} \Big|_{\mathbf{x}} + \frac{\partial A}{\partial \mathbf{x}} \frac{\partial \mathbf{x}}{\partial t} \Big|_{\mathbf{X}} = \frac{\partial A}{\partial t} \Big|_{\mathbf{x}} + \nabla_{\mathbf{x}} A \cdot \mathbf{v}. \quad (2.48)$$

We handle the last term in Eq. (2.38) by applying a corollary of the Piola transformation [47], which states:

$$\hat{\mathbf{n}} \, da = J \mathbf{F}^{-\text{T}} \hat{\mathbf{n}}_{\mathbf{X}} \, dA, \quad (2.49)$$

where $\hat{\mathbf{n}}$ is the outward-pointing normal across the current boundary, and $\hat{\mathbf{n}}_{\mathbf{X}}$ is that across the referential boundary. Lastly, the volume integrals in Eqs. (2.37)-(2.39) are converted to integrals in $\Omega_{\mathbf{X}}$ by recognizing that a volume element in $\Omega_{\mathbf{x}}$ is a volume element in $\Omega_{\mathbf{X}}$ scaled by J .

$$dv = J \, dV. \quad (2.50)$$

The completed Lagrangian formulation of (W) , with the balance of mass replaced with Eq. (2.46) and under the assumption that \mathbf{u} is sufficiently regular so that $\partial_t \nabla_{\mathbf{X}} \mathbf{u} = \nabla_{\mathbf{X}} (\partial_t \mathbf{u})$, after the application of the divergence theorem, is:

$$\int_{\Omega_{\mathbf{X}}} (J - 1) \tilde{p} \, J \, dV = 0, \quad (2.51)$$

$$\begin{aligned} \int_{\Omega_{\mathbf{X}}} \rho \partial_{tt} \mathbf{u} \cdot \tilde{\mathbf{u}} \, J \, dV + \int_{\Omega_{\mathbf{X}}} \mathbf{T} \mathbf{F}^{-\text{T}} : \nabla_{\mathbf{X}} \tilde{\mathbf{u}} \, J \, dV \\ - \int_{\partial \Omega_{\mathbf{X}}} J \mathbf{T} \mathbf{F}^{-\text{T}} \hat{\mathbf{n}}_{\mathbf{X}} \cdot \tilde{\mathbf{u}} \, dA = 0, \end{aligned} \quad (2.52)$$

$$\begin{aligned} \int_{\Omega_{\mathbf{X}}} [\partial_t \mathbf{B}(\mathbf{G}) - (\nabla_{\mathbf{X}} \partial_t \mathbf{u}) \mathbf{F}^{-1} \mathbf{B}(\mathbf{G}) - \mathbf{B}(\mathbf{G}) \mathbf{F}^{-\text{T}} (\nabla_{\mathbf{X}} \partial_t \mathbf{u})^{\text{T}} \\ + \tau^{-1} (\mathbf{B}(\mathbf{G}) - \mathbf{I})] : \tilde{\mathbf{G}} \, J \, dV = 0, \end{aligned} \quad (2.53)$$

with

$$\mathbf{T} = -p \mathbf{I} + \eta \left[(\nabla_{\mathbf{X}} \partial_t \mathbf{u}) \mathbf{F}^{-1} + \mathbf{F}^{-\text{T}} (\nabla_{\mathbf{X}} \partial_t \mathbf{u})^{\text{T}} \right] + \mu (\mathbf{B}(\mathbf{G}) - \mathbf{I}), \quad (2.54)$$

and $\mathbf{B}(\mathbf{G})$ and $\partial_t \mathbf{B}(\mathbf{G})$ given by Eqs. (2.41) and (2.42), respectively. Recall that

our unknown fields are the scalar quantity p , the tensor quantity \mathbf{G} , and the vector displacement \mathbf{u} , hidden within \mathbf{F} and J .

2.3.2 ALE Formulation

As mentioned above, the ALE formulation is useful for problems where neither the Eulerian nor the Lagrangian framework is convenient. The numerical approximation is built on a computational domain that is not tied to the body's motion nor to its reference configuration. The ALE map, or “mesh motion”*, is selected to have a velocity equal to the material velocity on the boundary, but be the solution to a well-behaved differential equation on the interior; in this case, we use the Laplace equation. This solves the Lagrangian issue of mesh-entanglement when the fluid experiences turbulence within the domain, and the Eulerian limitation of fixed boundaries [29]. Note that this map introduces yet another unknown and weak contribution to the system for a total of four unknown variables.

To formulate the ALE problem, we will perform a change of variables on Eqs. (2.37)-(2.39) from the current configuration to the computational domain. Let our transformation $\hat{\varphi}: \Omega_{\boldsymbol{\chi}} \rightarrow \Omega_{\mathbf{x}}$ be defined by:

$$\hat{\varphi}(\boldsymbol{\chi}, t) = \mathbf{x} := \boldsymbol{\chi} + \hat{\mathbf{u}} \quad (2.55)$$

Here, $\hat{\mathbf{u}}$ is our ALE map, and it represents the displacement from point $\boldsymbol{\chi}$ to \mathbf{x} . As previously stated, in this thesis, this field will be determined as the solution to the Laplace equation on the interior of $\Omega_{\boldsymbol{\chi}}$, and its time derivative is equal to the material velocity on the boundary $\partial\Omega_{\boldsymbol{\chi}}$:

$$\begin{cases} -\nabla_{\boldsymbol{\chi}} \cdot (\nabla_{\boldsymbol{\chi}} \hat{\mathbf{u}}) = 0 & \text{in } \Omega_{\boldsymbol{\chi}}, \\ \partial_t \hat{\mathbf{u}} = \mathbf{v} & \text{on } \partial\Omega_{\boldsymbol{\chi}}. \end{cases}$$

Following the same procedure as in the Lagrangian case, we will introduce the deformation gradient from $\Omega_{\boldsymbol{\chi}}$ to $\Omega_{\mathbf{x}}$ and its determinant, $\hat{\mathbf{F}}$ and \hat{J} , respectively.

$$\hat{\mathbf{F}} = \frac{\partial \hat{\varphi}(\boldsymbol{\chi}, t)}{\partial \boldsymbol{\chi}} = \mathbf{I} + \frac{\partial \hat{\mathbf{u}}}{\partial \boldsymbol{\chi}} = \mathbf{I} + \nabla_{\boldsymbol{\chi}} \hat{\mathbf{u}} \quad ; \quad \hat{J} = \det[\hat{\mathbf{F}}]. \quad (2.56)$$

*This is an unfortunate name often used for the ALE map.

Next, we consider the velocity gradient:

$$\nabla_x \mathbf{v} = \frac{\partial \mathbf{v}}{\partial \mathbf{x}} = \frac{\partial \mathbf{v}}{\partial \boldsymbol{\chi}} \frac{\partial \boldsymbol{\chi}}{\partial \mathbf{x}} = \nabla_{\boldsymbol{\chi}} \mathbf{v} \hat{\mathbf{F}}^{-1}. \quad (2.57)$$

To express the total time derivative of a quantity A , we will first write the local time derivative.

$$\left. \frac{\partial A}{\partial t} \right|_{\boldsymbol{\chi}} = \left. \frac{\partial A}{\partial t} \right|_{\mathbf{x}} + \left. \frac{\partial A}{\partial \mathbf{x}} \frac{\partial \mathbf{x}}{\partial t} \right|_{\boldsymbol{\chi}} = \left. \frac{\partial A}{\partial t} \right|_{\mathbf{x}} + \nabla_x A \cdot \frac{\partial \hat{\mathbf{u}}}{\partial t}. \quad (2.58)$$

Subtracting the last term on the right-hand side and adding $\nabla_x A \cdot \mathbf{v}$ to both sides, we see that the total time derivative of A is

$$\dot{A} = \left. \frac{\partial A}{\partial t} \right|_{\mathbf{x}} + \nabla_x A \cdot \mathbf{v} = \left. \frac{\partial A}{\partial t} \right|_{\boldsymbol{\chi}} + \nabla_x A \cdot (\mathbf{v} - \partial_t \hat{\mathbf{u}}) = \left. \frac{\partial A}{\partial t} \right|_{\boldsymbol{\chi}} + (\nabla_x A) \cdot \hat{\mathbf{F}}^{-1} (\mathbf{v} - \partial_t \hat{\mathbf{u}}). \quad (2.59)$$

The final ALE formulation, after the application of the divergence theorem and including the weak contribution of the “mesh motion”, is:

$$\int_{\Omega_x} \nabla_x \cdot (\hat{\mathbf{F}}^{-1} \mathbf{v}) \tilde{p} \hat{J} dV = 0, \quad (2.60)$$

$$\begin{aligned} & \int_{\Omega_x} \rho \left[\partial_t \mathbf{v} + (\nabla_x \mathbf{v}) \cdot \hat{\mathbf{F}}^{-1} (\mathbf{v} - \partial_t \hat{\mathbf{u}}) \right] \cdot \tilde{\mathbf{v}} \hat{J} dV \\ & + \int_{\Omega_x} \hat{J} \hat{\mathbf{T}} \hat{\mathbf{F}}^{-T} : \nabla_x \tilde{\mathbf{v}} dV - \int_{\partial \Omega_x} \hat{J} \hat{\mathbf{T}} \hat{\mathbf{F}}^{-T} \hat{\mathbf{n}}_x \cdot \tilde{\mathbf{v}} dA = 0, \end{aligned} \quad (2.61)$$

$$\begin{aligned} & \int_{\Omega_x} \left[\partial_t \mathbf{B}(\mathbf{G}) - (\nabla_x \mathbf{v}) \hat{\mathbf{F}}^{-1} \mathbf{B}(\mathbf{G}) - \mathbf{B}(\mathbf{G}) \hat{\mathbf{F}}^{-T} (\nabla_x \mathbf{v})^T \right. \\ & \quad \left. + \tau^{-1} (\mathbf{B}(\mathbf{G}) - \mathbf{I}) \right] : \tilde{\mathbf{G}} \hat{J} dV \\ & - \int_{\Omega_x} \left[\mathbf{B}(\mathbf{G}) \otimes (\hat{\mathbf{F}}^{-1} (\mathbf{v} - \partial_t \hat{\mathbf{u}})) \right] : \nabla \tilde{\mathbf{G}} \hat{J} dV \\ & + \int_{\partial \Omega_x} \left[\mathbf{B}(\mathbf{G}) \otimes (\hat{\mathbf{F}}^{-1} (\mathbf{v} - \partial_t \hat{\mathbf{u}})) \right] \hat{\mathbf{n}} : \tilde{\mathbf{G}} \hat{J} dA = 0, \end{aligned} \quad (2.62)$$

$$\int_{\Omega_x} \nabla_x \hat{\mathbf{u}} : \nabla_x \tilde{\mathbf{u}} dV + \int_{\partial \Omega_x} \left[\frac{1}{\gamma h} (\mathbf{v} - \partial_t \hat{\mathbf{u}}) - (\nabla_x \hat{\mathbf{u}}) \hat{\mathbf{n}} \right] \cdot \tilde{\mathbf{u}} dA = 0 \quad (2.63)$$

where

$$\hat{\mathbf{T}} = -p \mathbf{I} + \eta ((\nabla_x \mathbf{v}) \hat{\mathbf{F}}^{-1} + \hat{\mathbf{F}}^{-T} (\nabla_x \mathbf{v})^T) + \mu (\mathbf{B}(\mathbf{G}) - \mathbf{I}), \quad (2.64)$$

and where $\mathbf{B}(\mathbf{G})$ and $\partial_t \mathbf{B}(\mathbf{G})$ are given by Eqs. (2.41) and (2.42), respectively. $\tilde{\mathbf{u}}$ is

now the test function for $\hat{\mathbf{u}}$, γ is a small positive parameter, and h is the local mesh diameter. The coefficient $1/(\gamma h)$ was chosen to conform to Nitsche's Method for the weak enforcement of Dirichlet boundary conditions [48]. As h is a small number as the FE mesh is sufficiently refined, and choosing γ to also be a sufficiently small number, $1/(\gamma h)$ weighs said boundary condition more heavily than the flux term arising from the application of the divergence theorem. Our four unknown quantities are the mesh motion $\hat{\mathbf{u}}$ (also hidden inside $\hat{\mathbf{F}}$ and $\hat{\mathcal{J}}$), the fluid velocity \mathbf{v} , the Lagrange multiplier p , and the tensor \mathbf{G} .

Chapter 3 | COMSOL Multiphysics® Inputs

Thus far, we have decided upon the set of differential equations that govern our example problem. We then transformed the Eulerian strong form of the problem, (S) , into its weak form, (W) , and reformulated the problem as both Lagrangian and arbitrary Lagrangian-Eulerian (ALE) using an ALE map that is the solution to the Laplace equation. Now, we begin the process of numerically solving these integral equations for our unknowns using COMSOL Multiphysics®. In this Chapter, we give the reader a brief introduction to the finite element method, describe the solver setup, and establish our verification procedure.

3.1 Introduction to the Finite Element Method

COMSOL Multiphysics® is a user-friendly simulation software that offers modules for the solution of a variety of physical problems along with a platform for the development of new finite element methods (FEMs)*. In Chapter 2, we have identified the strong form of our problem and its corresponding weak forms. Both the strong form and the weak form are equivalent statements of the original problem — a proof of which can be found in [49].

Using the notation in [49], to formulate the weak form of a set of governing equations, we first need to define two spaces of functions: one is called the solution space, \mathcal{S} , and the other is called the space of test functions, or \mathcal{V} . Denoting by Ω the spatial domain over which a problem is posed, for partial differential equations (PDEs) like the Poisson equation or the Navier equations (linear elasticity), both

*For an exhaustive presentation of the FEM see [49].

spaces carry functions that are $H^1(\Omega)$, meaning that said functions are square-integrable along with their first order derivatives over Ω . Many physics-based problems, i.e., problems based on balance laws, require a $H^1(\Omega)$ functional setting in their definition. Going back to \mathcal{S} and \mathcal{V} , let Γ denote the boundary of Ω . Let us consider traditional boundary conditions such that on some part of the boundary the values of the primary unknowns are prescribed whereas the values of co-normal derivatives are prescribed on the remaining part of Γ . The first type of boundary condition are called Dirichlet boundary conditions, whereas the second type are called Neumann boundary conditions. Let Γ_g and Γ_h denote the subsets of Γ where Dirichlet and Neumann boundary conditions are prescribed, respectively. To guarantee well-posedness of the initial/boundary value problem (IBVP) we must have

$$\Gamma_g \cap \Gamma_h = \emptyset \quad \text{and} \quad \Gamma_g \cup \Gamma_h = \Gamma. \quad (3.1)$$

With the above stipulation, the functions in \mathcal{S} differ from those in \mathcal{V} in that they are designed so as to satisfy the Dirichlet boundary conditions imposed on the solution while those in \mathcal{V} , called test functions, take on the homogeneous-counterpart to those boundary conditions, that is, they equal zero on Γ_g .

If the Dirichlet data are denoted as g , then we can define these spaces as

$$\mathcal{S} = \{u \mid u \in H^1, u|_{\Gamma_g} = g\}, \quad (3.2)$$

$$\mathcal{V} = \{w \mid w \in H^1, w|_{\Gamma_g} = 0\}. \quad (3.3)$$

The spaces \mathcal{S} and \mathcal{V} are infinite-dimensional; the number of integral equations necessary to solve a weak problem exactly in an infinite-dimensional context would be infinite. In order for the problem to be solved numerically, we must approximate the underlying infinite-dimensional function spaces with corresponding finite-dimensional spaces. The core concept underlying any FEM is to achieve the approximation of the function spaces by splitting our domain up into a finite number of subdomains, often referred to as elements. This partition is called a triangulation or a mesh. The size of these approximate spaces is dependent, among other things, on the mesh chosen, parameterized by a characteristic mesh length, h , called the mesh diameter, and representing the diameter of the hypersphere able to circumscribe the largest element. The finer the mesh, the larger the set of the test functions becomes. We label these finite subsets of the solution and test-function

spaces \mathcal{S}^h and \mathcal{V}^h respectively.

The weak formulation is converted into a discrete set of integral equations, and ultimately into an algebraic matrix equation. The transformation is outlined in [49]. The objective of the finite element method is to find the function $u^h \in \mathcal{S}^h$ that, for every test function $v^h \in \mathcal{V}^h$, satisfies the governing system of equations.

The test functions, v^h , are defined as the linear combination of a set of *shape functions*. These shape functions are typically Lagrange polynomials supported over patches of contiguous elements, meaning they are zero everywhere except over a specific patch. The shape function can be of varying degrees. Our choices of interpolating polynomials for each unknown field will be discussed in a later section.

3.2 Method of Manufactured Solutions

The computer implementation of a numerical method often suffers from programming errors. Hence, certain measures must be taken to ensure that the simulation software is solving the equations at hand correctly. This process is called *verification* and is not to be mistaken for a follow up process in computational software for physics-based problems called *validation*, or comparing the numerical predictions of a calculation with benchmark experiments to ascertain the limits within which the numerical solution is an acceptable predictor of an actual physical phenomenon.

The instinctual approach to code verification would be to compare the numerical results with an existing closed-form solution. However, for complex nonlinear problems, closed form solutions are seldom available. Hence, the necessity to develop a standard strategy for verification that does not rely on existing closed-form solution. The method of manufactured solutions (MMS) is such a strategy [50]. The method works as follows:

1. Select arbitrary functions for each of the unknown fields and declare such functions to be the exact solution to the problem.
2. Substitute said functions into the strong form of the governing equations and solve these equations for the source terms that are consistent with the selected exact solution.

3. Repeat the step above but this time to solve for the boundary and initial conditions that are consistent with the chosen exact solution.
4. Finally, input the derived source terms and boundary conditions into the code and check whether or not the corresponding numerical solution matches the set of functions selected at the outset of the procedure.

In order to check how well the solutions match, we use error norms to quantitatively describe the error of a solution. Denoting the exact and approximate solutions to a system u and u^h , respectively, the pointwise error in the approximate solution is $e = |u^h - u|$. Clearly, this is not an adequate indicator of global accuracy. Following a standard approach (cf. [49]), we then define a global measure of error as follows:

$$\|e\|_{L^2} = \sqrt{\int_{\Omega} (u^h - u)^2 dv}. \quad (3.4)$$

This definition is extended to vector and tensor quantities by replacing $(u^h - u)^2$ in Eq. (3.4) with the inner product of the difference between the approximate and exact solutions with itself. For functions whose gradient is square integrable, we also define a measure for the error in the approximation of the gradient. Specifically, we have

$$\|e\|_{H^1} = \sqrt{\int_{\Omega} (\nabla u^h - \nabla u) \cdot (\nabla u^h - \nabla u) dv}. \quad (3.5)$$

Again this definition is extended to vector and tensor quantities as indicated earlier. $\|e\|_{L^2}$ and $\|e\|_{H^1}$ are referred to as the L^2 -norm (read L -2-norm) and the H^1 -norm (read H -1-norm) of the error. From a strictly rigorous viewpoint, calling $\|e\|_{H^1}$ a *norm* is a misnomer, as it should be called a semi-norm [51]. The abuse of language, which is quite common in the literature, comes from the fact that sometimes $\|e\|_{H^1}$ can be proven to be also a norm depending on the specific definition of \mathcal{S} .

The ability to compute meaningful numerical approximations of the solution of a BVP is predicated upon the existence of bounds for the error in terms of a convenient measure of the givens of a problem. These bounds are called *error estimates* [51] and they may or may not be always available depending on the type of error at hand. For example, for the classic Poisson problem with pure Dirichlet data, there are well-defined error estimates in terms of both the L^2 -norm and the H^1 -norm [51]. By contrast, for the classic Stokes problem (creeping flow of fluids),

with velocity and pressure as principal unknowns, under pure Dirichlet boundary conditions for the velocity, there are estimates in terms of the L^2 -norm and the H^1 -norm for the error in the velocity, but only in terms of the L^2 -norm for the error in the pressure.

The establishment of error estimates for a specific problem is often a delicate analytical process. To this author’s best knowledge, rigorous error estimates for the problems considered in this thesis are not available from the literature. And the derivation of these estimates is beyond the current analytical skills of the author. However, the problem at hand has features that appear in both the classic Navier-Stokes problem as well as in the classic advection-diffusion equation. Therefore, in this thesis, the comparison between the approximate and exact solutions will be carried out in terms of the error norms that are meaningful in the aforementioned classical problems. Specifically, we will calculate the L^2 -norm of the error for each of our unknown quantities, and the H^1 norm of the error for only the velocity, displacement, and mesh-motion fields. We do not calculate the H^1 norm of the error for p or \mathbf{G} because the governing equations for these fields do not possess terms involving the inner-product of their gradients.

3.2.1 Manufactured Solutions

Each of the manufactured solutions were chosen with seven guidelines in mind that ensure the ease with which our numerical solutions can be computed. These guidelines can be found in the report on the MMS done by the Sandia National Laboratories [50]. For all three formulations (Eulerian, Lagrangian, and ALE), the problem and its associated solutions are defined over the same subset of \mathcal{E}^3 to ease the comparison later on. To describe position in \mathcal{E}^3 , we use a Cartesian coordinate system with coordinates x , y , and z . The elements of the corresponding induced basis for the translation space \mathcal{V} will be denoted by \hat{i} , \hat{j} , and \hat{k} . For computational convenience, the systematic code verification via the MMS will be carried for “plane-strain” problems*, whose domain is a square with side $L = 1$ m

*A *plane-strain* formulation (cf. [49]) is *mathematically* two-dimensional problem obtained from a physical three-dimensional problem by seeking solutions in which all the principal unknowns are assumed to be functions of only two of the three coordinates while behaving as constants in the remaining third coordinate.

in the xy -plane and such that

$$0 \leq x \leq L \quad \text{and} \quad 0 \leq y \leq L. \quad (3.6)$$

Note that the square domain in question represents a control volume in the Eulerian formulation, the body's reference configuration in the Lagrangian formulation, and a mere computational domain in the ALE formulation such that its boundaries coincide with the boundary of the reference configuration.

Before presenting the selected manufactured solutions, for ease of identification, the functions representing these solutions will be denoted by an 'MS' beginning tag standing for 'manufactured solution.'

3.2.1.1 Pressure

The solution for p , in all three formulations, is chosen to be a simple oscillating sinusoidal function, given in by,

$$\mathbf{MSp}(x, y, t) = p_0 \cos\left(2\pi \frac{t}{t_0}\right) \cos\left(2\pi \frac{x+y}{L}\right), \quad (3.7)$$

with $p_0 = 1$ Pa, $L = 1$ m, and $t_0 = 1$ s. This function is depicted in Fig. 3.1.

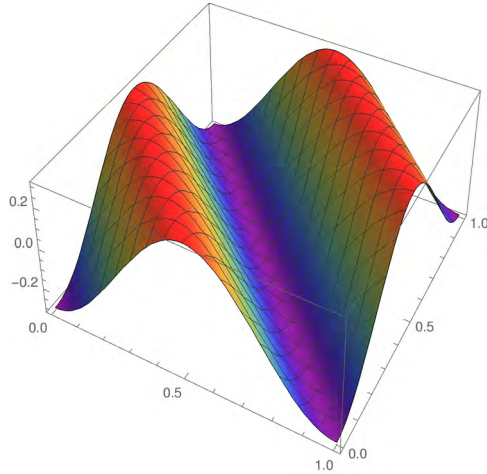


Figure 3.1: Plot of \mathbf{MSp} at time $t = 0.7$ s.

3.2.1.2 Velocities and Displacements

For the manufactured fields \mathbf{v} in the Eulerian, $\hat{\mathbf{u}}$ in the ALE, and \mathbf{u} in the Lagrangian formulation, we have selected the same form:

$$\mathbf{MSv}(x, y, t) = v_0 \sin\left(2\pi \frac{t}{t_0}\right) \left[\sin\left(2\pi \frac{x+y}{L}\right) \hat{i} + \cos\left(2\pi \frac{x-y}{L}\right) \hat{j} \right], \quad (3.8)$$

$$\mathbf{MSu}(x, y, t) = u_0 \sin\left(2\pi \frac{t}{t_0}\right) \left[\sin\left(2\pi \frac{x+y}{L}\right) \hat{i} + \cos\left(2\pi \frac{x-y}{L}\right) \hat{j} \right], \quad (3.9)$$

$$\mathbf{MS}\hat{\mathbf{u}}(x, y, t) = \hat{u}_0 \sin\left(2\pi \frac{t}{t_0}\right) \left[\sin\left(2\pi \frac{x+y}{L}\right) \hat{i} + \cos\left(2\pi \frac{x-y}{L}\right) \hat{j} \right], \quad (3.10)$$

where $v_0 = 0.01$ m/s, $u_0 = \hat{u}_0 = 0.01$ m, and \hat{i} , \hat{j} , \hat{k} are the base vectors of the underlying Cartesian coordinate system. The plot of the \hat{i} -component of these functions at time $t = 0.7$ s is given in Fig. 3.2. The velocity solution in the ALE

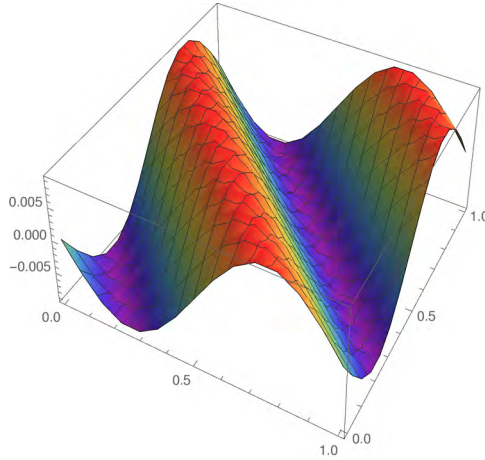


Figure 3.2: Plot of the \hat{i} -component of \mathbf{MSv} , \mathbf{MSu} and $\mathbf{MS}\hat{\mathbf{u}}$ at time $t = 0.7$ s.

formulations was chosen to be equal to the time derivative of $\mathbf{MS}\hat{\mathbf{u}}$ to automatically satisfy the imposed boundary constraint:

$$\mathbf{MSv}_A(x, y, t) = \frac{2\pi\hat{u}_0}{t_0} \cos\left(2\pi \frac{t}{t_0}\right) \left[\sin\left(2\pi \frac{x+y}{L}\right) \hat{i} + \cos\left(2\pi \frac{x-y}{L}\right) \hat{j} \right]. \quad (3.11)$$

Note that this choice is arbitrary and does not affect the solvability of this system; another choice would simply result in a source term not equal to zero for that constraint equation – see section on Manufactured Source Terms. The plot of this

function at time $t = 0.7$ s is given in Fig. 3.3.

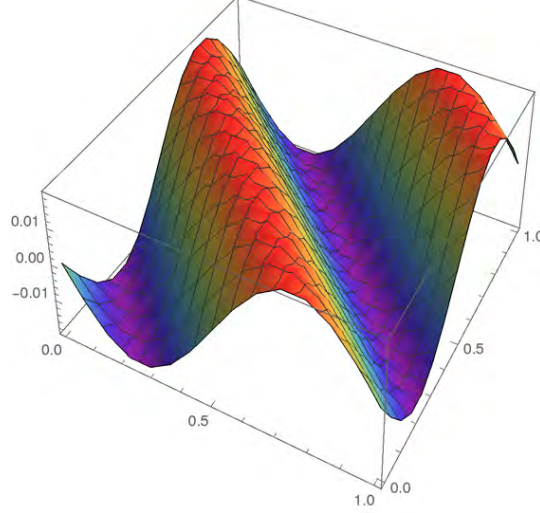


Figure 3.3: Plot of the \hat{i} -component of the \mathbf{MSv}_A at time $t = 0.7$ s.

3.2.1.3 Tensor \mathbf{G}

This selected field must be symmetric and have a determinant greater than zero, as the tensor \mathbf{B} in our formulation is defined as $J_G^{-1/3}\mathbf{G}$. This field was manufactured by generating an arbitrary 2×2 matrix, \mathbf{Gg} , then dividing each component by the square-root of its determinant, J_{Gg} , to obtain a 2×2 matrix with determinant equal to 1, \mathbf{GG} . Finally, this matrix is expanded to a 3×3 to match the *physical* dimension of the problem by setting the $\hat{k} \otimes \hat{k}$ component equal to 1. This must be the case since the *mathematical* problem is planar (two-dimensional). Ultimately, the manufactured field \mathbf{MSG} can be seen in (3.12), and has affine and sinusoidal components over the domain at each time step:

$$\begin{aligned} \mathbf{Gg} &= G_0 \left[\left(1 + \frac{x}{L}\right) \hat{i} \otimes \hat{i} + 0.1 \sin\left(2\pi \frac{t}{t_0}\right) \cos\left(2\pi \frac{x+y}{L}\right) \hat{i} \otimes \hat{j} \right. \\ &\quad \left. + 0.1 \sin\left(2\pi \frac{t}{t_0}\right) \cos\left(2\pi \frac{x+y}{L}\right) \hat{j} \otimes \hat{i} + \left(1 + \frac{y}{L}\right) \hat{j} \otimes \hat{j} \right], \\ \mathbf{GG} &= J_{Gg}^{-1/2} \mathbf{Gg}, \\ \mathbf{MSG} &= \left[GG_{ii} \hat{i} \otimes \hat{i} + GG_{ij} \hat{i} \otimes \hat{j} + GG_{ji} \hat{j} \otimes \hat{i} + GG_{jj} \hat{j} \otimes \hat{j} + 1 \hat{k} \otimes \hat{k} \right]. \end{aligned} \quad (3.12)$$

Here, $G_0 = 1$. The $\hat{i} \otimes \hat{i}$ component of \mathbf{MSG} is depicted in Fig. 3.4.

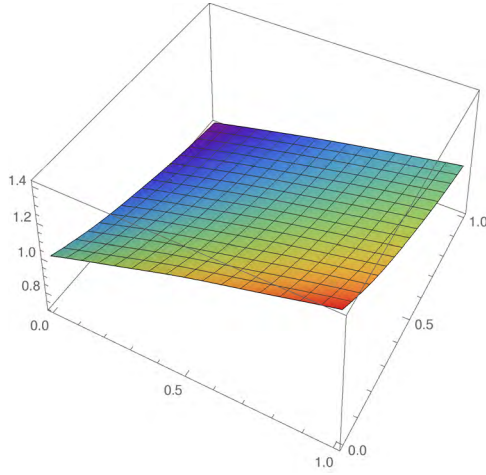


Figure 3.4: $\hat{i} \otimes \hat{i}$ component of **MSG** at time $t = 0.7$ s.

3.2.2 COMSOL Multiphysics[®] Inputs

Using *Mathematica*[®], we can generate the necessary parameter lists, field variables, source term variables, and weak contributions for the solution of the problem in COMSOL Multiphysics[®]. These fields are created from the inputs of the physics, the principle unknowns, and the three weak formulations.

As an example, the notebook converts the Eulerian interior weak contribution of the balance of linear momentum, i.e., the integrands over Ω_x of Eq. (2.38), from

$$\rho[\partial_t \mathbf{v} + (\nabla \mathbf{v})\mathbf{v}] \cdot \tilde{\mathbf{v}} + \mathbf{T} : \nabla \tilde{\mathbf{v}}, \quad (3.13)$$

to its scalar expansion in a COMSOL Multiphysics[®] compatible syntax with all terms properly expanded:

```
-(p*(test(v1x)+test(v2y)))+(mu*(G11*test(v1x)+G12*(test(v1y)
+test(v2x))+G22*test(v2y)-(-G12^2+G11*G22)^(1/3)*(test(v1x)
+test(v2y))))/(-G12^2+G11*G22)^(1/3)+rho*test(v1)*v1t
+rho*test(v1)*v1*v1x+rho*test(v1)*v1y*v2+rho*test(v2)*v2t
+rho*test(v2)*v1*v2x+rho*test(v2)*v2*v2y+eta*(2*test(v1x)*v1x
+(test(v1y)+test(v2x))*(v1y+v2x)+2*test(v2y)*v2y)-test(v1)*vEqS1
-test(v2)*vEqS2}
```

One should note that the outputted weak contribution is generated under given assumptions about the quantities involved. We have provided that the tensor \mathbf{G} is symmetric, and therefore G_{21} is equal to G_{12} . All cases of the former are replaced

by the latter. Furthermore, this outputted contribution includes the source term for the balance of momentum, which is not present in Eq. (2.38), but will be discussed in the next section.

3.2.2.1 Manufactured Source Terms

To implement the MMS, as stated before, we must manufacture solutions that follow a set of guidelines [50], then work backwards to obtain the source terms and auxiliary conditions that would produce our desired results. The full Eulerian strong form of our problem, with the source terms present, is

$$\nabla_{\mathbf{x}} \cdot \mathbf{v} = c_E, \quad (3.14)$$

$$\rho[\partial_t \mathbf{v} + (\nabla_{\mathbf{x}} \mathbf{v}) \mathbf{v}] - \nabla_{\mathbf{x}} \cdot \mathbf{T} = \mathbf{f}_E, \quad (3.15)$$

$$\partial_t \mathbf{B} + \nabla_{\mathbf{x}} \cdot (\mathbf{B} \otimes \mathbf{v}) - (\nabla_{\mathbf{x}} \mathbf{v}) \mathbf{B} - \mathbf{B} (\nabla_{\mathbf{x}} \mathbf{v})^T + \tau^{-1} (\mathbf{B} - \mathbf{I}) = \mathbf{A}_E, \quad (3.16)$$

supplemented by Eqs. (2.40)-(2.42). In the Lagrangian form, the strong form, with the corresponding source terms, becomes

$$J - 1 = c_L, \quad (3.17)$$

$$\rho \partial_{tt} \mathbf{u} - \nabla_{\mathbf{X}} \cdot (J \mathbf{T} \mathbf{F}^{-T}) = \mathbf{f}_L, \quad (3.18)$$

$$\partial_t \mathbf{B} - (\partial_t \nabla_{\mathbf{X}} \mathbf{u}) \mathbf{F}^{-1} \mathbf{B} - \mathbf{B} \mathbf{F}^{-T} (\partial_t \nabla_{\mathbf{X}} \mathbf{u})^T + \tau^{-1} (\mathbf{B} - \mathbf{I}) = \mathbf{A}_L, \quad (3.19)$$

along with Eq. (2.54) and Eqs. (2.41)-(2.42). Finally, the full ALE strong form, is

$$\nabla_{\mathbf{x}} \cdot (\hat{\mathbf{F}}^{-1} \mathbf{v}) = c_A, \quad (3.20)$$

$$\rho \partial_t \mathbf{v} + \nabla_{\mathbf{x}} \mathbf{v} \left[\hat{\mathbf{F}}^{-1} (\mathbf{v} - \partial_t \hat{\mathbf{u}}) \right] - \nabla_{\mathbf{x}} \cdot (\hat{J} \hat{\mathbf{T}} \hat{\mathbf{F}}^{-T}) = \mathbf{f}_A, \quad (3.21)$$

$$\begin{aligned} \partial_t \mathbf{B} + \nabla_{\mathbf{x}} \cdot \left[\mathbf{B} \otimes \left(\hat{\mathbf{F}}^{-1} (\mathbf{v} - \partial_t \hat{\mathbf{u}}) \right) \right] - (\nabla_{\mathbf{x}} \mathbf{v}) \hat{\mathbf{F}}^{-1} \mathbf{B} \\ - \mathbf{B} \hat{\mathbf{F}}^{-T} (\nabla_{\mathbf{x}} \mathbf{v})^T + \tau^{-1} (\mathbf{B} - \mathbf{I}) = \mathbf{A}_A, \end{aligned} \quad (3.22)$$

$$-\nabla_{\mathbf{x}} \cdot (\nabla_{\mathbf{x}} \hat{\mathbf{u}}) = \mathbf{w}_A, \quad (3.23)$$

supplemented by Eq. (2.64) and Eqs. (2.40)-(2.42). Substituting the chosen manufactured functions for p , \mathbf{v} , \mathbf{u} , $\hat{\mathbf{u}}$, and \mathbf{G} into their respective systems, we calculate the source terms. These calculations are tedious and prone to error, hence we use the symbol manipulation capability of *Mathematica*[®] to carry out this task.

3.2.2.2 Initial and Boundary Conditions

To calculate the initial conditions of each dependent quantity, we simply plug $t = 0$ into each of our solutions and obtain \mathbf{MSp}_i , \mathbf{MSv}_i , \mathbf{MSu}_i , $\mathbf{MS}\hat{u}_i$, and \mathbf{MSG}_i . Next, we gather our desired boundary conditions for the velocity. The Dirichlet data, defined on Γ_g , are retrieved by evaluating \mathbf{MSv} at the boundary, and the Neumann data, defined on Γ_h , are calculated via the Cauchy law [43]:

$$\mathbf{T}\hat{\mathbf{n}} = \mathbf{MSgh}, \quad (3.24)$$

where $\hat{\mathbf{n}}$ is the outward unit normal to the boundary and \mathbf{MSgh} is the desired Neumann datum vector field. For the sake of our case study, we will impose pure Dirichlet boundary conditions on \mathbf{v} (on \mathbf{u} in the Lagrangian case). That is, the exact solutions for \mathbf{v} and \mathbf{u} are prescribed on *entire* boundary in their respective systems. Because the solution for p is not unique with pure Dirichlet boundary conditions for \mathbf{v} or \mathbf{u} , we apply an additional constraint that says that the average of the quantity p equals 0, which is true of our manufactured solution.

Lastly, along with the material parameters, we have introduced a number of new constants in the creation of our manufactured solutions that must be understood by COMSOL Multiphysics[®], namely t_0 , L , p_0 , v_0 , u_0 , \hat{u}_0 , and G_0 . These constants and the auxiliary conditions are exported from *Mathematica*[®] into a text file and imported into COMSOL Multiphysics[®].

3.2.3 Solver Setup

To ensure the solution of our new system, we must make educated decisions about the procedural steps taken by COMSOL Multiphysics[®]. This regards the size and shape of our mesh, the shape functions chosen to represent the test functions, and most importantly, the time-integration solver. These choices are the factors which will be tested during our verification process.

3.2.3.1 Domain

The domain chosen for our two-dimensional verification analysis is a simple square of side length 1 m. We have chosen mapped quadrilateral mesh elements for their ease of implementation. The finite element method retrieves the exact value of the

solution at the nodes of the mesh. We interpolate the solution between the nodes via shape functions, typically Lagrange polynomials. In our verification analysis, we have chosen Lagrange linear elements for the pressure and strain in all three formulations. The velocity, displacement, and ALE map were approximated with Lagrange quadratic shape functions.

In the MMS, we define the end solution we wish to obtain. If we define the exact velocity solution to be planar, and then choose linear Lagrange polynomials as its shape functions, it is clear that the exact solution lies within the chosen solution space. This allows us to recover the true solution, no matter the mesh refinement. Choosing a sinusoidal manufactured solutions, we avoid this issue.

3.2.3.2 Time-Stepping

The FEM is used to approximate the problem over a domain at a *fixed point in time*. This reduces the problem to a system of ordinary differential equations in time which is then solved using a finite difference scheme. Our choice for the time-stepping scheme is an IDA solver with a variable-coefficient, variable-order backward differentiation formulas (BDF) to integrate over time. IDA solves a differential-algebraic equations (DAE) system of the following type [52]:

$$F(t, y, \dot{y}) = 0, \quad y(t_0) = y_0, \quad \dot{y}(t_0) = \dot{y}_0. \quad (3.25)$$

If y_0 and \dot{y}_0 are not provided by the user, this scheme attempts to compute a set of consistent initial conditions. The specific time integration scheme we used is adaptive BDF of variable order, q , between 1 and 5. The order is the number of previous solutions necessary to compute the next time step. The BDF formula is given in [52] as

$$\sum_{i=0}^q \alpha_{n,i} y_{n-i} = h_n \dot{y}_n, \quad (3.26)$$

where y_n and \dot{y}_n are the calculated solution and derivative at step n , and h_n is the current time step given by $t_n - t_{n-1}$. The coefficients, $\alpha_{n,i}$, depend on the BDF order, q , and the past step sizes [52].

There are many benefits to choosing a BDF time integration scheme. It is an adaptive method, meaning it fluctuates its time step size depending on the quality of the previous results. BDF integration is also fully implicit and unconditionally

stable. Furthermore, it is of variable order and therefore capable, to some degree, of adapting to the smoothness of the solution. Lastly, observing our system of equations, we can see that there is no differential operator on the field p anywhere, suggesting that our problem is a differential-algebraic; IDA is a DAE solver, as mentioned above, designed to handle problems like these.

In summary, our problem is one of an Oldroyd-B type fluid abiding by the conservation of mass, balance of linear momentum, and an evolution law. We have converted the strong form into its corresponding Eulerian, Lagrangian, and ALE weak forms, created arbitrary solutions to these problems, and worked backwards to solve for the necessary source terms, boundary conditions, and initial conditions. We have decided upon the desired time-integration scheme and domain, and implemented the code in COMSOL Multiphysics®. In the next Chapter, we will present the results of these calculations, and discuss the error incurred in each.

Chapter 4 | Oldroyd-B Results & Analysis

For each formulation of the problem, we have performed our verification analysis with five uniform mesh refinements, though only the first, third, and last refinements are shown to illustrate the resulting solution. The plots in this Chapter are of raw COMSOL Multiphysics® results, with no output data smoothing on the results for the purpose of plotting. The original form of our balance laws are Eulerian, so we begin the presentation of results with this trial.

4.1 Eulerian Results

Recall the plots of our manufactured solution for p , \mathbf{v} , and \mathbf{G} in Figs. 3.1, 3.2, and 3.4 respectively. The corresponding COMSOL Multiphysics® outputs of these fields, with various mesh diameters can be seen in Figs. 4.1–4.3, all at time $t = 0.7$ s.

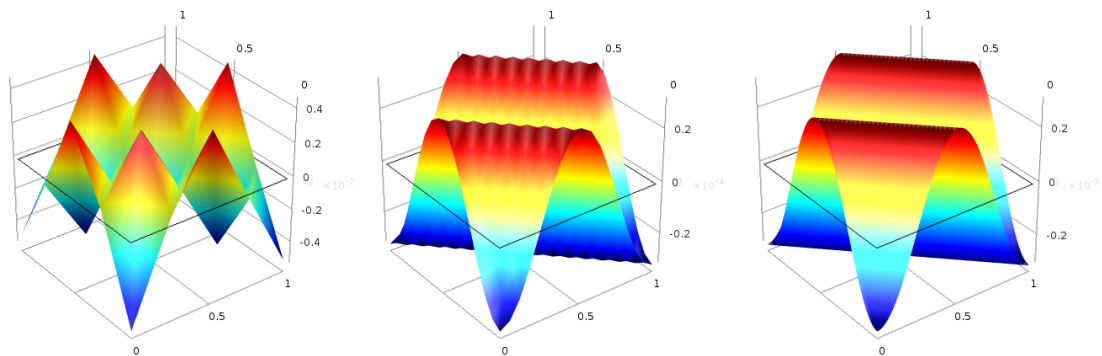


Figure 4.1: Numerical solution of p in Eulerian framework. Left to right: $h = 0.25$ m, $h = 0.0625$ m, and $h = 1.563 \times 10^{-2}$ m.

Since we know the exact solutions, we can calculate the L^2 and H^1 norms of the

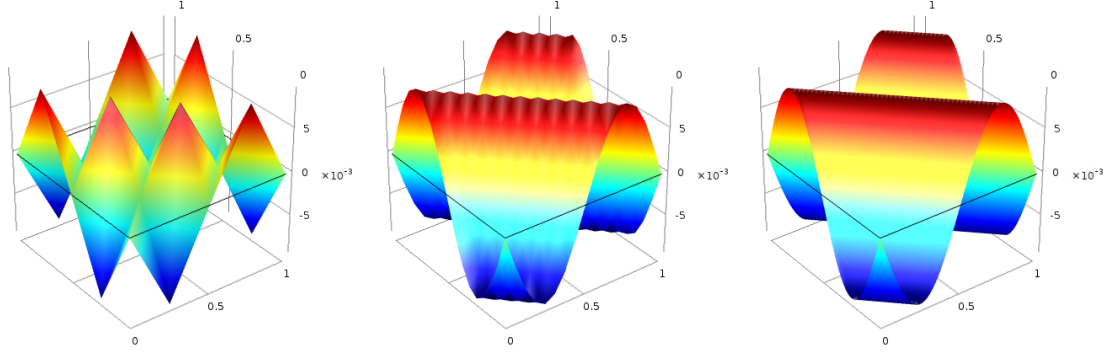


Figure 4.2: Numerical solution of \mathbf{v}_1 in Eulerian framework. Left to right: $h = 0.25$ m, $h = 0.0625$ m, and $h = 1.563 \times 10^{-2}$ m.

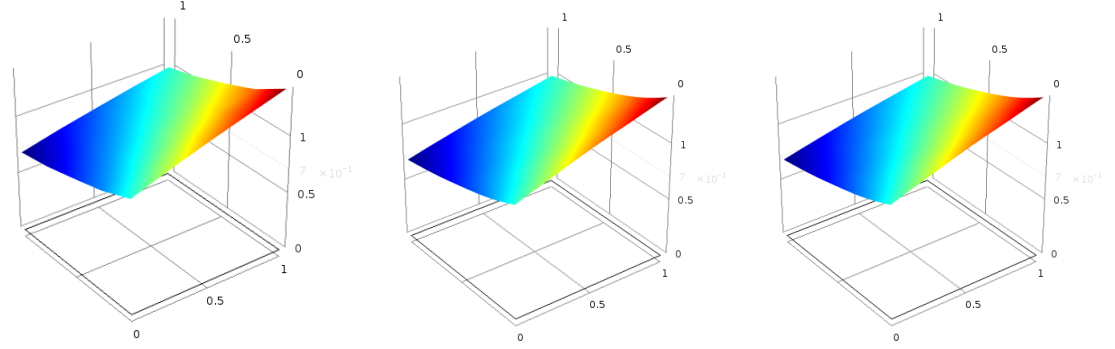


Figure 4.3: Numerical solution of \mathbf{G}_{11} in Eulerian framework. Left to right: $h = 0.25$ m, $h = 0.0625$ m, and $h = 1.563 \times 10^{-2}$ m.

error between the two, using Eqs. 3.4-3.5, at various characteristic mesh diameters. The magnitude of these errors are tabulated in Table 4.1.

Table 4.1: Error in numerical solution of p , \mathbf{v} , and \mathbf{G} in Eulerian framework.

h (m)	dof#	$\ e_p\ _{L^2}$	$\ e_v\ _{L^2}$	$\ e_v\ _{H^1}$	$\ e_G\ _{L^2}$
2^{-2}	262	4.882×10^{-4}	4.907×10^{-8}	6.887×10^{-5}	3.273×10^{-5}
2^{-3}	902	1.323×10^{-5}	1.122×10^{-10}	1.232×10^{-6}	9.337×10^{-7}
2^{-4}	3334	4.839×10^{-7}	4.836×10^{-13}	3.033×10^{-8}	3.472×10^{-8}
2^{-5}	12806	1.928×10^{-8}	3.398×10^{-15}	1.036×10^{-9}	1.390×10^{-9}
2^{-6}	50182	7.861×10^{-10}	3.131×10^{-17}	4.049×10^{-11}	5.712×10^{-11}

In Fig. 4.4, we have plotted the log of the inverse of the mesh length $-\log(\frac{1}{h})$ –

on the x-axis, and the log of these two norms of error on the y-axis. This way, we can visualize the convergence of the error as we refine the mesh for each unknown quantity.

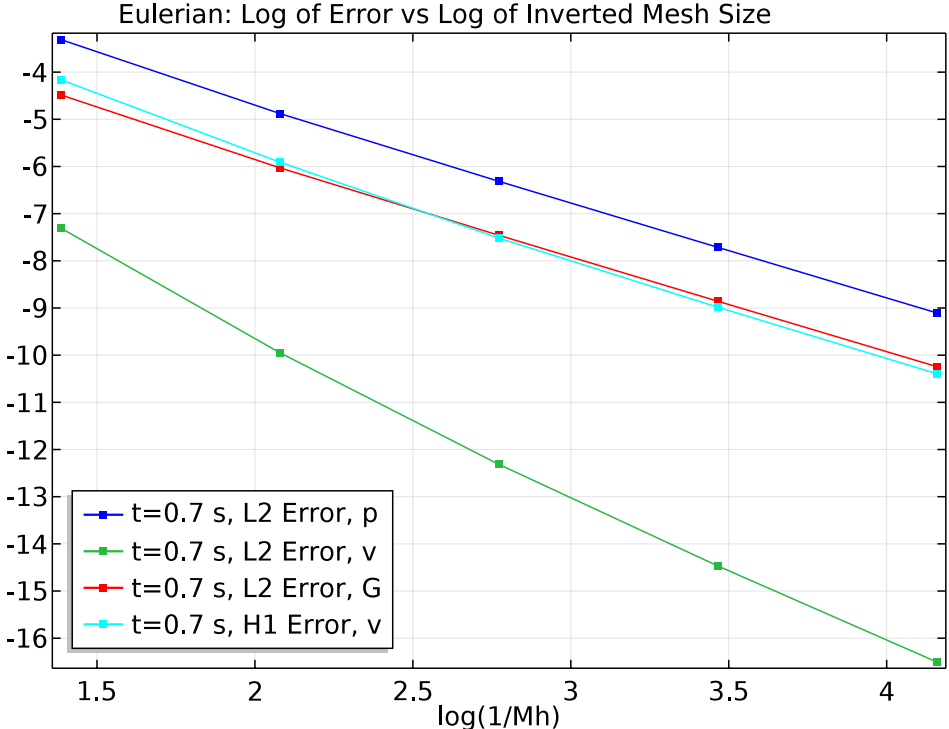


Figure 4.4: Plot of the L^2 and H^1 norms of error for p , \mathbf{v} , and \mathbf{G} — Eulerian.

4.2 Lagrangian Results

Recall the plots of our manufactured solution for p , \mathbf{u} , and \mathbf{G} in Figs. 3.1, 3.2, and 3.4 respectively. The corresponding COMSOL Multiphysics[®] outputs of these fields, with various mesh diameters can be seen in Figs. 4.5–4.7, all at time $t = 0.7$ s.

The magnitude of the L^2 and H^1 errors incurred in this formulation are tabulated in Table 4.2

Plotting the log of these norms versus the log of the inverse of the mesh length, we obtain a convergence plot of the error in the Lagrangian-formulation quantities in Fig. 4.8.

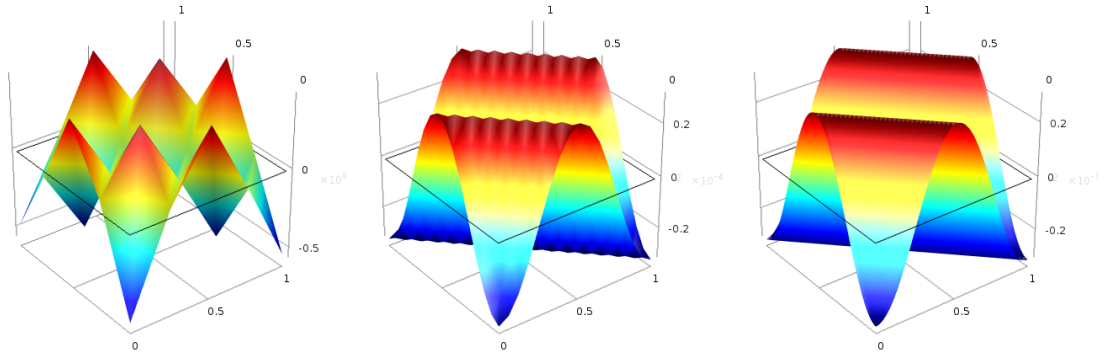


Figure 4.5: Numerical solution of p in the Lagrangian framework. Left to right: $h = 0.25$ m, $h = 0.0625$ m, and $h = 1.563 \times 10^{-2}$ m.

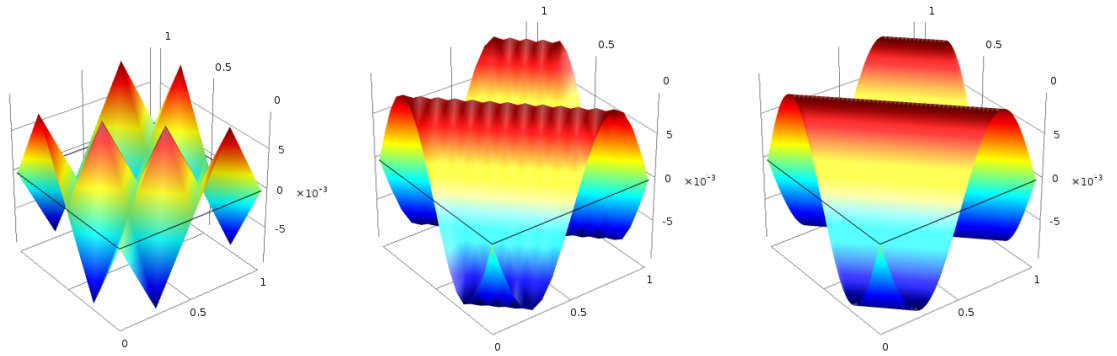


Figure 4.6: Numerical solution of u_1 in the Lagrangian framework. Left to right: $h = 0.25$ m, $h = 0.0625$ m, and $h = 1.563 \times 10^{-2}$ m.

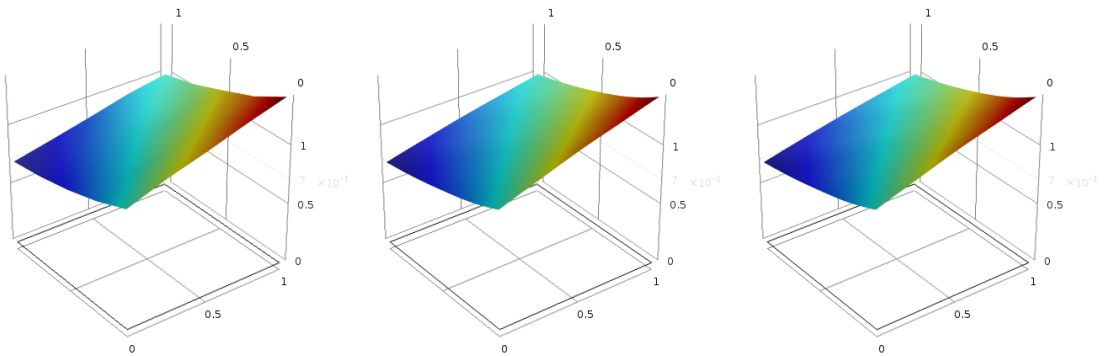


Figure 4.7: Numerical solution of \mathbf{G}_{11} in Lagrangian framework. Left to right: $h = 0.25$ m, $h = 0.0625$ m, and $h = 1.563 \times 10^{-2}$ m.

Table 4.2: Error in numerical solution of p , \mathbf{u} , and \mathbf{G} in Lagrangian framework.

h (m)	dof#	$\ e_p\ _{L^2}$	$\ e_u\ _{L^2}$	$\ e_u\ _{H^1}$	$\ e_G\ _{L^2}$
2^{-2}	262	5.173×10^{-4}	1.245×10^{-8}	2.228×10^{-5}	3.501×10^{-5}
2^{-3}	902	1.328×10^{-5}	5.528×10^{-11}	6.606×10^{-7}	9.387×10^{-7}
2^{-4}	3334	4.841×10^{-7}	3.797×10^{-13}	2.439×10^{-8}	3.458×10^{-8}
2^{-5}	12806	1.928×10^{-8}	3.006×10^{-15}	9.732×10^{-10}	1.382×10^{-9}
2^{-6}	50182	7.876×10^{-10}	2.480×10^{-17}	3.968×10^{-11}	5.640×10^{-11}

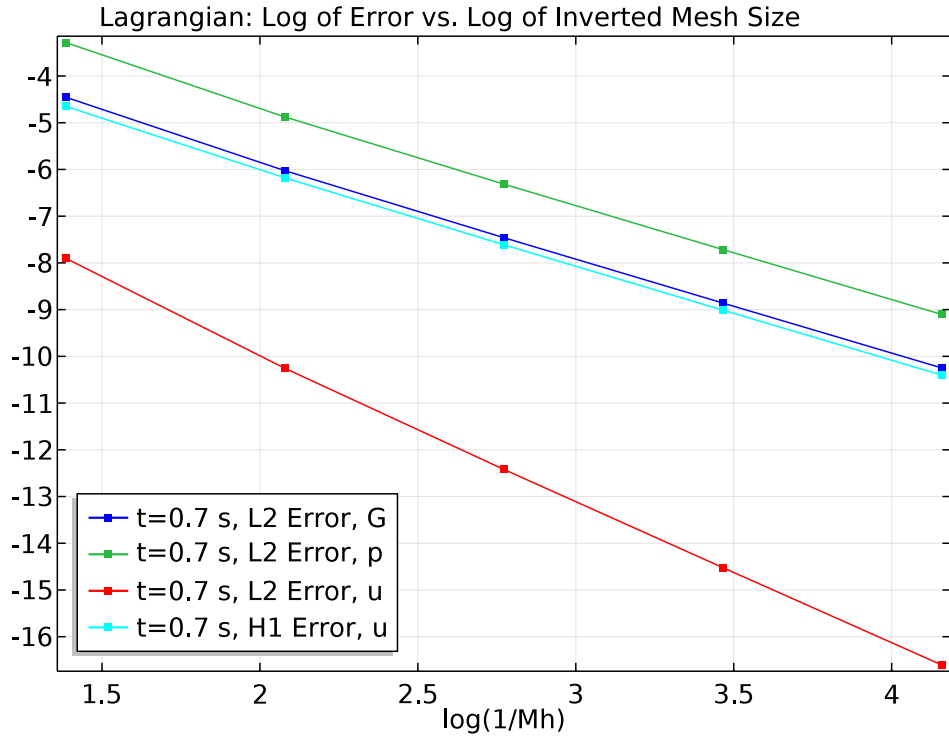


Figure 4.8: Plot of the L^2 and H^1 norms of error for p , \mathbf{u} , and \mathbf{G} — Lagrangian.

4.3 ALE Results

Recall the plots of our manufactured solution for p , \mathbf{v} , $\hat{\mathbf{u}}$ and \mathbf{G} in Figs. 3.1, 3.3, 3.2, and 3.4 respectively. The corresponding COMSOL Multiphysics[®] outputs of these fields, with various mesh diameters can be seen in Figs. 4.9–4.12.

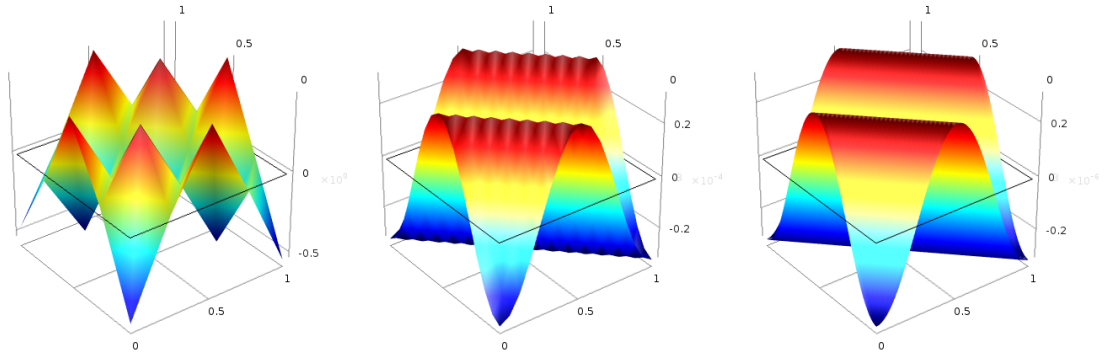


Figure 4.9: Numerical solution of p in ALE framework. Left to right: $h = 0.25$ m, $h = 0.0625$ m, and $h = 1.563 \times 10^{-2}$ m.

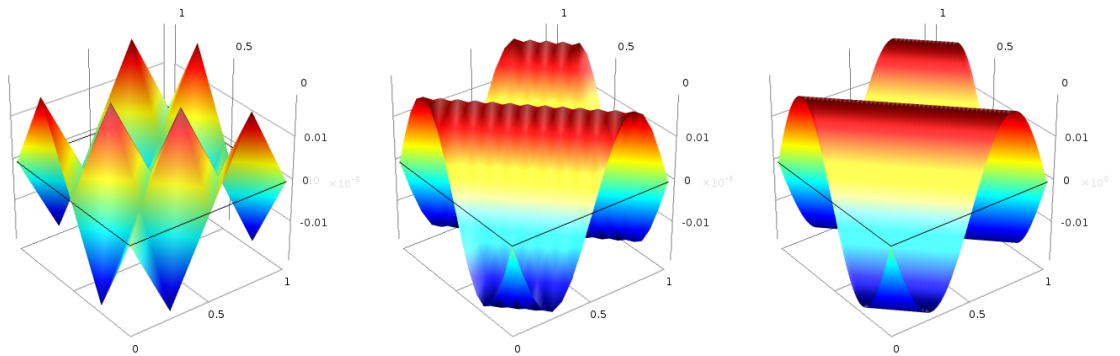


Figure 4.10: Numerical solution of \mathbf{v} in ALE framework. Left to right: $h = 0.25$ m, $h = 0.0625$ m, and $h = 1.563 \times 10^{-2}$ m.

The magnitude of the L^2 and H^1 errors incurred in this formulation are tabulated in Table 4.3 and Table 4.4. Plotting the log of these norms versus the log of the inverse of the mesh length, we obtain Fig. 4.13.

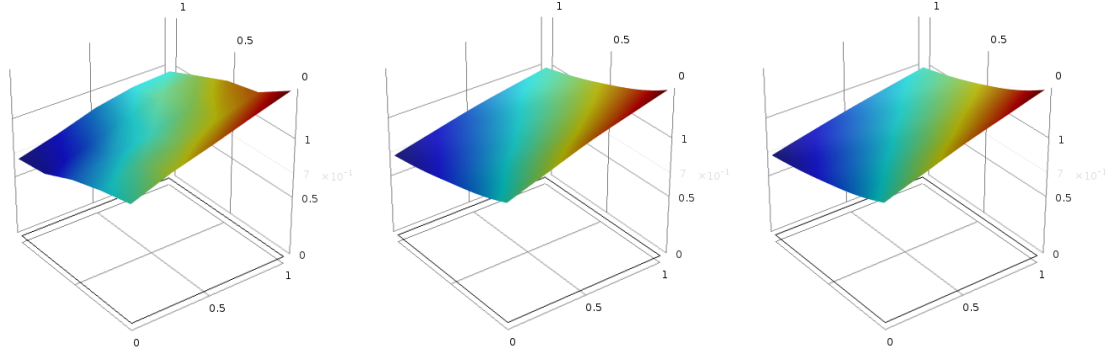


Figure 4.11: Numerical solution of \mathbf{G} in ALE framework. Left to right: $h = 0.25$ m, $h = 0.0625$ m, and $h = 1.563 \times 10^{-2}$ m.

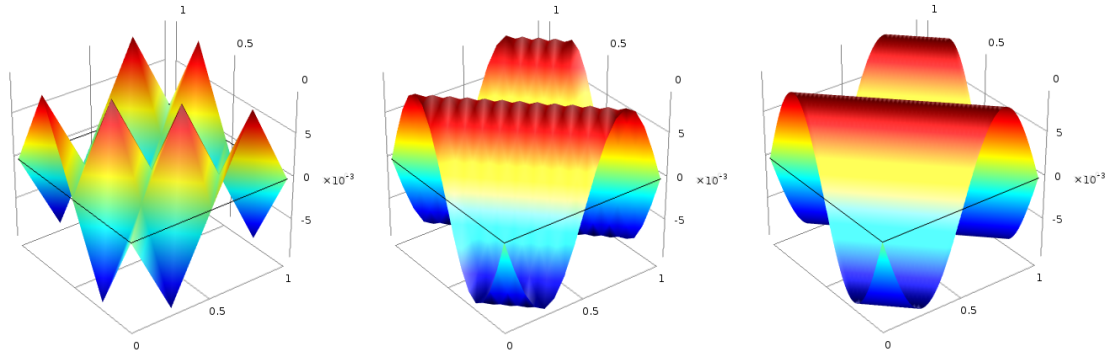


Figure 4.12: Numerical solution of $\hat{\mathbf{u}}$ in ALE framework. Left to right: $h = 0.25$ m, $h = 0.0625$ m, and $h = 1.563 \times 10^{-2}$ m.

Table 4.3: Error in numerical solution of p , \mathbf{v} , and \mathbf{G} in ALE framework.

h (m)	dof#	$\ e_p\ _{L^2}$	$\ e_v\ _{L^2}$	$\ e_v\ _{H^1}$	$\ e_{\mathbf{G}}\ _{L^2}$
2^{-2}	592	5.045×10^{-4}	4.62×10^{-8}	1.052×10^{-4}	1.404×10^{-4}
2^{-3}	2104	1.326×10^{-5}	2.465×10^{-10}	3.424×10^{-6}	7.709×10^{-6}
2^{-4}	7912	4.837×10^{-7}	1.876×10^{-12}	1.271×10^{-7}	3.666×10^{-7}
2^{-5}	30664	1.927×10^{-8}	1.537×10^{-14}	5.047×10^{-9}	1.576×10^{-8}
2^{-6}	120712	7.855×10^{-10}	1.275×10^{-16}	2.054×10^{-10}	6.556×10^{-10}

Table 4.4: Error in numerical solution of $\hat{\mathbf{u}}$ in ALE framework.

h (m)	dof#	$\ e_{\hat{\mathbf{u}}}\ _{L^2}$	$\ e_{\hat{\mathbf{u}}}\ _{H^1}$
2^{-2}	592	4.473×10^{-9}	1.344×10^{-5}
2^{-3}	2104	4.124×10^{-11}	5.669×10^{-7}
2^{-4}	7912	3.520×10^{-13}	2.341×10^{-8}
2^{-5}	30664	2.950×10^{-15}	9.629×10^{-10}
2^{-6}	120712	2.462×10^{-17}	3.958×10^{-11}

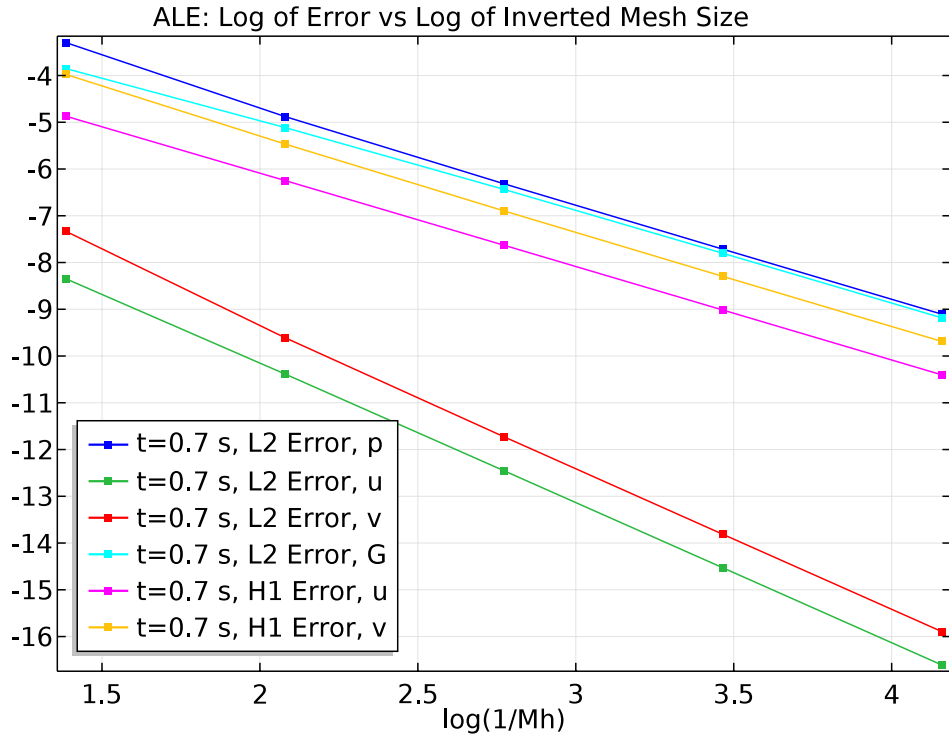


Figure 4.13: Plot of the L^2 and H^1 norms of error for p , \mathbf{v} , $\hat{\mathbf{u}}$, and \mathbf{G} — ALE.

4.4 Analysis

In each formulation of our system, we observe (in Figs. 4.1, 4.2, 4.3, 4.5, 4.6, 4.7, 4.9, 4.10, 4.11, and 4.12) that refining the mesh allows the interpolation to converge to the exact solution. For each field, the coarse mesh results illustrate that the linear or quadratic interpolation falls short at capturing the sinusoidal nature of our solutions. However, by the fifth mesh refinement, the solution for each field looks nearly exact in all three formulations.

Quantitatively, each field converges uniformly to the exact solution upon refinement of the mesh, as indicated by Figs. 4.4, 4.8, and 4.13. The solutions for \mathbf{v} , \mathbf{u} , and $\hat{\mathbf{u}}$ show the least error, essentially converging to the exact solution to within precision error by our last chosen mesh refinement. For example, in the Eulerian case, the L^2 -norm of the error in \mathbf{v} starts on the order of 10^{-8} and, by the fifth refinement, has dropped to a value on the order of 10^{-17} . These fields converge to the exact solution at a rate of 3 and their gradients converge at a rate of 2. The solutions for p and \mathbf{G} , while less accurate, still exhibit a uniform convergence upon mesh refinement at a rate of 2. On average, the solutions for p and \mathbf{G} decrease by six orders of magnitude in the L^2 -norm of the error from the first to last mesh refinements, from 10^{-4} to 10^{-10} or even 10^{-5} to 10^{-11} .

The observed convergence rates for p and \mathbf{v} (as well as \mathbf{u} in the Lagrangian case) agree with the predicted rates for the (Navier-)Stokes problem with Lagrange linear and quadratic interpolation functions, respectively (cf. [53]). Since our equations closely resemble those comprising the Navier-Stokes problem, namely the balance of mass and balance of momentum, this compliance is expected. However, our formulation is unique in that it introduces the tensor \mathbf{G} to enforce a constraint that has not been done prior to this study. As this constraint-enforcement method has only been employed by this group, there are no published works proving the uniqueness of the solution for this quantity, nor providing a guide for its convergence rates to that solution. We only comment on its convergence rate as a comparison to the rates observed in the blood-model study (see Chapter 6).

The conclusion to draw from these results is the following: *the proposed finite-element scheme solves the Oldroyd-B system smoothly, and converges to the exact solution at a uniform rate.* It is important to note that this study is not meant to compare the benefits of each formulation type: Eulerian, Lagrangian, and ALE.

If so, one would conclude that the three are interchangeable, which is false. We have simply performed a verification analysis via the Method of Manufactured Solutions to show that we have solved these problems *correctly*. Once we apply these solvers to a physical system with the proper boundary conditions, constraints, and source fields, deciding which formulation to employ may be the difference between obtaining our desired results and being unable to solve the system entirely. This phase of the research project goes beyond the scope of this study, but will be explored in the future regarding the application of choice.

Chapter 5 |

Blood Model & Study

In the previous chapters, we solved our system of equations with a constitutive relationship describing an Oldroyd-B type fluid. Three frames of reference were explored and the results of these calculations were discussed. Now, we introduce the reader to a continuum model for the behavior of blood. The model itself was proposed by K. R. Rajagopal *et. al* in 2000 [22] and applied to blood by M. Anand and K. R. Rajagopal in 2004 [30]. Following the same procedures as for the Oldroyd-B problem, we will present the governing equations in their Eulerian, Lagrangian and arbitrary Lagrangian-Eulerian (ALE) descriptions. Finally, we will provide details on the components of the study, the boundary and initial conditions, and other COMSOL Multiphysics® inputs.

5.1 Rheological Clot Model

A continuum model is not an intuitive description for blood or clotted blood. Blood is a *mixture*, made up of red blood cells (erythrocytes), white blood cells (leukocytes), and platelets floating in plasma. The red blood cells comprise about 45% by volume of healthy human blood. Clotted blood is primarily comprised of platelets within a fibrin matrix, red blood cells, and other nucleated cells (monocytes and neutrophils) with varying concentrations of each [54]. The exact behavior of blood is amazingly complex, but as a first step in capturing its full response, we will neglect the presence of these constituents. Instead, their effects on the flow of blood will be imposed on the fluid model by various material parameters. These scalar values should adjust to the concentrations of the individual molecular components, but for now, these parameters are taken to be constant. The continuum model,

though incomplete now, will serve as the backbone of our intended objective: a monolithic system incorporating the clotting and lysis mechanisms for blood, which aligns reasonably well with experimental data [31].

The authors of [30] represent blood as a viscoelastic fluid with shear-thinning properties [55, 56]. Starting with the thermodynamic framework presented in [22], the stored energy function and scalar dissipation rate are chosen by these authors to have the following form:

$$\hat{W} = \frac{\mu}{2}(I - 3), \quad (5.1)$$

$$\hat{\xi} = \alpha(\mathbf{D}_{\kappa_p(t)} : \mathbf{B}_{\kappa_p(t)} \mathbf{D}_{\kappa_p(t)})^\gamma + \eta_1 \mathbf{D} : \mathbf{D}. \quad (5.2)$$

Upon first glance, these assumptions are almost identical to those which resulted in the Oldroyd-B fluid model (Eqs. (2.5) and (2.12)); the stored energy function \hat{W} matches that chosen for both the Maxwell and Oldroyd-B model, and the dissipation rate has an identical structure. However, the difference lies in the exponent γ in the first term in $\hat{\xi}$. This adds a power-law viscous nature of the fluid, while the second term represents the Newtonian nature of plasma [30]. These assumptions, after following the maximization procedure in [22], result in the following set of constitutive equations:

$$\mathbf{T} = -p\mathbf{I} + \mathbf{S}, \quad (5.3)$$

$$\mathbf{S} = \mu \mathbf{B}_{\kappa_p(t)} + \eta \mathbf{D}, \quad (5.4)$$

$$\overset{\nabla}{\mathbf{B}}_{\kappa_p(t)} = -2 \left(\frac{\mu}{\alpha} \right)^{1+2n} [\text{tr}(\mathbf{B}_{\kappa_p(t)}) - 3\lambda]^n (\mathbf{B}_{\kappa_p(t)} - \lambda \mathbf{I}), \quad (5.5)$$

where

$$\lambda = \frac{3}{\text{tr}(\mathbf{B}_{\kappa_p(t)}^{-1})}. \quad (5.6)$$

Here, μ is the shear modulus, η is the dynamic viscosity, $n \in \mathbb{R}$ is the shear-thinning index, and $\alpha \in \mathbb{R}$ is a constant that describes the evolution of $\mathbf{B}_{\kappa_p(t)}$ [32]. Note that this model applies to *clotted* blood as well, with modification to the material parameters.

Adopting the decision made by the authors of [30], we will introduce a constant, K , to replace $\left(\frac{\mu}{\alpha}\right)^{1+2n}$. The quantity $-2K(\text{tr}(\mathbf{B}_{\kappa_p(t)}) - 3\lambda)^n$ in Eq. (5.5) replaces the term $1/\tau$ in Eq. (2.18) of the classical Oldroyd-B model. It is for this reason

that we call $[-2K(\text{tr}(\mathbf{B}_{\kappa_p(t)}) - 3\lambda)^n]^{-1}$ the relaxation time of the material. Recall that while the classical model treats the material's relaxation time as a constant, it is actually deformation-dependent. Therefore, the generalized Oldroyd-B model used here is more applicable to blood.

To alleviate the numerical difficulty in inverting the tensor \mathbf{B} in the definition of λ , we apply the Cayley-Hamilton theorem, which states that every square matrix satisfies its own characteristic equation:

$$\mathbf{B}^3 - \text{I}_B \mathbf{B}^2 + \text{II}_B \mathbf{B} - \text{III}_B \mathbf{I} = 0, \quad (5.7)$$

where I_B , II_B , and III_B are the three principal invariants of \mathbf{B} :

$$\text{I}_B = \text{tr}(\mathbf{B}), \quad \text{II}_B = \frac{1}{2}[\text{tr}(\mathbf{B})^2 - \text{tr}(\mathbf{B}^2)], \quad \text{and} \quad \text{III}_B = \det(\mathbf{B}). \quad (5.8)$$

Substituting these into Eq. (5.7), we have:

$$\mathbf{B}^3 - \text{tr}(\mathbf{B})\mathbf{B}^2 + \frac{1}{2}[\text{tr}(\mathbf{B})^2 - \text{tr}(\mathbf{B}^2)]\mathbf{B} - \det(\mathbf{B})\mathbf{I} = 0. \quad (5.9)$$

In our formulation, we define the tensor \mathbf{B} to have a determinant equal to 1, simplifying the last term. Rearranging the equation, and multiplying both sides by \mathbf{B}^{-1} , we obtain:

$$\frac{1}{2}[\text{tr}(\mathbf{B})^2 - \text{tr}(\mathbf{B}^2)]\mathbf{I} = \mathbf{B}^{-1} - \mathbf{B}^2 + \text{tr}(\mathbf{B})\mathbf{B}. \quad (5.10)$$

We then take the trace of both sides and divide each term by 3:

$$\frac{1}{2}[\text{tr}(\mathbf{B})^2 - \text{tr}(\mathbf{B}^2)] = \frac{1}{3}\text{tr}(\mathbf{B}^{-1}) + \frac{1}{3}[\text{tr}(\mathbf{B})^2 - \text{tr}(\mathbf{B}^2)], \quad (5.11)$$

which implies

$$\frac{1}{3}\text{tr}(\mathbf{B}^{-1}) = \frac{1}{6}[\text{tr}(\mathbf{B})^2 - \text{tr}(\mathbf{B}^2)]. \quad (5.12)$$

Hence, we have

$$\lambda = \frac{3}{\text{tr}(\mathbf{B}^{-1})} = \frac{6}{\text{tr}(\mathbf{B})^2 - \text{tr}(\mathbf{B}^2)}, \quad (5.13)$$

eliminating the inverse of \mathbf{B} from the formulation with its computational cost.

The problem formulations in the Eulerian, Lagrangian, and ALE frameworks are essentially identical to those for the Oldroyd-B example, derived in Chapter 2,

with the exception of the altered relaxation time. The Eulerian weak form of the blood-clot problem is

$$\int_{\Omega_x} (\nabla \cdot \mathbf{v}) \tilde{p} \, dv = 0, \quad (5.14)$$

$$\int_{\Omega_x} \rho [\partial_t \mathbf{v} + (\nabla \mathbf{v}) \mathbf{v}] \cdot \tilde{\mathbf{v}} \, dv + \int_{\Omega_x} \mathbf{T} : \nabla \tilde{\mathbf{v}} \, dv - \int_{\partial\Omega_x} \mathbf{T} \hat{\mathbf{n}} \cdot \tilde{\mathbf{v}} \, da = 0, \quad (5.15)$$

$$\begin{aligned} & \int_{\Omega_x} [\partial_t \mathbf{B}(\mathbf{G}) - (\nabla \mathbf{v}) \mathbf{B}(\mathbf{G}) - \mathbf{B}(\mathbf{G}) (\nabla \mathbf{v})^T \\ & \quad + 2K (\text{tr}(\mathbf{B}(\mathbf{G})) - 3\lambda)^n (\mathbf{B}(\mathbf{G}) - \lambda \mathbf{I})] : \tilde{\mathbf{G}} \, dv \\ & - \int_{\Omega_x} (\mathbf{B}(\mathbf{G}) \otimes \mathbf{v}) : \nabla \tilde{\mathbf{G}} \, dv + \int_{\partial\Omega_x} (\mathbf{B}(\mathbf{G}) \otimes \mathbf{v}) \hat{\mathbf{n}} : \tilde{\mathbf{G}} \, da = 0, \end{aligned} \quad (5.16)$$

with

$$\mathbf{T} = -p \mathbf{I} + \frac{1}{2} \eta (\nabla \mathbf{v} + (\nabla \mathbf{v})^T) + \mu \mathbf{B}(\mathbf{G}), \quad (5.17)$$

$$\mathbf{B}(\mathbf{G}) = J_G^{-1/3} \mathbf{G}, \quad (5.18)$$

$$\partial_t \mathbf{B}(\mathbf{G}) = J_G^{-1/3} \left[\partial_t \mathbf{G} - \frac{1}{3} \text{tr}(\mathbf{G}^{-1} \partial_t \mathbf{G}) \mathbf{G} \right]. \quad (5.19)$$

and λ given in Eq. (5.13). Recall that we have dropped the subscript $\kappa_{p(t)}$ from \mathbf{B} for simplicity, but we are in fact referring to the left Cauchy-Green stress tensor from the natural to the current configuration. The quantities ρ , μ , η , n , and K , are taken to be constant parameters of our material, with values provided in [30] and [32]. These values are tabulated in Table 5.1.

Table 5.1: Parameter values for use in clot formulation.

Parameter	Value
ρ	1025.9 kg/m ³
μ	0.01 Pa·s
η	0.1611 Pa
n	0.5859
K	58.0725 s ⁻¹

It is well studied and documented that the dynamic viscosity of blood, η , has a dependence on the shear rate [17, 18]. As we have yet to identify the optimal

expression for the viscosity as a function of shear rate, \mathbf{D} , we will approximate this parameter as a constant. This assumption is admissible in high velocity, and high shear rate, flows, but we will need to account for this dependence in the development of a complete model for blood.

In the Lagrangian framework, we have the following weak form:

$$\int_{\Omega_{\mathbf{X}}} (J - 1) \tilde{p} J \, dV = 0, \quad (5.20)$$

$$\begin{aligned} \int_{\Omega_{\mathbf{X}}} \rho \partial_{tt} \mathbf{u} \cdot \tilde{\mathbf{u}} J \, dV + \int_{\Omega_{\mathbf{X}}} \mathbf{T} \mathbf{F}^{-T} : \nabla_{\mathbf{X}} \tilde{\mathbf{u}} J \, dV \\ - \int_{\partial\Omega_{\mathbf{X}}} J \mathbf{T} \mathbf{F}^{-T} \hat{\mathbf{n}}_{\mathbf{X}} \cdot \tilde{\mathbf{u}} \, dA = 0, \end{aligned} \quad (5.21)$$

$$\begin{aligned} \int_{\Omega_{\mathbf{X}}} [\partial_t \mathbf{B}(\mathbf{G}) - (\nabla_{\mathbf{X}} \partial_t \mathbf{u}) \mathbf{F}^{-1} \mathbf{B}(\mathbf{G}) - \mathbf{B}(\mathbf{G}) \mathbf{F}^{-T} (\nabla_{\mathbf{X}} \partial_t \mathbf{u})^T \\ + 2K (\text{tr}(\mathbf{B}(\mathbf{G})) - 3\lambda)^n (\mathbf{B}(\mathbf{G}) - \lambda \mathbf{I})] : \tilde{\mathbf{G}} J \, dV = 0, \end{aligned} \quad (5.22)$$

with

$$\mathbf{T} = -p \mathbf{I} + \frac{1}{2} \eta [(\nabla_{\mathbf{X}} \partial_t \mathbf{u}) \mathbf{F}^{-1} + \mathbf{F}^{-T} (\nabla_{\mathbf{X}} \partial_t \mathbf{u})^T] + \mu \mathbf{B}(\mathbf{G}), \quad (5.23)$$

where $\mathbf{B}(\mathbf{G})$, $\partial_t \mathbf{B}(\mathbf{G})$, and λ are given by Eqs. (5.18), (5.19), and (5.13), respectively.

Lastly, in the ALE framework we have:

$$\int_{\Omega_{\mathbf{x}}} \nabla_{\mathbf{x}} \cdot (\hat{\mathbf{F}}^{-1} \mathbf{v}) \tilde{p} \hat{J} \, dV = 0, \quad (5.24)$$

$$\begin{aligned} \int_{\Omega_{\mathbf{x}}} \rho [\partial_t \mathbf{v} + (\nabla_{\mathbf{x}} \mathbf{v}) \cdot \hat{\mathbf{F}}^{-1} (\mathbf{v} - \partial_t \hat{\mathbf{u}})] \cdot \tilde{\mathbf{v}} \hat{J} \, dV \\ + \int_{\Omega_{\mathbf{x}}} \hat{J} \hat{\mathbf{T}} \hat{\mathbf{F}}^{-T} : \nabla_{\mathbf{x}} \tilde{\mathbf{v}} \, dV - \int_{\partial\Omega_{\mathbf{x}}} \hat{J} \hat{\mathbf{T}} \hat{\mathbf{F}}^{-T} \hat{\mathbf{n}}_{\mathbf{x}} \cdot \tilde{\mathbf{v}} \, dA = 0, \end{aligned} \quad (5.25)$$

$$\begin{aligned} \int_{\Omega_{\mathbf{x}}} [\partial_t \mathbf{B}(\mathbf{G}) - (\nabla_{\mathbf{x}} \mathbf{v}) \hat{\mathbf{F}}^{-1} \mathbf{B}(\mathbf{G}) - \mathbf{B}(\mathbf{G}) \hat{\mathbf{F}}^{-T} (\nabla_{\mathbf{x}} \mathbf{v})^T \\ + 2K (\text{tr}(\mathbf{B}(\mathbf{G})) - 3\lambda)^n (\mathbf{B}(\mathbf{G}) - \lambda \mathbf{I})] : \tilde{\mathbf{G}} \hat{J} \, dV \\ - \int_{\Omega_{\mathbf{x}}} [\mathbf{B}(\mathbf{G}) \otimes (\hat{\mathbf{F}}^{-1} (\mathbf{v} - \partial_t \hat{\mathbf{u}}))] : \nabla \tilde{\mathbf{G}} \hat{J} \, dV \\ + \int_{\partial\Omega_{\mathbf{x}}} [\mathbf{B}(\mathbf{G}) \otimes (\hat{\mathbf{F}}^{-1} (\mathbf{v} - \partial_t \hat{\mathbf{u}}))] \hat{\mathbf{n}} : \tilde{\mathbf{G}} \hat{J} \, dA = 0, \end{aligned} \quad (5.26)$$

$$\int_{\Omega_{\mathbf{x}}} \nabla_{\mathbf{x}} \hat{\mathbf{u}} : \nabla_{\mathbf{x}} \tilde{\mathbf{u}} \, dV + \int_{\partial\Omega_{\mathbf{x}}} \left[\frac{1}{\gamma h} (\mathbf{v} - \partial_t \hat{\mathbf{u}}) - (\nabla_{\mathbf{x}} \hat{\mathbf{u}}) \hat{\mathbf{n}} \right] \cdot \tilde{\mathbf{u}} \, dA = 0 \quad (5.27)$$

where

$$\hat{\mathbf{T}} = -p\mathbf{I} + \frac{1}{2}\eta[(\nabla_{\mathbf{x}}\mathbf{v})\hat{\mathbf{F}}^{-1} + \hat{\mathbf{F}}^{-\text{T}}(\nabla_{\mathbf{x}}\mathbf{v})^{\text{T}}] + \mu\mathbf{B}(\mathbf{G}), \quad (5.28)$$

and Eqs. (5.18), (5.19), and (5.13) hold.

5.2 Study Components

From this point on, we are not concerned with solving a physical problem. We instead will perform the same verification of our three formulations using the method of manufactured solutions (MMS) as in Chapter 3 [50]. We choose the same fields as in the Oldroyd-B problem for our unknown quantities:

$$\mathbf{MSp}(x, y, t) = p_0 \cos\left(2\pi \frac{t}{t_0}\right) \cos\left(2\pi \frac{x+y}{L}\right), \quad (5.29)$$

$$\mathbf{MSv}(x, y, t) = v_0 \sin\left(2\pi \frac{t}{t_0}\right) \left[\sin\left(2\pi \frac{x+y}{L}\right) \hat{i} + \cos\left(2\pi \frac{x-y}{L}\right) \hat{j} \right], \quad (5.30)$$

$$\mathbf{MSu}(x, y, t) = u_0 \sin\left(2\pi \frac{t}{t_0}\right) \left[\sin\left(2\pi \frac{x+y}{L}\right) \hat{i} + \cos\left(2\pi \frac{x-y}{L}\right) \hat{j} \right], \quad (5.31)$$

$$\mathbf{MS}\hat{\mathbf{u}}(x, y, t) = \hat{u}_0 \sin\left(2\pi \frac{t}{t_0}\right) \left[\sin\left(2\pi \frac{x+y}{L}\right) \hat{i} + \cos\left(2\pi \frac{x-y}{L}\right) \hat{j} \right], \quad (5.32)$$

$$\mathbf{MSv}_A(x, y, t) = \frac{2\pi\hat{u}_0}{t_0} \cos\left(2\pi \frac{t}{t_0}\right) \left[\sin\left(2\pi \frac{x+y}{L}\right) \hat{i} + \cos\left(2\pi \frac{x-y}{L}\right) \hat{j} \right] \quad (5.33)$$

and \mathbf{MSG} as in Eq. (3.12). As for the constants above, $p_0 = 1$ Pa, $v_0 = 0.01$ m/s, $u_0 = \hat{u}_0 = 0.01$ m, $G_0 = 1$, $L = 1$ m, and $t_0 = 1$ s. These functions at time $t = 0.7$ are depicted in Figs. 5.1-5.4.

It is at this point that we work backwards from these solutions to obtain the source terms, boundary conditions, and initial conditions for each field. As with the Oldroyd-B case study, we will impose pure Dirichlet boundary conditions on \mathbf{v} and \mathbf{u} and a constraint on p , which states that its global average is zero. These calculations are carried out in *Mathematica*[®], outputted to a text file, then imported directly into COMSOL Multiphysics[®].

We solve our system in two-dimensions over a square domain of side-length $L = 1$ m. The mesh is comprised of mapped quadrilateral elements of side length h . We solve the system six times, each time refining the mesh by halving h . Each field is evaluated exactly at the nodes of our mesh and the solution is interpolated

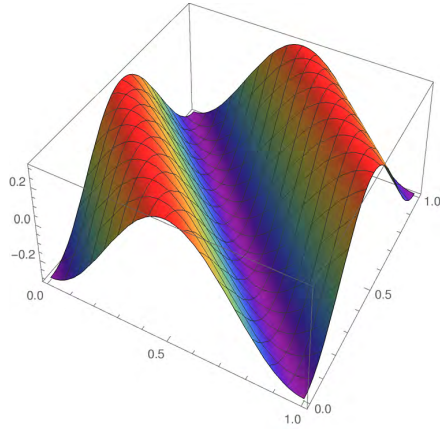


Figure 5.1: Plot of \mathbf{MS}_p at time $t = 0.7$ s.

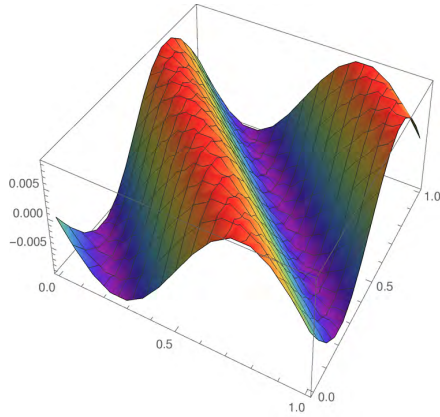


Figure 5.2: Plot of the \hat{i} -component of \mathbf{MS}_v , \mathbf{MS}_u , and $\mathbf{MS}_{\hat{u}}$ at time $t = 0.7$ s.

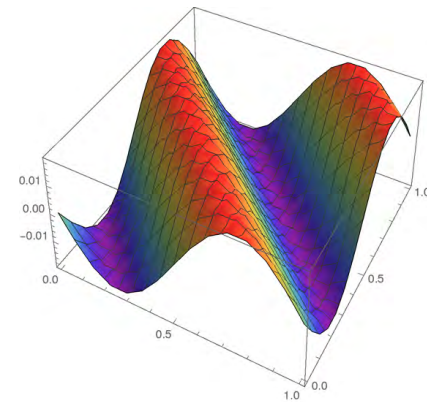


Figure 5.3: Plot of the \hat{i} -component of the \mathbf{MS}_{v_A} at time $t = 0.7$ s.

between these points by a linear combination of polynomial shape functions. We select Lagrange quadratic shape functions for the vector-valued fields: \mathbf{v} , \mathbf{u} , $\hat{\mathbf{u}}$. For

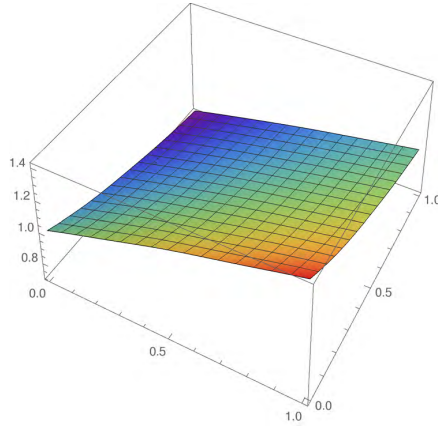


Figure 5.4: $\hat{i} \otimes \hat{i}$ component of **MSG** at time $t = 0.7$ s.

p and \mathbf{G} , we choose Lagrange linear elements. As our system is time-dependent, we use a variable-order backward differentiation formulas (BDF) to integrate over time, which is an IDA solver for differential-algebraic-equations [52]. In the next chapter, we will present the numerical solutions of this problem, and provide an analysis on the error incurred by the solver.

Chapter 6 | Blood Model Results & Analysis

As with the Oldroyd-B fluid model, a two-dimensional verification analysis was carried out of our finite element solver. For each formulation of the problem – Eulerian, Lagrangian and arbitrary Lagrangian-Eulerian (ALE) — we have performed our verification analysis with six mesh refinements, though only the second, fourth, and last refinements are shown for illustration purposes. The plots in this Chapter are of raw COMSOL Multiphysics® results, with no optical refinement on the resolution.

6.1 Eulerian Results

Recall the plots of our manufactured solution for p , \mathbf{v} , and \mathbf{G} in Figs. 5.1, 5.2, and 5.4, respectively. The corresponding COMSOL Multiphysics® outputs of these fields, with various mesh diameters can be seen in Figs. 6.1–6.3, all at time $t = 0.7$ s.

We calculate the L^2 and H^1 norms of the error, given by Eqs. 3.4-3.5, between the exact the numerical solutions at various characteristic mesh diameters, h . The magnitude of these errors are tabulated in Table 6.1. In Fig. 6.4, we have plotted the log of the inverse of the mesh length – $\log(\frac{1}{h})$ – on the x-axis, and the log of these two norms of error on the y-axis. This allows us to visualize the convergence of the error as we refine the mesh for each unknown quantity.

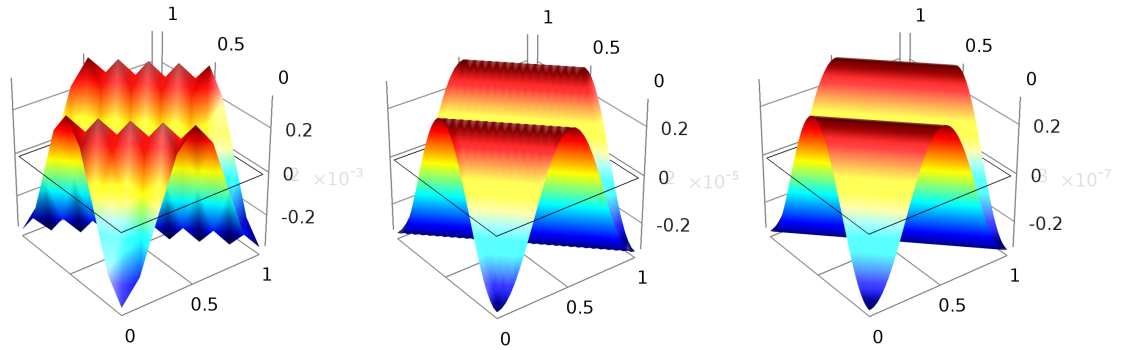


Figure 6.1: Numerical solution of p in Eulerian framework. Left to right: $h = 0.125$ m, $h = 0.0313$ m, and $h = 7.813 \times 10^{-3}$ m.

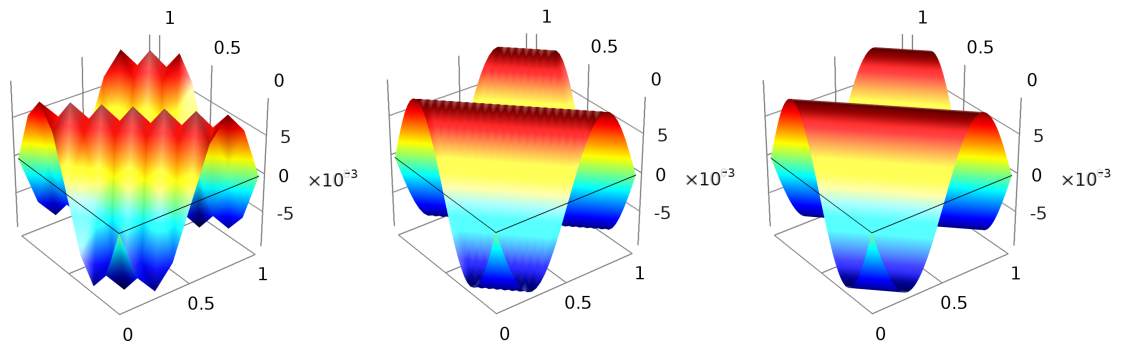


Figure 6.2: Numerical solution of v_1 in Eulerian framework. Left to right: $h = 0.125$ m, $h = 0.0313$ m, and $h = 7.813 \times 10^{-3}$ m.

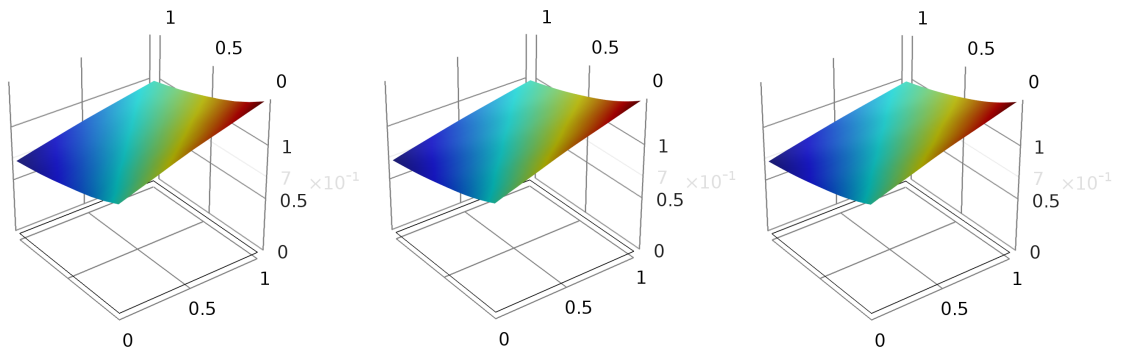


Figure 6.3: Numerical solution of \mathbf{G}_{11} in Eulerian framework. Left to right: $h = 0.125$ m, $h = 0.0313$ m, and $h = 7.813 \times 10^{-3}$ m.

Table 6.1: Error in numerical solution of p , \mathbf{v} , and \mathbf{G} in Eulerian framework.

h (m)	dof#	$\ e_p\ _{L^2}$	$\ e_v\ _{L^2}$	$\ e_v\ _{H^1}$	$\ e_{\mathbf{G}}\ _{L^2}$
2^{-2}	262	4.836×10^{-4}	4.779×10^{-9}	7.633×10^{-6}	8.213×10^{-5}
2^{-3}	902	1.339×10^{-5}	3.962×10^{-10}	4.197×10^{-6}	2.129×10^{-6}
2^{-4}	3334	4.889×10^{-7}	1.215×10^{-12}	7.332×10^{-7}	5.825×10^{-8}
2^{-5}	12806	1.936×10^{-8}	2.810×10^{-14}	8.646×10^{-9}	1.810×10^{-9}
2^{-6}	50182	7.879×10^{-10}	2.028×10^{-17}	3.011×10^{-11}	6.274×10^{-11}
2^{-7}	198662	3.226×10^{-11}	6.028×10^{-20}	1.995×10^{-13}	2.343×10^{-12}

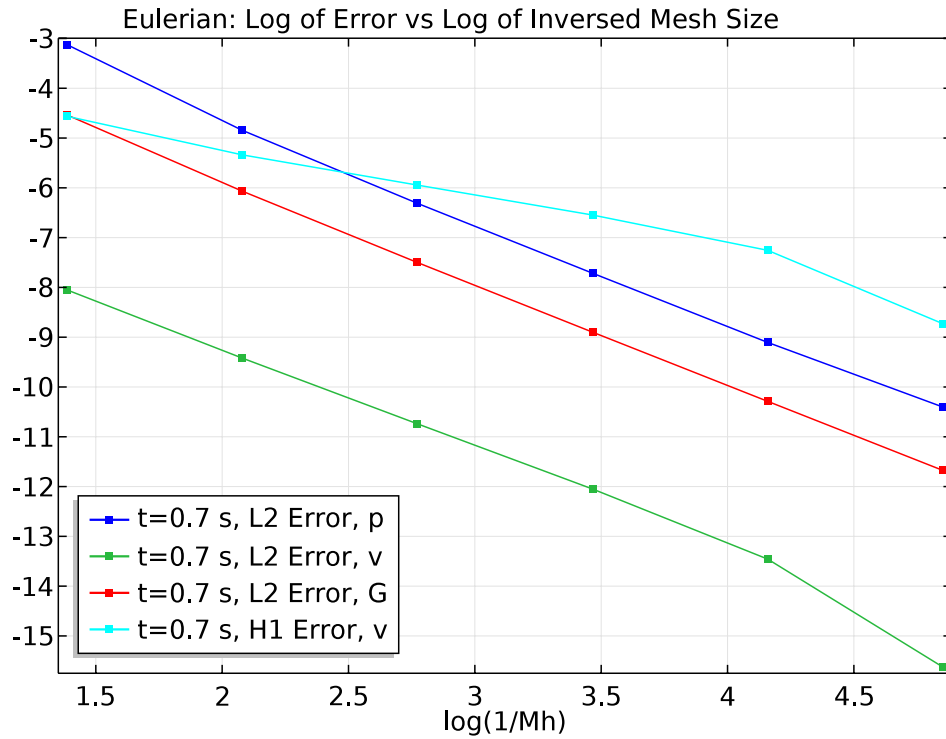


Figure 6.4: Plot of the L^2 and H^1 norms of error for p , \mathbf{v} , and \mathbf{G} — Eulerian.

6.2 Lagrangian Results

Our solutions for p , \mathbf{u} , and \mathbf{G} are given in the previous chapter and their plots can be seen in Figs. 5.1, 5.2, and 5.4, respectively. Below, we present the results outputted by COMSOL Multiphysics[®] for these three fields in Figs. 6.5–6.7.

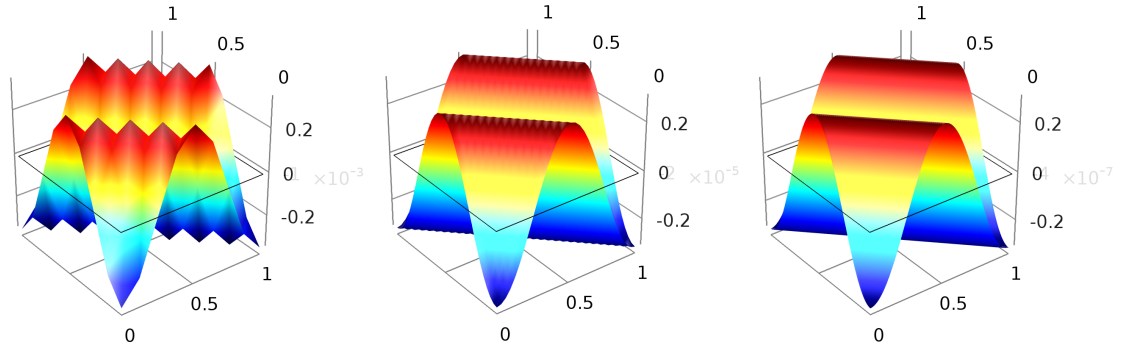


Figure 6.5: Numerical solution of p in Lagrangian framework. Left to right: $h = 0.125$ m, $h = 0.0313$ m, and $h = 7.813 \times 10^{-3}$ m.

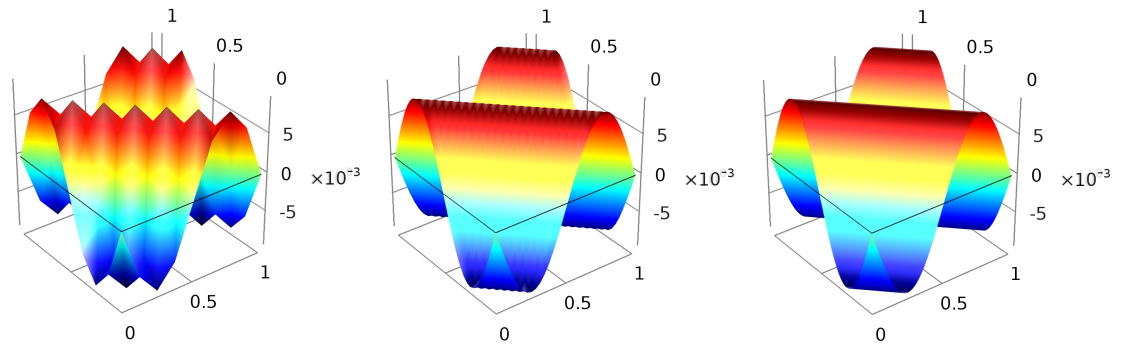


Figure 6.6: Numerical solution of \mathbf{u}_1 in Lagrangian framework. Left to right: $h = 0.125$ m, $h = 0.0313$ m, and $h = 7.813 \times 10^{-3}$ m.

We calculate the L^2 and H^1 norms of the error between the exact the numerical solutions at various characteristic mesh diameters, h . The magnitude of these errors are tabulated in Table 6.2. Plotting the log of these norms versus the log of the inverse of the mesh diameter, we obtain Fig. 6.8.

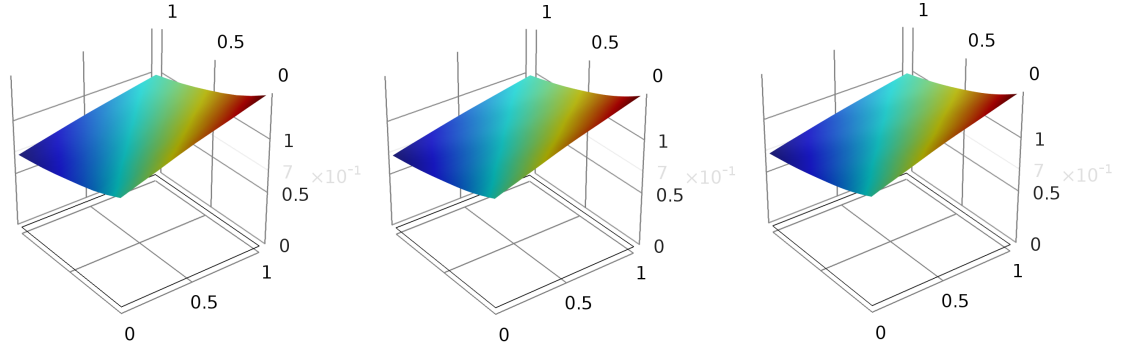


Figure 6.7: Numerical solution of \mathbf{G}_{11} in Lagrangian framework. Left to right: $h = 0.125$ m, $h = 0.0313$ m, and $h = 7.813 \times 10^{-3}$ m.

Table 6.2: Error in numerical solution of p , \mathbf{u} , and \mathbf{G} in Lagrangian framework.

h (m)	dof#	$\ e_p\ _{L^2}$	$\ e_u\ _{L^2}$	$\ e_u\ _{H^1}$	$\ e_G\ _{L^2}$
2^{-2}	262	4.749×10^{-4}	3.847×10^{-8}	5.603×10^{-5}	3.130×10^{-5}
2^{-3}	902	1.320×10^{-5}	9.211×10^{-11}	1.077×10^{-7}	8.609×10^{-7}
2^{-4}	3334	4.835×10^{-7}	4.421×10^{-13}	2.875×10^{-8}	3.165×10^{-8}
2^{-5}	12806	1.927×10^{-8}	3.136×10^{-15}	1.019×10^{-9}	1.263×10^{-9}
2^{-6}	50182	7.860×10^{-10}	3.280×10^{-17}	4.016×10^{-11}	5.150×10^{-11}
2^{-7}	198662	3.585×10^{-11}	4.275×10^{-18}	1.634×10^{-12}	2.112×10^{-12}

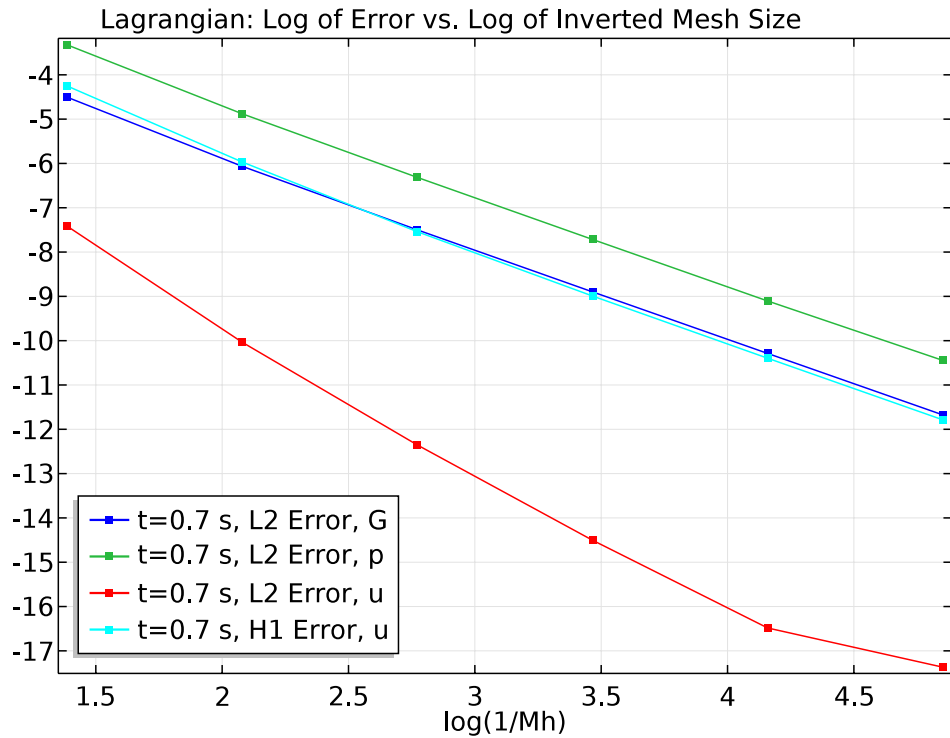


Figure 6.8: Plot of the L^2 and H^1 norms of error for p , \mathbf{u} , and \mathbf{G} – Lagrangian.

6.3 ALE Results

Plots of the exact solutions for p , \mathbf{v} , $\hat{\mathbf{u}}$, and \mathbf{G} are given in the previous chapter in Figs. 5.1, 5.3, 5.2, and 5.4. The COMSOL Multiphysics[®] outputs are shown below in Figs. 6.9–6.12 at time $t = 0.7$ s.

We calculate the L^2 and H^1 norms of the error between the exact the numerical solutions at various characteristic mesh diameters. The magnitude of these errors are tabulated in Table 6.3. Plotting the log of these norms versus the log of the inverse of the mesh diameter, we obtain Fig. 6.13.

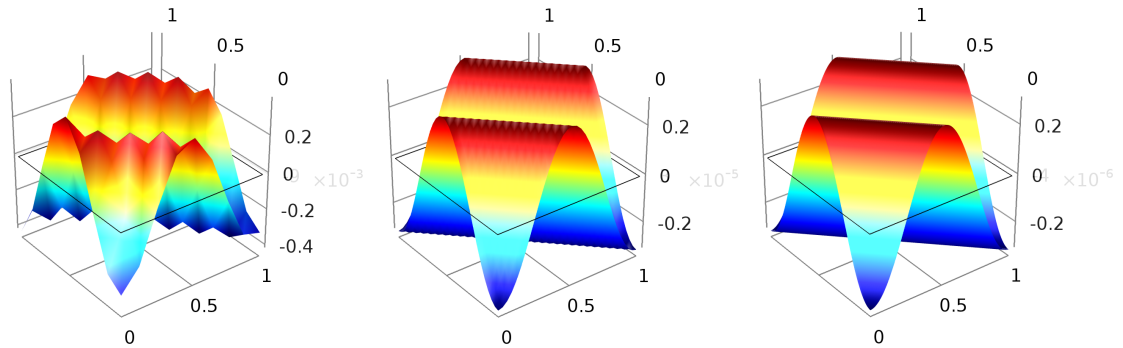


Figure 6.9: Numerical solution of p in ALE framework. Left to right: $h = 0.125$ m, $h = 0.0313$ m, and $h = 7.813 \times 10^{-3}$ m.

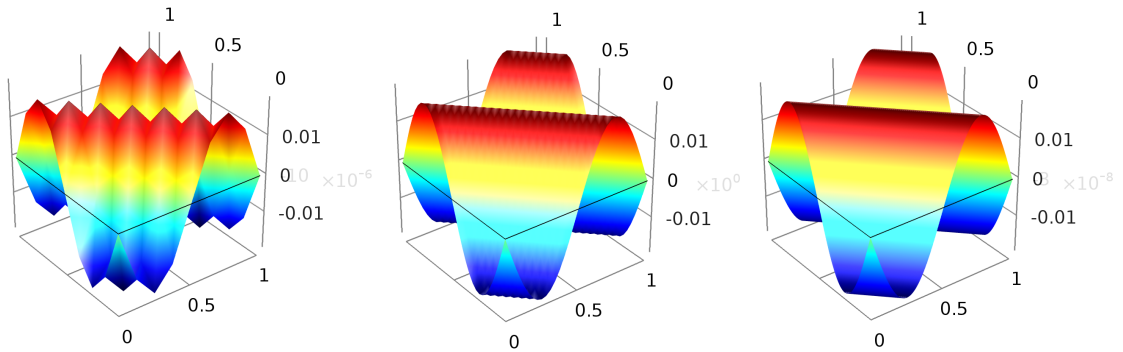


Figure 6.10: Numerical solution of v_1 in ALE framework. Left to right: $h = 0.125$ m, $h = 0.0313$ m, and $h = 7.813 \times 10^{-3}$ m.

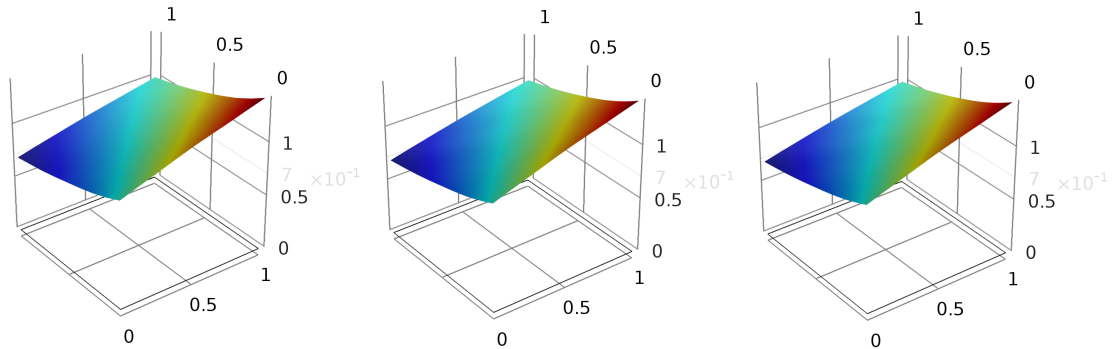


Figure 6.11: Numerical solution of \mathbf{G}_{11} in ALE framework. Left to right: $h = 0.125$ m, $h = 0.0313$ m, and $h = 7.813 \times 10^{-3}$ m.

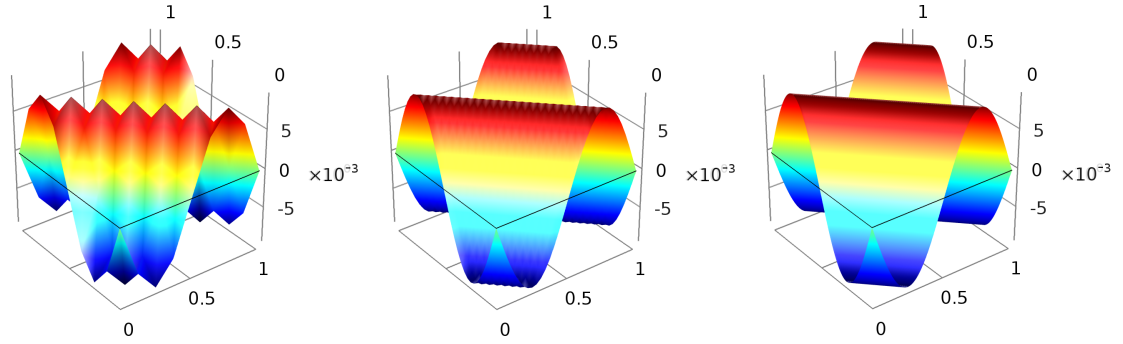


Figure 6.12: Numerical solution of $\hat{\mathbf{u}}_1$ in ALE framework. Left to right: $h = 0.125$ m, $h = 0.0313$ m, and $h = 7.813 \times 10^{-3}$ m.

Table 6.3: Error in numerical solution of p , \mathbf{v} , and \mathbf{G} in ALE framework.

h (m)	dof#	$\ e_p\ _{L^2}$	$\ e_v\ _{L^2}$	$\ e_v\ _{H^1}$	$\ e_{\mathbf{G}}\ _{L^2}$
2^{-2}	592	1.973×10^{-1}	1.444×10^{-7}	3.780×10^{-4}	3.095×10^{-5}
2^{-3}	2104	2.360×10^{-4}	8.303×10^{-10}	1.163×10^{-5}	8.638×10^{-7}
2^{-4}	7912	9.105×10^{-7}	1.994×10^{-11}	1.201×10^{-6}	3.167×10^{-8}
2^{-5}	30664	2.036×10^{-8}	9.655×10^{-13}	2.936×10^{-7}	1.263×10^{-9}
2^{-6}	120712	1.664×10^{-8}	2.496×10^{-14}	3.232×10^{-8}	5.168×10^{-11}
2^{-7}	198662	3.298×10^{-11}	6.171×10^{-16}	3.325×10^{-10}	2.124×10^{-12}

Table 6.4: Error in numerical solution of $\hat{\mathbf{u}}$ in ALE framework.

h (m)	dof#	$\ e_{\hat{\mathbf{u}}}\ _{L^2}$	$\ e_{\hat{\mathbf{u}}}\ _{H^1}$
2^{-2}	592	4.532×10^{-9}	1.345×10^{-5}
2^{-3}	2104	4.145×10^{-11}	5.670×10^{-7}
2^{-4}	7912	3.530×10^{-13}	2.341×10^{-8}
2^{-5}	30664	2.954×10^{-15}	9.629×10^{-10}
2^{-6}	120712	2.876×10^{-17}	3.958×10^{-11}
2^{-7}	198662	2.094×10^{-19}	1.626×10^{-12}

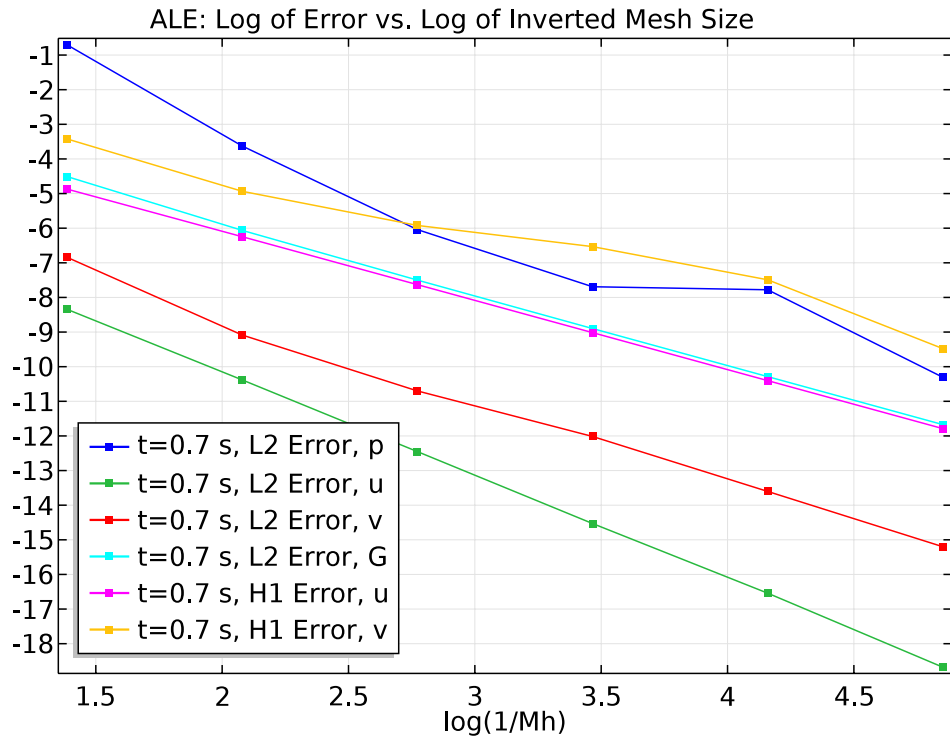


Figure 6.13: Plot of the L^2 and H^1 norms of error for p , \mathbf{v} , $\hat{\mathbf{u}}$, and \mathbf{G} — ALE.

6.4 Analysis

As with the Oldroyd-B problem solutions, we can qualitatively observe (in Figs. 6.1, 6.2, 6.3, 6.5, 6.6, 6.7, 6.9, 6.10, 6.11, and 6.12) the smoothing of the outputs with refinement of the mesh. In this chapter, we have only displayed the second, fourth, and sixth mesh refinements, simply for the purpose of visualization. The analysis of this apparent convergence begins with the quantitative data. As we know the exact solutions, we have calculated the L^2 and H^1 norms of the error between the exact and numerical solutions at each mesh diameter. The magnitude of these errors are presented in Tables 6.1–6.4. The error magnitudes in all three formulations are relatively small and decreasing, with the solutions for \mathbf{v} , \mathbf{u} , and $\hat{\mathbf{u}}$ performing the best. These fields, between the first and sixth mesh refinement, decrease in the L^2 -norm of the error by ten orders of magnitude. In the Eulerian case, the error in the solution for \mathbf{v} becomes truly negligible (on the order of 10^{-20}). As for the p and \mathbf{G} solutions, the error decreases, on average, by seven orders of magnitude over

six refinements of the mesh.

Beginning with the Eulerian convergence plot in Fig. 6.4, the L^2 -norm of the error in p and \mathbf{G} follow the expected trend of convergence at a rate of 2. The velocity solution, however, converges at a rate one lower than the expected: 2 in the L^2 -norm and 1 in the H^1 -norm. This continues steadily until the sixth mesh refinement where the error decreases with the expected rates of 3 and 2 from the fifth refinement in the L^2 and H^1 -norms of error, respectively. The Lagrangian plot (Fig. 6.8) depicts the expected convergences for all fields up until the sixth refinement. Between the fifth and sixth refinements, the L^2 -norm of the error in the displacement field \mathbf{u} does not drop as much as predicted. The actual value of the error in this quantity is on the order of 10^{-18} by the last step, which is very small relative to the other fields in this formulation. Finally we turn our attention to the ALE results. Fig. 6.13 exhibits regular convergence of $\hat{\mathbf{u}}$ and \mathbf{G} . The velocity converges at an approximate rate that is lower than expected: slope of 1 for the H^1 norm of error and a slope of 2 for the L^2 norm. The pressure does approach the true solution with refinement of the mesh, as in the error monotonically decreases with each refinement, but the rate at which it does so is unclear. More work needs to be done to ensure consistent convergence rates of these quantities in the clot problem.

Again, this study is not meant to compare the benefits of each the Eulerian, Lagrangian, and ALE formulation types. Rather, we have performed a verification analysis to show that the proposed finite-element scheme solves these problems *correctly*. From these results, it is clear that the generalized relaxation time term adds numerical instability to the system compared with the Oldroyd-B results. Refining our maximum time-step, say from 0.001 s to 0.0001 s, may mitigate these challenges, but, in conclusion, the error convergence rates need further exploration.

Chapter 7 | Conclusion

7.1 Future Plans

The results of the clot problem presented in the preceding chapter, though tending closer to the true solution with each mesh refinement, require further exploration of time-integration schemes to ensure the steady convergence of our quantities of interest. Pending the resolution of these difficulties, we may begin the process of expanding the model and testing its accuracy applied to clinical situations, such as for the clot-removal procedure outlined by Dr. Simon in [57].

7.1.1 3D Verification Analysis

In this study, we have only performed on a two-dimensional trial run of the problem. Clearly, the next step is to expand this to three-dimensions to capture the full behavior of blood flowing through a vessel. We believe that this step requires the use of an iterative, rather than a direct, solver with an appropriate preconditioner applied to our coefficient matrix.

Recall that the finite element method (FEM) reduces a fully nonlinear system of differential equations to a simple matrix statement of the form $\mathbf{Ax} = \mathbf{b}$ at each time step, where \mathbf{x} represents our vector of unknowns [49]. Therefore, the challenge in a finite element scheme lies in the numerical inversion of the matrix \mathbf{A} to solve for \mathbf{x} . For both problems presented in this document, a direct solver was sufficient to invert our coefficient matrix via a derivative of LU-decomposition. However, in three-dimensions, the size of this matrix increases drastically, and its properties play a larger role in its invertibility. For example, the underlying

coefficient matrix of our system has a block structure with a zero block on its diagonal, stemming from the incompressibility condition and the resulting coupling between the pressure quantity p and its corresponding test function \tilde{p} . This results in singular submatrices which are unable to be inverted directly. This attribute is common amongst incompressible Navier-Stokes-type systems, such as ours, where p acts as a Lagrange multiplier, enforcing the $\nabla \cdot \mathbf{v} = 0$ constraint on the velocity. Luckily, mathematicians in the field have published works on the selection of appropriate preconditioners to such problems based on the block structure of \mathbf{A} and the Schur complement of a submatrix [58–60], some of which include applications to the Stokes or Navier-Stokes systems. The objective of a preconditioner is to “reduce the number of iterations required for convergence while not increasing significantly the amount of computation required at each iteration” [61]. We will proceed by reviewing the literature on iterative methods and preconditioners for saddle point problems and adopting the established techniques.

7.1.2 Chemical Contributions to Fluid Model

The fluid model simulated in this project to describe blood, though a good first approximation to the viscoelastic tendencies of blood, has its limitations. As discussed in Chapter 5, it treats blood as a homogeneous continuum with a constant viscosity, disregarding the heterogenous nature of blood. The viscosity of blood, at low shear rates, can not be precisely approximated by a constant value, and depends on the shear rate of flow. In this study, we have used parameter values that are associated with normal 40% hematocrit, but pathology and the coagulation process vary these component concentrations and, subsequently, the properties of the fluid. In practice, it is extremely difficult to capture the fully-coupled biochemical, rheological, and mechanical effects on clot behavior. The blood model below, developed by Rajagopal et al. [30], was a big step toward this goal by capturing the clot’s mechanical response.

$$\mathbf{T} = -p\mathbf{I} + \mathbf{S}, \quad (7.1)$$

$$\mathbf{S} = \mu \mathbf{B}_{\kappa_p(t)} + \eta_1 \mathbf{D}, \quad (7.2)$$

$$\mathbf{B}_{\kappa_p(t)}^\nabla = -2 \left(\frac{\mu}{\alpha'} \right)^{1+2n} (\text{tr } \mathbf{B}_{\kappa_p(t)} - 3\lambda)^n [\mathbf{B}_{\kappa_p(t)} - \lambda \mathbf{I}], \quad (7.3)$$

$$\lambda = \frac{3}{\text{tr} \mathbf{B}^{-1}_{\kappa_p(t)}}, \quad (7.4)$$

$$n = \frac{\gamma - 1}{1 - 2\gamma}; \quad n > 0 \quad (7.5)$$

In references [30, 32, 33], M. Anand *et al.* track the concentrations of nearly 30 enzymes, proteins, and platelets present in the extrinsic pathway of coagulation to fully predict clot formation and lysis. A third governing equation, the advection-diffusion equation for mixtures, is employed to relate the component concentrations of these individual constituents with the flow of the fluid.

$$\frac{\partial[\phi]}{\partial t} + \text{Div}([\phi_i]\mathbf{v}) = \nabla \cdot (D_{\phi_i}(\mathbf{D})\nabla[\phi_i]) + G_{\phi_i}, \quad i = 1, \dots, N, \quad (7.6)$$

N being the number of constituents in the mixture. Above, $[\phi_i]$ is the concentration of constituent ϕ_i , and $D_{\phi_i}(\mathbf{D})$ is the diffusivity of the constituent as a function of the stretching tensor (the symmetric part of the velocity gradient). We have attempted trials of this step with some preliminary successes; the advection-diffusion equation was incorporated with arbitrary initial conditions on $[\phi]$. The fully-coupled system with one constituent ran successfully and converged uniformly to its intended solution, proving the accuracy of the solver. Moving forward, we will incorporate a subset of the chemical reactions in [31] into our fluid model to test our ability to couple multiple component concentrations, specifically those of thrombin, fibrin, and platelets, with the overall flow characteristics, described by the main balance laws.

7.1.3 Surrounding Artery

Thrombus formation does not occur in isolation; without the presence of the arterial wall in our simulations, we can not accurately depict the clot coagulation or lysis cycle. Blood vessels in the body are known to be elastic, adapting to pulsatile flow, and typically elliptical in shape due to the surrounding musculature [62]. Approximating the blood clot as a cylinder, assuming a rigid cylindrical tube, does not provide the most realistic results. Along with the elasticity of the boundary, the wall geometry may directly produce or influence the studied pathology, further proving the relevance of the vessel wall in our simulations.

In the coming years, we would like to synthesize models of both a functioning

artery and thrombus to depict their interactions more realistically. When incorporating multiple materials within the same framework, we may require the use of transformer (TF) elements to translate between material elements, as outlined in [63].

7.1.4 Clinical Application

Finally, for the model to be relevant in clinical research, we must test its ability to simulate real-life situations. Various scenarios would require different boundary conditions and source terms, or even slight alterations to the model.

In the case of the aforementioned mechanical thrombectomy procedure, the solution would be carried out over a cylindrical clot domain, to resemble a clot fully enveloped by a cylindrical artery – as a first approximation – with physiological boundary and initial conditions. Specifically, we would solve the model under no-slip boundary conditions with an applied traction force, mediated through the surrounding blood, on one face of the cylinder to represent the alternating suction pressure as an approximation of the proposed procedure. The true stress would then be studied at the clot boundary, with expectations of sharp peaks in the stress on that surface, implying clot detachment at the arterial wall.

The study of a few medical scenarios would require slight modifications to our system. For example, massive hemorrhaging occurs when a blood vessel ruptures in the body and the victim rapidly loses large amounts of blood from their circulating blood volume. This event can result in coagulopathy, or the impairment of the body’s natural clotting mechanisms, which prevents the victims ability to halt the outward flow. In studying this clotting phenomenon, the overall blood flow velocity is much higher than in that of a stroke and the problem becomes *advection-dominated*. These problems require stabilization techniques to mitigate the challenges that arise in modeling both fine and coarse spatial scales. As it preserves the consistency of the physical problem, the method called the streamline upwind/Petrov-Galerkin formulations [64] would perhaps offer the best framework for the stabilization of our problem.

7.2 Conclusion

The objective of this work is the development of a fully-coupled clot coagulation/lysis model, incorporating the biochemical, mechanical, and rheological characteristics of blood. This thesis documents the first step of this venture, focusing on the mechanical blood model and disregarding the presence of individual constituents. We have developed a simulation scheme in COMSOL Multiphysics[®] to model the behavior of various viscoelastic fluids. We tested its ability with the classical Oldroyd-B fluid, and then with a generalized model that has been accepted to represent human blood [30, 32, 33]. The constitutive relationships models were developed by Rajagopal *et al.* using a thermodynamical framework [22], governed by specific energy dissipation and storage functions. The governing system of equations, comprised of the balance of mass, momentum, and a strain-evolution law, is converted from its Eulerian form to its Lagrangian and arbitrary Lagrangian-Eulerian (ALE) descriptions. With our choices regarding the finite element and time-integration schemes, we implemented the method of manufactured solutions (MMS) for a planar problem on each formulation to assess the accuracy of the solver. Overall, the solver delivers the manufactured pressure, velocity and strain solutions with scant error and uniform convergence when solving the system for an Oldroyd-B fluid. Incorporating the fluid model for blood, the numerical solutions approach the exact solution with refinement of the mesh for all three formulations, but not always at the expected rates. The solver requires further study and development of a proper time-integration scheme for the clot problem before moving forward with the work discussed above.

Appendix |

Proof of Equivalence Between Two Models

1 Rajagopal et al.

As discussed in Chapter 2, the classical Oldroyd-B fluid model derived in the paper written by Rajagopal et al. in 2000 is written in the following form:

$$\mathbf{T} = -p\mathbf{I} + \mathbf{S}, \quad (.1)$$

$$\mathbf{S} = \mu\mathbf{B}_{\kappa_p(t)} + \eta_1\mathbf{D}, \quad (.2)$$

$$\mathbf{S} + \frac{\eta}{2\mu}\overset{\nabla}{\mathbf{S}} = \eta_1\left(\mathbf{D} + \frac{\eta}{2\mu}\overset{\nabla}{\mathbf{D}}\right) + \mu\lambda\mathbf{I}. \quad (.3)$$

Substituting \mathbf{S} into .1 and .3, we have,

$$\mathbf{T} = -p\mathbf{I} + \eta_1\mathbf{D} + \mu\mathbf{B}_{\kappa_p(t)}, \quad (.4)$$

$$(\eta_1\mathbf{D} + \mu\mathbf{B}_{\kappa_p(t)}) + \frac{\eta}{2\mu}\overset{\nabla}{(\eta_1\mathbf{D} + \mu\mathbf{B}_{\kappa_p(t)})} = \eta_1\left(\mathbf{D} + \frac{\eta}{2\mu}\overset{\nabla}{\mathbf{D}}\right) + \mu\lambda\mathbf{I}. \quad (.5)$$

Distributing the upper-convected derivative on the left-hand-side of .5 gives,

$$(\eta_1\mathbf{D} + \mu\mathbf{B}_{\kappa_p(t)}) + \frac{\eta}{2\mu}(\eta_1\overset{\nabla}{\mathbf{D}} + \mu\overset{\nabla}{\mathbf{B}_{\kappa_p(t)}}) = \eta_1\left(\mathbf{D} + \frac{\eta}{2\mu}\overset{\nabla}{\mathbf{D}}\right) + \mu\lambda\mathbf{I}. \quad (.6)$$

Observe that the term involving \mathbf{D} shows up on both sides of the equation. Canceling these, we find,

$$\mu \mathbf{B}_{\kappa_p(t)} + \frac{\eta}{2} \overset{\nabla}{\mathbf{B}}_{\kappa_p(t)} = \mu \lambda \mathbf{I}. \quad (.7)$$

We can now expand the upper-convected derivate of \mathbf{B} according to the definition, $\overset{\nabla}{\mathbf{A}} = \dot{\mathbf{A}} - \mathbf{L}\mathbf{A} - \mathbf{A}\mathbf{L}^T$, for any arbitrary tensor \mathbf{A} . From this point on, we will drop the $\kappa_p(t)$ subscript on the stress tensor \mathbf{B} for efficiency, but it is important to note that this strain tensor is defined in the natural configuration of the body.

$$\mu \mathbf{B} + \frac{\eta}{2} (\dot{\mathbf{B}} - \mathbf{L}\mathbf{B} - \mathbf{B}\mathbf{L}^T) = \mu \lambda \mathbf{I}. \quad (.8)$$

Expanding the material derivative and substituting in $\nabla \mathbf{v}$ for \mathbf{L} ,

$$\frac{\partial \mathbf{B}}{\partial t} + (\nabla \mathbf{B})\mathbf{v} - (\nabla \mathbf{v})\mathbf{B} - \mathbf{B}(\nabla \mathbf{v})^T = \frac{2\mu}{\eta} (\lambda \mathbf{I} - \mathbf{B}). \quad (.9)$$

Equations .4 and .9 showcase a simplified version of the model outlined in [22].

2 Hron et al.

The Oldroyd-B fluid model used in [29] is written in the following form:

$$\mathbf{T} = -p\mathbf{I} + 2\eta_s \mathbf{D} + \mu(\mathbf{B} - \mathbf{I}), \quad (.10)$$

$$\frac{\partial \mathbf{B}}{\partial t} + (\nabla \mathbf{B})\mathbf{v} - (\nabla \mathbf{v})\mathbf{B} - \mathbf{B}(\nabla \mathbf{v})^T = \frac{1}{\tau}(\mathbf{I} - \mathbf{B}), \quad (.11)$$

with η_s being the viscosity of the solvent in the experiment, μ being the material constant for the elastic modulus, and τ the relaxation time of the material. When we expand and regroup the terms in .10, we find,

$$\mathbf{T} = -(p + \mu)\mathbf{I} + 2\eta_s \mathbf{D} + \mu \mathbf{B}. \quad (.12)$$

Upon inspection, we can see that this Cauchy stress equation is equivalent to the simplified version of the equation at the end of the previous section (.4). The only differences lie within the values of the constants, but these coefficients themselves represent the same material quantities as in [22]. As for the evolution of the natural configuration of the fluid, the left-hand-sides of both .9 and .11 are

equivalent, but the right-hand-sides have differing coefficients. Using dimension analysis, we can show that these constants represent the same material parameter, henceforth proving that both models are identical. According to the latter equation, the coefficient in front of $(\mathbf{I} - \mathbf{B})$ should have dimensions of $[t^{-1}]$. We know that λ is dimensionless based on its definition ($\lambda = \frac{3}{\text{tr } \mathbf{B}^{\kappa_p(t) - 1}}$), μ has units of $[Pa]$, and η has units of $[Pa \cdot s]$, giving the coefficient the same units as in equation .11, and proving the models equivalence.

Bibliography

- [1] SMITH, W. S. (2006) “Safety of Mechanical Thrombectomy and Intravenous Tissue Plasminogen Activator in Acute Ischemic Stroke. Results of the multi Mechanical Embolus Removal in Cerebral Ischemia (Merci) Trial, Part I,” *American Journal of Neuroradiology*, **27**(6), pp. 1177–1182, DOI: 10.1016/S0513-5117(08)79192-0; PMID: 16775259.
- [2] DONNAN, G. A., M. FISHER, and M. MACLEOD (2008) “Stroke,” *Lancet*, **371**(9624), pp. 1612–1623, DOI: 10.1016/S0140-6736(08)60694-7; PMID: 18468545.
- [3] RITZ, K., N. P. DENSWIL, O. C. STAM, J. J. VAN LIESHOUT, and M. J. DAEMEN (2014) “Cause and Mechanisms of Intracranial Atherosclerosis,” *Circulation*, **130**(16), pp. 1407–1414, DOI: 10.1161/CIRCULATION-AHA.114.011147; PMID: 25311618.
- [4] (2014), “Post-Stroke Rehabilitation,” <http://stroke.nih.gov/materials/rehabilitation.htm>.
- [5] MAYO CLINIC STAFF, “Stroke,” <http://www.mayoclinic.org/diseases-conditions/stroke/diagnosis-treatment/treatment/txc-20117296>.
- [6] BATH, P. M. and J. M. WARDLAW (2015) “Pharmacological Treatment and Prevention of Cerebral Small Vessel Disease: A Review of Potential Interventions,” *International Journal of Stroke*, **10**(4), pp. 469–478, DOI: 10.1111/ijss.12466; PMID: 25727737.
- [7] ASADI, H., D. WILLIAMS, and J. THORNTON (2016) “Changing Management of Acute Ischaemic Stroke: The New Treatments and Emerging Role of Endovascular Therapy,” *Current Treatment Options in Neurology*, **18**(5), pp. 1–19, DOI: 10.1007/s11940-016-0403-8; PMID: 27017832.
- [8] BERLIS, A., H. LUTSEP, S. BARNWELL, A. NORBASH, L. WECHSLER, C. A. JUNGREIS, A. WOOLFENDEN, G. REDEKOP, M. HARTMANN, and M. SCHUMACHER (2004) “Mechanical Thrombolysis in Acute Ischemic Stroke

- with Endovascular Photoacoustic Recanalization,” *Stroke*, **35**(5), pp. 1112–1116, DOI: 10.1161/01.STR.0000124126.17508.d3; PMID: 15017011.
- [9] KATZ, J. M. and Y. P. GOBIN (2006) “Merci® Retriever in Acute Stroke Treatment,” *Expert Review of Medical Devices*, **3**(3), pp. 273–280, DOI:10.1586/17434440.3.3.273; PMID: 16681448.
- [10] BROUSSALIS, E., E. TRINKA, W. HITZL, A. WALLNER, V. CHROUST, and M. KILLER-OBERPFALZER (2013) “Comparison of Stent-retriever Devices versus the Merci Retriever for Endovascular Treatment of Acute Stroke,” *AJNR American Journal of Neuroradiology*, **34**(2), pp. 366–372, doi: 10.3174/a-jnr.A3195; PMID: 22790249.
- [11] SIMON, S., C. P. GREY, T. MASSENZO, D. G. SIMPSON, and P. W. LONGEST (2013) “Exploring the Efficacy of Cyclic vs Static Aspiration in a Cerebral Thrombectomy Model: An Initial Proof of Concept Study,” *Journal of NeuroInterventional Surgery*, **0**, pp. 1–7, DOI: 10.1136/neurintsurg-2013-010941; PMID: 24235098.
- [12] SALARI, K. and P. KNUPP (2000) *Code Verification by The Method of Manufactured Solutions, Sand2000-1444*, Sandia National Laboratories.
- [13] FUNG, F. C. (1993) *Biomechanics: Mechanical Properties of Living Tissues*, 2nd ed., Springer.
- [14] MADER, S. S. and M. WINDELSPECHT (2012) *Biology*, 11th ed., McGraw-Hill Education.
- [15] COWMAN, A. F., J. HEALER, D. MARAPANA, and K. MARSH (2016) “Malaria: Biology and Disease,” *Cell*, **167**(3), pp. 610 – 624.
URL <http://www.sciencedirect.com/science/article/pii/S009286741631008X>
- [16] YAZDANI, A., H. LI, J. D. HUMPHREY, and G. E. KARNIADAKIS (2017) “A General Shear-Dependent Model for Thrombus Formation,” *PLOS Computational Biology*, **13**(1), pp. 1–24.
URL <https://doi.org/10.1371/journal.pcbi.1005291>
- [17] SEQUEIRA, A. and J. JANELA (2007) “An Overview of Some Mathematical Models of Blood Rheology,” in *A Portrait of State-of-the-Art Research at the Technical University of Lisbon* (M. S. Pereira, ed.), Springer, pp. 65–87.
- [18] THURSTON, G. B. (1996) “Viscoelastic Properties of Blood and Blood Analogs,” in *Advances in Hemodynamics and Hemorheology* (T. V. How, ed.), vol. 1, Jai Press Inc., pp. 1–30.

- [19] TAYLOR, C. A., T. J. R. HUGHES, and C. K. ZARINS (1998) “Finite Element Modeling of Blood Flow in Arteries,” *Computer Methods in Applied Mechanics and Engineering*, **158**(1–2), pp. 155–196, DOI: 10.1016/S0045-7825(98)80008-X.
- [20] OSHIMA, M., R. TORII, T. KOBAYASHI, N. TANIGUCHI, and K. TAKAGI (2001) “Finite Element Simulation of Blood Flow in the Cerebral Artery,” *Computer Methods in Applied Mechanics and Engineering*, **191**(6–7), pp. 661–671, DOI: 10.1016/S0045-7825(01)00307-3.
- [21] OLDROYD, J. G. (1950) “On the Formulation of Rheological Equations of State,” *Proceedings of the Royal Society A: Mathematical and Physical Sciences*, **200**(1063), pp. 523–541, DOI: 10.1098/rspa.1950.0035.
- [22] RAJAGOPAL, K. R. and A. R. SRINIVASA (2000) “A Thermodynamic Frame Work for Rate Type Fluid Models,” *Journal of Non-Newtonian Fluid Mechanics*, **88**(3), pp. 207–227, DOI: 10.1016/S0377-0257(99)00023-3.
- [23] ——— (2004) “On the Thermomechanics of Materials that have Multiple Natural Configurations Part I: Viscoelasticity and Classical Plasticity,” *Zeitschrift für Angewandte Mathematik und Physik*, **55**(5), pp. 861–893, DOI: 10.1007/s00033-004-4019-6.
- [24] ——— (2004) “On the Thermomechanics of Materials that have Multiple Natural Configurations Part II: Twinning and Solid to Solid Phase Transition,” *Zeitschrift für Angewandte Mathematik und Physik*, **55**(5), pp. 1074–1093, DOI: 10.1007/s00033-004-4020-0.
- [25] ZAMAN, G., S. ISLAM, Y. H. KANG, and I. H. JUNG (2012) “Blood flow of an Oldroyd-B fluid in a blood vessel incorporating a Brownian stress,” *Science China Physics, Mechanics and Astronomy*, **55**(1), pp. 125–131.
URL <https://doi.org/10.1007/s11433-011-4571-y>
- [26] ZAMAN, A., N. ALI, B. ANWAR, and M. SAJID (2016) “Unsteady Two-Layered Blood Flow Through A W-Shaped Stenosed Artery Using The Generalized Oldroyd-B Fluid Model,” *The ANZIAM Journal*, **58**(1), pp. 96–118.
- [27] HAMZAH, B., A. LAHCEN, and D. BALEANU (2017) “Pulsatile blood flow in constricted tapered artery using a variable-order fractional Oldroyd-B model,” *Thermal Science*, **21**(1 Part A), pp. 29–40.
- [28] ANAND, M., J. KWACK, and A. MASUD (2013) “A new generalized Oldroyd-B model for blood flow in complex geometries,” *International Journal of Engineering Science*, **72**, pp. 78–88.

- [29] HRON, J., K. R. RAJAGOPAL, and K. TŮMA (2014) “Flow of a Burgers Fluid due to Time Varying Loads on Deforming Boundaries,” *Journal of Non-Newtonian Fluid Mechanics*, **210**, pp. 66–77, DOI: 10.1016/j.jnnfm.2014.05.005.
- [30] ANAND, M. and K. R. RAJAGOPAL (2004) “A Shear-Thinning Viscoelastic Fluid Model for Describing the Flow of Blood,” *International Journal of Cardiovascular Medicine and Science*, **4**(2), pp. 59–68.
- [31] ANAND, M., K. RAJAGOPAL, and K. R. RAJAGOPAL (2003) “A Model Incorporating some of the Mechanical and Biochemical Factors Underlying Clot Formation and Dissolution in Flowing Blood,” *Journal of Theoretical Medicine*, **5**(3–4), pp. 183–218, DOI: 10.1080/10273660412331317415.
- [32] ——— (2006) “A Model for the Formation and Lysis of Blood Clots,” *Pathophysiology of Haemostasis and Thrombosis*, **34**(2–3), pp. 109–120, DOI: 10.1159/000089931; PMID: 16432312.
- [33] ——— (2006) “A viscoelastic fluid model for describing the mechanics of a coarse ligated plasma clot,” *Theoretical and Computational Fluid Dynamics*, **20**(4), pp. 239–250.
URL <http://link.springer.com/10.1007/s00162-006-0019-9>
- [34] MÁLEK, J. and K. R. RAJAGOPAL (2007) “Incompressible rate type fluids with pressure and shear-rate dependent material moduli,” *Nonlinear Analysis: Real World Applications*, **8**, pp. 156–164.
- [35] SEQUEIRA, A. and T. BODNÁR (2014) “Blood Coagulation Simulations using a Viscoelastic Model,” *Mathematical Modelling of Natural Phenomena*, **9**(6), pp. 34–45.
- [36] GOOD, B. C., S. DEUTSCH, and K. B. MANNING (2016) “Hemodynamics in a Pediatric Ascending Aorta Using a Viscoelastic Pediatric Blood Model,” *Annals of Biomedical Engineering*, **44**(4), pp. 1019–1035.
URL <https://doi.org/10.1007/s10439-015-1370-z>
- [37] ——— (2016) “Continuous and Pulsatile Pediatric Ventricular Assist Device Hemodynamics with a Viscoelastic Blood Model,” *Cardiovascular Engineering and Technology*, **7**(1), pp. 23–43.
URL <https://doi.org/10.1007/s13239-015-0252-8>
- [38] GURTIN, M. E. (1981) *An Introduction to Continuum Mechanics*, vol. 158 of *Mathematics in Science and Engineering*, Academic Press, San Diego.
- [39] MOROZOV, A. and S. E. SPAGNOLIE (2015) “Introduction to Complex Fluids,” in *Complex Fluids in Biological Systems* (S. E. Spagnolie, ed.), Biological and

Medical Physics, Biomedical Engineering, chap. 1, Springer, New York, NY, USA, pp. 3–52.

- [40] SARAMITO, P. (2016) *Complex Fluids*, vol. 79 of *Mathématique et Applications*, Springer, Cham, Switzerland.
- [41] TAZRAEI, P., A. RIASI, and B. TAKABI (2015) “The Influence of the Non-Newtonian Properties of Blood on Blood-Hammer Through the Posterior Cerebral Artery,” *Mathematical Biosciences*, pp. 119–127.
- [42] TRUESDELL, C. A. and W. NOLL (2004) *The Non-Linear Field Theories of Mechanics*, third ed., Springer, Berlin, the first edition appeared in 1965.
- [43] GURTIN, M. E., E. FRIED, and L. ANAND (2010) *The Mechanics and Thermodynamics of Continua*, Cambridge University Press, New York.
- [44] MAUGIN, G. A. (1992) *The Thermomechanics of Plasticity and Fracture*, Cambridge Texts in Applied Mathematics, Cambridge University Press, Cambridge.
- [45] FERNÁNDEZ, M. A., L. FORMAGGIA, J.-F. GERBEAU, and A. QUARTERONI (2009) “The Derivation of the Equations for Fluids and Structure,” in *Cardiovascular Mathematics: Modeling and Simulation of the Circulatory System* (L. Formaggia, A. Quarteroni, and A. Veneziani, eds.), vol. 1 of *Modeling, Simulation and Applications (MS&A)*, chap. 3, Springer, pp. 77–121, DOI: 10.1007/978-88-470-1152-6_3.
- [46] SCOVAZZI, G. and T. J. R. HUGHES (2007) “Lecture Notes on Continuum Mechanics on Arbitrary Moving Domains,” *Sandia National Laboratories*.
- [47] ODEN, J. T. (2008) “A Short-Course on Nonlinear Continuum Mechanics,” .
- [48] JUNTUNEN, M. and R. STENBERG (2009) “Nitsche’s Method for General Boundary Conditions,” *Mathematics of Computation*, **78**(267), pp. 1353–1374.
- [49] HUGHES, T. J. R. (2000) *Fundamental Concepts; a Simple One-Dimension Boundary-Value Problem*, chap. 1, Dover Publications Inc., Minneola, NY, pp. 1–56.
- [50] SALARI, K. and P. KNUPP (2000) *Code Verification by the Method of Manufactured Solutions*, *Tech. rep.*, Sandia National Laboratories, Albuquerque, NM.
- [51] BRENNER, S. C. and L. RIDGWAY SCOTT (2002) *The Mathematical Theory of Finite Element Methods*, vol. 15 of *Texts in Applied Mathematics*, 2nd ed., Springer-Verlag.

- [52] HINDMARSH, A. C., P. N. BROWN, K. E. GRANT, S. L. LEE, R. SERBAN, D. E. SHUMAKER, and C. S. WOODWARD (2005) “SUNDIALS: Suite of Nonlinear and Differential/Algebraic Equation Solvers,” *ACM Transactions on Mathematical Software*, **31**(3), pp. 363–396.
URL <http://doi.acm.org/10.1145/1089014.1089020>
http://dl.acm.org/ft_gateway.cfm?id=1089020&type=pdf
- [53] BREZZI, F. and M. FORTIN (1991) *Mixed and Hybrid Finite Element Methods*, vol. 15 of *Springer Series in Computational Mathematics*, Springer-Verlag, New York.
- [54] SINGH, P., R. KAUR, and A. KAUR (2013) “Clot composition and treatment approach to acute ischemic stroke: The road so far,” *Annals of Indian Academy of Neurology*, **16**(4), pp. 494–497.
- [55] CHIEN, S., S. USAMI, R. J. DELLENBACK, M. I. GREGERSEN, L. B. NANINGA, and M. M. GUEST (1967) “Blood Viscosity: Influence of Erythrocyte Aggregation,” *Science*, **157**(3790), pp. 829–831, <http://science.sciencemag.org/content/157/3790/829.full.pdf>.
URL <http://science.sciencemag.org/content/157/3790/829>
- [56] CHIEN, S., S. USAMI, R. J. DELLENBACK, and M. I. GREGERSEN (1967) “Blood Viscosity: Influence of Erythrocyte Deformation,” *Science*, **157**(3790), pp. 827–829, <http://science.sciencemag.org/content/157/3790/827.full.pdf>.
URL <http://science.sciencemag.org/content/157/3790/827>
- [57] COSTANZO, F., S. ZHANG, and S. D. SCOTT (2014) “Computational Modeling of Clot Fracture Mechanics for the Surgical Therapy of Acute Stroke,” Grant funded by the *Penn State Clinical and Translational Institute*.
- [58] CAO, Y., J. DU, and Q. NIU (2014) “Shift-splitting preconditioners for saddle point problems,” *Journal of Computational and Applied Mathematics*, **272**, pp. 239 – 250.
- [59] NOTAY, Y. (2014) “A New Analysis of Block Preconditioners for Saddle Point Problems,” *SIAM Journal on Matrix Analysis and Applications*, **35**(1), pp. 143–173.
- [60] ELMAN, H. C., D. J. SILVESTER, and A. J. WATHEN (2002) “Performance and analysis of saddle point preconditioners for the discrete steady-state Navier-Stokes equations,” *Numerische Mathematik*, **90**(4), pp. 665–688.
URL <https://doi.org/10.1007/s002110100300>

- [61] MURPHY, M. F., G. H. GOLUB, and A. J. WATHEN (2000) “A Note on Preconditioning for Indefinite Linear Systems,” *SIAM Journal on Scientific Computing*, **21**(6), pp. 1969–4, copyright - Copyright] © 2000 Society for Industrial and Applied Mathematics; Last updated - 2012-02-14.
 URL <http://ezaccess.libraries.psu.edu/login?url=https://search-proquest-com.ezaccess.libraries.psu.edu/docview/921354189?accountid=13158>
- [62] HOLZAPFEL, G. A. and R. W. OGDEN (2010) “Constitutive Modelling of Arteries,” *Proceedings of the Royal Society A: Mathematical, Physical and Engineering Sciences*, **466**(2118), pp. 1551–1597, DOI: 10.1098/rspa.2010.0058.
- [63] ROMERO, G., M. L. MARTINEZ, G. PEARCE, and J. M. MERA (2012) “An Investigation into the Performance of a New Mechanical Thrombectomy Device using Bond Graph Modeling: Application to the Extraction of Blood Clots in the Middle Cerebral Artery,” *Simulation*, **89**(3), pp. 381–391, DOI: 10.1177/0037549712463418.
- [64] BROOKS, A. N. and T. J. HUGHES (1982) “Streamline upwind/Petrov-Galerkin formulations for convection dominated flows with particular emphasis on the incompressible Navier-Stokes equations,” *Computer Methods in Applied Mechanics and Engineering*, **32**, pp. 199–259.